Title
Exploiting atom-cavity coupling to measure real-time changes in the atomic spatial distribution

Author
Schlupf, Chandler

Publication Date
2020

Peer reviewed|Thesis/dissertation

UNIVERSITY OF CALIFORNIA

Los Angeles

Exploiting atom-cavity coupling to measure real-time changes in the atomic spatial distribution

A dissertation submitted in partial satisfaction
of the requirements for the degree
Doctor of Philosophy in Physics

by

Chandler Rae Schlupf

2020

ABSTRACT OF THE DISSERTATION

Exploiting atom-cavity coupling to measure real-time changes in the atomic spatial distribution

by

Chandler Rae Schlupf
Doctor of Philosophy in Physics
University of California, Los Angeles, 2020
Professor Paul Hamilton, Chair

This dissertation details the construction of a neutral ultracold atom system along with one completed experiment and one future experiment. This systems contains a two-stage slowing/cooling scheme with a Zeeman slower and a magneto-optical trap (MOT), as well as an in-vacuum optical cavity. The optical cavity was specially designed for precision measurement experiments. When near resonance atoms are present in the cavity, they cause a phase shift in the light. This enables use of the cavity light transmission as a minimally invasive feedback for information on the presence of atoms in the cavity. We look at this atom cavity interaction in two regimes: a deep lattice and a shallow lattice.

Atoms confined to a deep optical lattice are constrained to thousands of individual wells. Any feedback on the lattice from motion of atoms in a single well is amplified by thousands due to this repetition. We exploit this deep lattice uniformity to measure atomic motion immediately after release from the deep lattice using another very shallow probe lattice. The feedback from the atomic motion on the probe lattice cavity transmission is used to measure the atomic samples original temperature without losing the atoms. We measure the sample's temperature in both the axial and radial direction, with the axial measurement taking < 10 μs with the ability to recapture 75% of the atoms back into the lattice.

Atoms in a shallow lattice have wavefunctions spread out across multiple lattice cites. This enables them to undergo a process called Bloch oscillations, which requires a periodic potential plus a uniform force (gravity). I perform a simulation of the coupled atom and lattice distributions to optimize our experimental realization of the system. The atomic oscillations due to gravity imprint their oscillation frequency on the transmission of cavity light, which enables us to measure the force on the atoms which is directly proportional to the frequency. We plan on using this feature to perform a precision measurement on our atoms to look for ultralight dark matter. I estimate our limits on this type of dark matter, and discuss the future of this experiment.

The dissertation of Chandler Rae Schlupf is approved.

Wesley Campbell

Eric Hudson

Robert D. Cousins

Paul Hamilton, Committee Chair

University of California, Los Angeles

2020

Table of Contents

List of Figures

List of Variables

Γ = Natural atomic linewidth

I_s = Saturation intensity

I = Intensity felt by the atoms

δ = Atomic detuning, $\omega_a - \omega$

R_{scatt} = Scattering rate

$\hbar$ = Reduced Planck's constant

k = Wavenumber

F_{scatt} = Scattering force

ω = Angular frequency (note that all frequencies used in this thesis are angular)

B = Magnetic field

$\Delta\omega_B$ = Zeeman shift change in frequency

ΔE = Energy difference

μ_B = Bohr magneton

F = Total angular momentum

$F^{'}$ = Total angular momentum of excited state

g_F = Landé g-factor

m_F = z component of the total angular momentum F

$\Delta\mu$ = Difference in effective magnetic moments of the ground and excited state

v = Atom velocity

$a_{\text{max}} = \frac{\hbar k}{m}\frac{\Gamma}{2}$ = Maximum acceleration due to scattering

m = Mass of Yb

v_0 = Initial atom velocity

$B_{\text{bias}} = \frac{\hbar}{\Delta\mu}(\omega - \omega_a)$ = Bias magnetic field

$B_0 = \frac{kv_0\hbar}{\Delta\mu}$ = Magnetic field amplitude

F_{MOT} = MOT confining force

$\vec{E}$ = Electric field

$U_t(z)$ = Trapping lattice potential

e = Electron charge

$\vec{r}$ = Dipole vector

$\delta_{\ell a} = \omega_\ell - \omega_a$ = Detuning of lattice from atomic resonance

ω_ℓ = Trapping lattice frequency

ω_a = Atomic resonance frequency

k_ℓ = Trapping lattice wavenumber

R_c = Cavity mirror radius of curvature

L_c = Cavity length

$\Delta\omega_{\mathrm{LMS}}$ = Cavity longitudinal mode spacing

c = speed of light

$\Delta\omega_{\mathrm{TMS}}$ = Cavity transverse mode spacing

w_ℓ = Lattice Gaussian waist, $1/e^2$ intensity radius

V_ℓ = Lattice mode volume

R = Cavity mirror reflectivity (intensity)

Θ = Cavity mirror transmission (intensity)

$\mathcal{F}$ = Cavity finesse

I_{circ} = Circulating intensity inside cavity

I_i = Intensity input into cavity

κ = Cavity linewidth, full-width-half-max

$\Delta\omega$ = Detuning of light from nearest cavity longitudinal mode

k_B = Boltzmann constant

T = Atom temperature

$\chi^{(3)}$ = Third order optical susceptibility

ω_m = Modulation frequency

E_0 = Electric field amplitude

A_m = Modulation amplitude

J_n = Bessel function of order n

P_a = Atomic polarization

S = Signal

L_n = Lorentzian lineshape

D_n = Dispersive lineshape

ϕ = Phase

p = momentum

Ψ = Atomic wavefunction

E = Energy

$U_{t,0}$ = Amplitude of trapping lattice potential energy

λ_ℓ = Lattice wavelength

q = quasi-momentum

g = acceleration due to gravity

F_g = force due to gravity

r = Landau-Zener tunneling rate

ΔE = Band gap energy

T_B = Bloch period

ω_g = Bloch oscillation frequency due to gravity

σ_z = z Pauli matrix

$a, a^\dagger$ = photon ladder operators

η = Cavity pumping parameter

$\sigma_\pm$ = Two-state raising and lowering operators

ϵ_0 = Vacuum permittivity

g_0 = Single-atom-cavity-mode interaction frequency

$g^2(t)$ = Atomic back action on the light field

$\alpha(t)$ = Coherent state parameter

α_{ss} = Steady state value for the coherent state parameter

$c_1 = \frac{2mg_0^2}{\delta_{\ell a} k_\ell^2}$ = Scaled cavity depth

$c_2 = \frac{4m}{T_B k_\ell^2}$ = Scaled atomic function

k_0 = Scaled momentum

b_n = Atom wavefunction Fourier transfer momentum coefficients

SNR = Signal to noise ratio

ϵ = Oscillation contrast

E_R = Recoil energy

I_{nuc} = Nuclear spin

P = Pressure

λ_1 = Wavelength of Yb($^1\text{S}_0 \rightarrow ^1\text{P}_1$)

Γ_1 = Linewidth of Yb($^1\text{S}_0 \rightarrow ^1\text{P}_1$)

T_D = Doppler cooling limit temperature

λ = Wavelength

f_1 = Frequency of Yb($^1\text{S}_0 \rightarrow ^1\text{P}_1$)

Δf_1 = Isotope shift of Yb($^1\text{S}_0 \rightarrow ^1\text{P}_1$)

Γ_3 = Linewidth of Yb($^1\text{S}_0 \rightarrow ^3\text{P}_1$)

λ_3 = Linewidth of Yb($^1\text{F}_0 \rightarrow ^3\text{P}_1$)

f_3 = Frequency of Yb($^1\text{F}_0 \rightarrow ^3\text{P}_1$)

Δf_3 = Isotope shift of Yb($^1\text{F}_0 \rightarrow ^3\text{P}_1$)

$\dot{N}_a$ = Flow rate of atoms

n_0 = Atom number density

r_t = Radius of oven nozzle tube

L_t = Length of oven nozzle tube

N_t = Number of tubes in oven nozzle

$v_{\text{avg}} = \sqrt{\frac{8k_BT}{\pi m}}$ = Average velocity of thermal atoms in an oven

$\dot{N}_M$ = Flow rate of atoms through the MOT area

r_M = MOT capture region radius

L_M = Distance from oven nozzle to MOT

θ_e = Exit angle out of nozzle tubes

P_r = Pressure ratio

S_r = Pumping rate

C = Molecular conductance

d_d = Differential pumping tube diameter

L_d = Differential pumping tube length

$\bar{v} = \sqrt{\frac{k_B T}{m}}$ = Root mean square velocity in one dimension of a thermal distribution

$v_p = \sqrt{\frac{3k_B T}{m}}$ = Most probable velocity of an effusive thermal distribution

$\Delta\omega_D$ = Doppler shift

v_m = Maximum acceptance speed into Zeeman slower from oven

v_f = Final speed out of Zeeman slower into MOT

L_s = Length of Zeeman slower

θ_a = Absorption beam angle

k_3 = Wavenumber of Yb($^1\mathrm{F}_0 \rightarrow ^3\mathrm{P}_1$)

k_S = Spring constant

S_S = Surface area of a spring

Y = Young's Modulus

F_d = Driving force

b = Damping coefficient

ω_c = Critical driving frequency

$b_c = 2\sqrt{k_S m}$ = Critical damping coefficient

l = Mirror loss

σ_a = Absorption cross section

w_p = Camera effective pixel size

ρ_{col} = Atom column density

C_a = Atom picture pixel count

C_B = Background picture pixel count

N_a = Atom number

σ_i = Atom distribution Gaussian $1/e^2$ width in the i direction

σ_{v_i} = Atom thermal velocity spread in the i direction

T_i = Atom temperature in the i direction

σ_p = Standard deviation of laser power due to shot noise

$\mathcal{P}$ = Laser power

λ_p = Probe wavelength

d_{uniform} = Distance in lattice sites over which the atomic distribution remains uniform

$\Delta\phi$ = Phase shift of the probe lattice with respect to the trap lattice

U_p = Probe lattice depth

U_t = Trap lattice depth

ω_p = Probe frequency

ω_c = Bare cavity frequency

$\delta_{ca} = \omega_c - \omega_a$ = Detuning of atom resonance from bare cavity resonance

Ω = Collective vacuum Rabi frequency

$\mathcal{I}$ = Atom-probe overlap integral

$\Delta\omega_{\pm}$ = Cavity resonance frequency splitting

$\delta_{cp} = \omega_c - \omega_p$ = Detuning of probe frequency from bare cavity resonance

Θ_0 = Cavity mirror transmission amplitude

ρ = Normalized atomic number density

M = Cavity probe spatial intensity profile

k_p = Probe wavenumber

ω_t = Lattice trap frequency

Ψ_n = Simple harmonic oscillator (SHO) wavefunctions

H_n = Hermite polynomial

E_n = SHO energy eigenvalues

ρ_z = Atomic ensemble's spatial Boltzmann thermal distribution

$\langle n \rangle$ = Thermal occupation number

$\sigma_{r,\text{SHO}}$ = Width for a Gaussian potential approximated as a SHO

ρ_{PS} = Thermal phase space distribution

$\sigma_{r,\text{PS}}$ = Width for a Gaussian potential approximated by the phase space distribution

θ_t = Tilt angle of absorption beam

$T_z^{'}$ = Effective measured temperature in the presence of a tilt in the absorption beam

A = Atomic mass number

ρ_ϕ = Local dark matter density

λ_{dB} = deBroglie wavelength of dark matter

ϕ_0 = Oscillation amplitude of dark matter field

ω_ϕ = Dark matter field oscillation frequency

k_ϕ = Dark matter wavenumber

m_ϕ = Dark matter mass

v_ϕ = Dark matter galactic velocity

τ_{coh} = Dark matter field oscillation coherence time

G = Gravitational constant $\kappa_\phi = \sqrt{4\pi G}$

m_0 = Standard Model mass

d_g = Gluonic coupling coefficient of dark matter in the Standard Model

$\delta\omega_g$ = Precision on the frequency of Bloch oscillations

τ_{int} = Integration time of the experiment

R_{ph} = Rate of photon transmission

$\langle i \rangle$ = Average photocurrent

Δi = Shot noise on $\langle i \rangle$

Δf = Bandwidth of photodetector

Δi_{bin} = Shot noise per frequency bin

δg = Precision on the atomic acceleration

α = Bloch oscillation frequency amplitude due to dark matter

SNR_ϕ = Signal to noise ratio of dark matter signal

α_{min} = Minimum detectable α

P_{shot} = Power in the shot noise

$d_{g,\tau_{\text{coh}}>\tau_{\text{int}}}$ = Upper limit on gluonic coupling coefficient for DM coherence times longer than our integration time

$d_{g,\tau_{\text{coh}}<\tau_{\text{int}}}$ = Upper limit on gluonic coupling coefficient for DM coherence times shorter than our integration time

f = Fraction of the thermal atom sample loaded into the ground state

Acknowledgments

I wish to express my deepest gratitude to my advisor, Paul Hamilton, for his non-judgmental and encouraging nature throughout my research. Paul would always completely engage in conversations about whichever fundamental topic of physics I was thinking about at the time. We even had fun in our disagreements, as we never resolved the best way to simply describe Bloch oscillations. I will extend my thanks to the rest of my committee, Wes Campbell, Bob Cousins, and Eric Hudson, who also individually supported my quests for department equity, particle physics knowledge, and fundamental quantum physics explanations, respectively. I'd like to make an additional shout-out to two other department members, Smadar Noaz and Chair David Saltzberg, for both encouraging me to speak up, and for listening.

I was also surrounded by an incredible AMO community of graduate students who were beyond supportive. I cannot imagine having been as productive with my research without being able to bounce ideas around, borrow equipment, and occasionally go out for a beer with this cohort.

Near the beginning of graduate school I met my partner, Niko Rombes, who has been 100% supportive of every decision I have made, and helped me through the ups and downs of graduate school.

Thank you all.

Curriculum Vitae

2012 – 2014	Undergraduate Research under Prof. Enectalí Figueroa Feliciano. Particle Physics, Cryogenic Dark Matter Search, Massachusetts Institute of Technology (MIT).
2014	B.S. in Physics, MIT.
2015-2019	Teaching Assistant, Department of Physics and Astronomy, University of California, Los Angeles (UCLA).
2015	M.S., Physics, UCLA.)
2016-2020	Graduate Student Researcher under Prof. Paul Hamilton. Atomic Molecular Optics, UCLA.
2016-2018	Julian Schwinger Fellowship, Department of Physics and Astronomy, UCLA.

Publications and Presentations

Chandler Schlupf, Robert Niederriter, Eliot Bohr, Sami Khamis, Youna Park, Erik Szwed, Paul Hamilton, "Development of a force sensor using atom interferometry to constrain theories on dark matter and dark energy," (2017), APS Division of Atomic, Molecular and Optical Physics (DAMOP), Sacramento, CA, BAPS.2017.DAMOP.G5.5.

Chandler Schlupf, Robert Niederriter, Kayla Rodriguez, Paul Hamilton, "Progress towards a force sensor using Bloch oscillations to constrain dark matter theories," (2018), DAMOP, Ft. Lauderdale, FL, BAPS.2018.DAMOP.H06.6.

Chandler Schlupf, Robert Niederriter, Kayla Rodriguez, Paul Hamilton, "Progress towards non-destructive measurements of Bloch Oscillations as a force sensor to constrain dark matter

theories",
Frontiers in Matter Waves and Optics (FOMO), Crete, Greece.

Chandler Schlupf, Robert Niederriter, Paul Hamilton, "Progress towards Bloch Oscillations of Yb in an optical lattice to search for ultra-light dark matter," (2019,
Group on Precision Measurement and Fundamental Constants Poster Prize Winner
DAMOP, Milwaukee, WI.

Robert Niederriter, Chandler Schlupf, and Paul Hamilton, "Cavity probe for real-time detection of atom dynamics in an optical lattice", in preparation.

CHAPTER 1

Introduction

The dipole force from light on atoms can be used both to contain the atoms and to detect them. One form of containment for ultracold atoms that does not require additional electric or magnetic fields is the periodic potential created by an optical lattice. Deep and stable optical lattices are typically created with a laser and an optical cavity. Boundary conditions restrict the wavelength of light allowed in the cavity to the length of the cavity divided by a half integer, ensuring a zero electric field on the metallic surfaces. Only light of these specific wavelengths successfully enters and transmits through the cavity.

When atoms are present in the cavity, they cause a phase shift, changing which wavelengths are accepted into the cavity to maintain boundary conditions. This can be thought of classically as a path length difference of the light caused by the change in the index of refraction due to the atoms, or quantum mechanically as a two state system (the atom) coupled to damped driven quantum harmonic oscillator (light in the cavity). This enables use of the cavity transmission as a minimally invasive measurement tool for information on the presence of atoms in the cavity. See Figure 1.1 for a simple schematic.

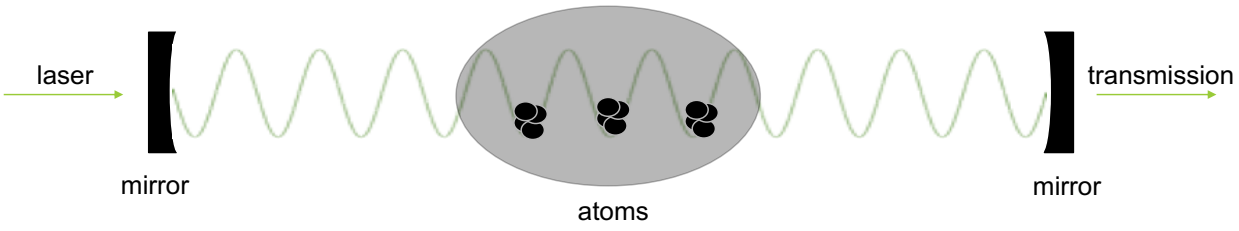

Figure 1.1: A simple schematic of a laser in a cavity, with atoms filling the potential wells created by the standing wave.

Within the last ten years atomic molecular optics (AMO) groups have started to exploit this feedback mechanism to study trapped atoms. Brahms and Stamper-Kurn [BBS12] use rubidium atoms in an optical cavity to study the relationship between motional excitations of the atoms and photon transmission frequency, ultimately quantifying the measurement backaction. Schleier-Smith and Vuletić [SLc10] use a similar technique to measure the level occupation of a two-level atom beyond the standard quantum limit by spin squeezing. Bohnet and Thompson [BCW13] show that under the right conditions atoms in a cavity can spontaneously synchronize and could be used as a gain medium for a sub-millihertz linewidth optical laser.

We look at this atom cavity interaction in two regimes: a deep lattice and a shallow lattice. Atoms confined to a deep lattice collect into individual lattice wells. When the average energy of the atoms is small compared to the lattice depth, the standing wave sinusoidal potential can be modeled as a simple harmonic oscillator (SHO) potential for the atoms. The quantum SHO is a much simpler system to solve than the sinusoidal potential. Across the lattice we have thousands of repeated harmonic oscillator wells filled with atoms that are all uniformly coupled to the lattice. Any feedback on the lattice from motion of atoms in a single well is amplified by thousands due to this repetition. We exploit this deep lattice uniformity to measure atomic motion immediately after release from the deep lattice by using another very shallow probe lattice. The feedback from the atomic motion on the probe lattice cavity transmission is used to measure the atomic sample's original temperature without losing the atoms.

Atoms in a shallow lattice, on the other hand, have wavefunctions spread out across multiple lattice cites. This enables them to undergo a process called Bloch oscillations [Blo29] (discovered by both Bloch and Zener, sometimes referred to as Bloch-Zener oscillations), which requires a periodic potential plus a uniform force (in our case, gravity). This phenomena produces atoms oscillating in space with a frequency directly proportional to the uniform force. Bloch oscillations were first observed by Feldmann and Leo [LFS93] 20 years after their prediction in a condensed matter system: electrons oscillating in a crystal lattice. Just

four years later an optical lattice was used by Dahan [BPR96] to observe cesium atoms undergoing Bloch oscillations. This system is highly advantageous because the lattice is easily tunable, and there are fewer scattering forces that decrease the oscillation coherence time. Since then Bloch oscillations have entered the field of laboratory-scale precision measurements. Cladé [CMC06] measures the recoil velocity of rubidium by transferring momentum to the atoms via Bloch oscillations to obtain a precision measurement of the fine structure constant. Tino [PWT11] use Bloch oscillations to precisely measure the force of gravity for testing gravitational redshifts and Newtonian law at micrometer scale. These experiments all measure their oscillations using the destructive time-of-flight technique to determine their sample's momentum distribution.

Due to our feedback on the lattice from the motion of the atoms, the Bloch oscillation frequency is imprinted directly on the transmission of the cavity, allowing for a real-time nondestructive measurement. Prasanna Venkatesh [PTH09] and Peden [PMC09a] discuss the theory of this nondestructive technique, which I review in my thesis. We will continue the trend of using Bloch oscillations for precision measurements by looking for the predicted small oscillating forces from ultralight dark matter.

This thesis starts by describing the theory of neutral atom cooling and trapping, broken up into our first two stages of cooling/trapping, the Zeeman slower and the magneto-optical trap, followed by trapping in an optical lattice. I then focus on the theory of Bloch oscillations necessary to understand one of our two applications: shallow lattice precision force sensor. The following chapter goes into technical details of the experimental apparatus. Chapter 4 first discusses results from our deep lattice temperature measurement, followed by projecting future sensitivities for our shallow lattice dark matter measurement. In the conclusion, I reflect on our progress towards observing Bloch oscillations, and discuss future plans for the experiment.

CHAPTER 2

Theory

2.1 Atomic Cooling and Trapping

Obtaining a gas of atoms cold enough to sit in the wells of an optical lattice requires an ultrahigh vacuum chamber with multiple stages of cooling. Cooling and trapping atoms led to the 1997 Nobel Prize for William Daniel Phillips, Claude Cohen-Tannoudji, and Steven Chu [AB20]. We still use their fundamental techniques today to obtain neutral atoms cold enough to load into an optical lattice.

2.1.1 Cooling

Interactions with the electromagnetic field allow us to use photons to apply forces and exert control on atoms. An atom can resonantly absorb a photon of a specific frequency, which is followed by spontaneous emission of a photon isotropically. After many absorptions and emissions, the average force is in the direction of the absorbed photons. This force from a beam of photons on an atom is simply the photon momentum times the rate of scattering. Each atomic transition has an intrinsic scattering rate (equivalent to its natural linewidth) Γ, but the rate of absorption also depends on the time spent in the ground or excited state. The scattering rate for an atom with saturation intensity I_s bombarded with a photon beam of intensity I and frequency detuning δ from an atomic resonance is

$$R_{\text{scatt}} = \frac{\Gamma}{2} \frac{I/I_s}{1 + I/I_s + 4\delta^2/\Gamma^2}. \tag{2.1}$$

This equation is only true for a two-state system. Atoms are quite complicated having many states, but typically the two-state system is an excellent approximation when the

laser frequency is close to a specific resonance and far from all of the others. The photon momentum is $\hbar k$, where k is the wavenumber, resulting in a scattering force of

$$F_{\text{scatt}} = \hbar k R_{\text{scatt}}. \tag{2.2}$$

With enough laser power ($I >> I_s$), the maximum force from a beam of photons is

$$\max(F_{\text{scatt}}) = \hbar k \Gamma/2. \tag{2.3}$$

The factor of two can be thought of qualitatively as occurring because half of the atoms are in the ground state while the other half are in the excited state at any given time.

The first part of the theory section addresses how the scattering force is used to slow atoms using a Zeeman slower and cool them using a magneto-optical trap. Next, I talk about how this force is used to confine atoms to the potential wells of an optical lattice. The second part discusses more complicated atom-light interactions that occur within the periodic potential set up by the lattice.

Zeeman Slower A beam of hot atoms is created by sublimating an elemental solid in an oven and allowing the gas to exit through a collimation tube. The Zeeman slower is a device that slows the beam of atoms using the scattering force from a counterpropagating laser beam of frequency ω. It exploits the Zeeman shift of atomic transitions with a specific magnetic field profile $B(z)$ to counter the Doppler shift of the light as the atoms change velocity while slowing down. The change in frequency of the atomic transition from the magnetic Zeeman shift is

$$\Delta\omega_B = \Delta E/\hbar = \frac{\mu_B B}{\hbar}(g_{F'} m_{F'} - g_F m_F) \equiv \frac{\Delta\mu B}{\hbar}, \tag{2.4}$$

where μ_B is the Bohr magneton, g_F is the Landé g-factor, m_F is the z-component of the magnetic field for the total angular momentum F, and I have defined $\Delta\mu$ as the difference in effective magnetic moments of the ground and excited state. To keep atoms on resonance with the laser one needs to satisfy the equation

$$\omega_a + \frac{\Delta\mu B(z)}{\hbar} = \omega + kv(z), \tag{2.5}$$

where v is the velocity of the atoms.

The maximum achievable acceleration follows from Eq. 2.3,

$$a_{\max} = \frac{\hbar k}{m}\frac{\Gamma}{2}, \tag{2.6}$$

where m is the atomic mass. Using this constant acceleration and simple kinematics, the velocity can be written as a function of distance

$$v(z) = v_0\sqrt{1 - \frac{2a_{\max}z}{v_0^2}}, \tag{2.7}$$

where v_0 is the initial atom velocity. Plugging this equation into Eq. 2.5 gives a functional form for the magnetic field needed to maintain resonance,

$$B(z) = B_{\text{bias}} + B_0\sqrt{1 - \frac{2a_{\max}z}{v_0^2}}, \tag{2.8}$$

where I have defined $B_{\text{bias}} = \frac{\hbar}{\Delta\mu}(\omega - \omega_a)$ and $B_0 = \frac{kv_0\hbar}{\Delta\mu}$. Qualitatively, B_{bias} is the magnetic field needed to keep the slow atoms on resonance with the highly detuned laser at the end of the slower, and $B_{\text{bias}} + B_0$ is the magnetic field needed to keep the fast atoms on resonance.

Magneto-Optical Trap A MOT uses a quadrupole magnetic field to create an imbalance in the scattering force from six red-detuned laser beams to spatially confine and cool atoms. The optical setup consists of three sets of red-detuned counter propagating beams along three perpendicular axes, see Figure 2.1(b). The atoms are trapped due to an effective spring force created by the combination of the scattering and the magnetic field gradient, and cooled by a dissipative force created by the scattering of the light. The qualitative picture is that when an atom has a velocity pointing away from the center of the trap, it will absorb and scatter a red-detuned photon coming from a counter propagating beam and on average are pushed back towards the center. The atom's resonance with the photon also has a spatial dependence due to the magnetic field. A typical MOT uses a transition from a spin zero ground state to a spin one excited state, allowing for three distinct Zeeman excited states, see Figure 2.1(a) for a visual. A quadrupole magnetic field has zero field in the center,

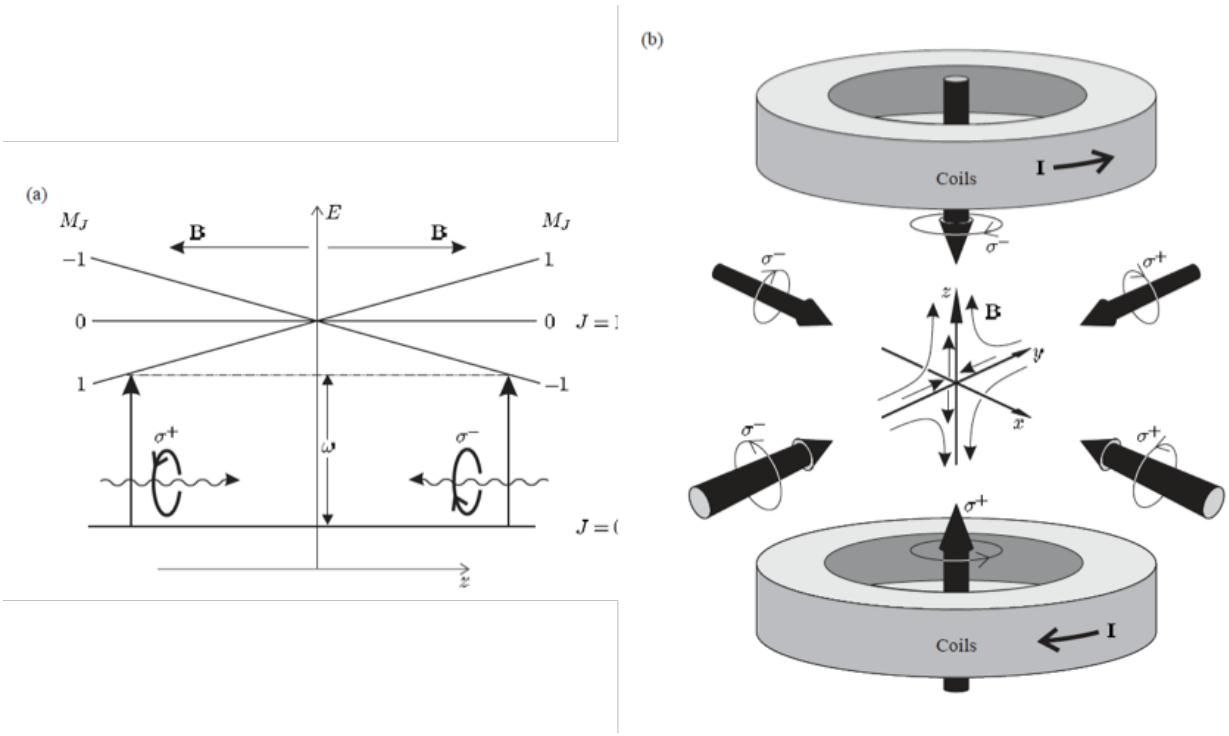

Figure 2.1: (From [Foo05].) Physics of the magneto-optical trap (MOT). (a) The quadrupole magnetic field creates a linear shift of the excited state Zeeman levels near the center of the trap. Counter propagating red-detuned beams of circular polarization ($\sigma^{\pm}$) induce scattering events if the atoms stray from the center of the trap. (b) A diagram of what a typical MOT consists of: three pairs of counterpropagating circularly polarized beams and a pair of coils in the anti-Helmholtz configuration provide the quadrupole magnetic field.

and a linearly increasing field close to the center. As an atom moves away from the center it gets Zeeman shifted by the linear field and becomes on resonance with the red-detuned laser beam, causing it to be pushed back towards the center. The correct choice of circular polarization for each beam ensures that atoms can only undergo a transition that pushes them back towards the center and will not be accelerated out of the trap.

Quantifying this effect, I consider the force caused by the scattering events while taking into account the Doppler shift and the Zeeman shift of the levels. Here I simply quote the results, but a full derivation of this force can be found in Sections 9.3-9.4 of [Foo05]. The

force exerted by the lasers in the small z regime is

$$F_{\mathrm{MOT}} = -2k\frac{\partial F_{\mathrm{scatt}}}{\partial \omega}v - 2\frac{g_\ell \mu_B}{\hbar}\frac{\partial F_{\mathrm{scatt}}}{\partial \omega}\frac{\mathrm{d}B}{\mathrm{d}z}z. \tag{2.9}$$

This equation consists of a restoring spring-like force from the magnetic field proportional to z, and a dissipative force from the scattering rate proportional to v.

2.1.2 Trapping

Optical Lattice Trap Optical lattices confine the atoms to an even smaller region than the MOT. An optical lattice consists of a standing wave of light created by counterpropagating laser beams of the same frequency. Besides the force from absorbing and emitting photons directly, if there is a gradient in the electric field there also exists a dipole force. Both of these forces can be derived starting from the potential energy of an atomic dipole with an electric field $\vec{E}$,

$$U_t(z) = \frac{1}{2}e\vec{r}\cdot\vec{E}, \tag{2.10}$$

where e is the unit of charge, $\vec{r}$ is the dipole vector of the atom, and the subscript t refers to this being the trapping potential. Without going into the details of the derivation, which can be found in Chapter 9 of Foot [Foo05], I quote the potential for an optical lattice far detuned from the atomic transition,

$$U_t(z) = \frac{\hbar\Gamma^2}{8\delta_{\ell a}}\frac{I}{I_s}\cos^2(k_\ell z), \tag{2.11}$$

where $\delta_{\ell a} = \omega_\ell - \omega_a$ is the difference between the lattice frequency ω_ℓ and atomic resonant frequency ω_a and k_ℓ is the wavenumber of the lattice light. Note that the dipole force scales as $1/\delta_{\ell a}$ while the scattering force scales as $1/\delta_{\ell a}^2$. This means if we go far enough detuned, we only need to consider the dipole force when looking at lattice dynamics. This scaling is important since in many situations one wants to avoid scattering, which destroys atomic coherence. A more thorough look at the atom-light interaction can be found in Section 2.2.2.

Optical Cavity Our optical lattice is formed by an optical cavity consisting of a pair of convex mirrors with radius of curvatures R_c and separation length L_c. Due to the boundary

conditions on the metal reflective mirror surfaces, only light with wavelength λ_c satisfying $L_c/\lambda_c \in \mathbb{Z}$ is permitted inside the cavity. (More accurately, assuming no mirror loss, light with wavelength λ_c is fully transmitted through the cavity, while off resonance light is transmitted with power following a Lorentzian curve with a specific linewidth as a function of detuning from the cavity wavelength). From this one can derive the distance between two permitted frequencies called the free spectral range or longitudinal mode spacing,

$$\Delta\omega_{\mathrm{LMS}} = \frac{\pi c}{L_c}, \tag{2.12}$$

where c is the speed of light. Transverse spatial modes describe the spatial profile of the beam using a combination of a Gaussian beam profile with a Laguerre polynomial. The transverse modes are also separated in frequency space by

$$\Delta\omega_{\mathrm{TMS}} = \Delta\omega_{\mathrm{LMS}}\sqrt{\frac{2L_c}{\pi^2 R_c}}. \tag{2.13}$$

The lowest order mode is a simple Gaussian profile with $1/e^2$ central waist radius of

$$w_\ell = \left(\frac{\lambda L_c}{\pi}\sqrt{\frac{2 - L_c/R_c}{4L_c/R_c}}\right)^{1/2}. \tag{2.14}$$

In the limit $R_c >> L_c$ satisfied by our experiment, the central waist can be approximated as the waist along the entire cavity, resulting in a Gaussian mode volume of

$$V_\ell = \frac{1}{4}\pi w_\ell^2 L_c. \tag{2.15}$$

This is the mode we use for all of our cavity experiments. (I switched to subscript "ℓ" for lattice since the waist and mode volume are properties of the lattice itself.)

After light enters the cavity, it bounces back and forth between the mirrors many times depending on the intensity reflectivity R of each mirror, with a chance each time of being transmitted (assuming no loss) of $\Theta = 1 - R$, where Θ is transmission (the more customary variable T is later used in this thesis for temperature). From the reflectivity, I can define the finesse,

$$\mathcal{F} = \frac{\pi\sqrt{R}}{1-R}, \tag{2.16}$$

which is useful when calculating the circulating power inside the cavity I_{circ} from inputting light of intensity I_i,

$$I_{circ} = \frac{2}{\pi} I_i \mathcal{F}. \tag{2.17}$$

The finesse is also useful when determining the linewidth of transmittable light,

$$\kappa = \frac{\Delta\omega_{\text{LMS}}}{\mathcal{F}} = c\frac{1-R}{L_c\sqrt{R}}. \tag{2.18}$$

The decay rate of light leaving the cavity, κ, is the full-width-half-max frequency space Lorentzian linewidth of transmission,

$$\Theta = \frac{1}{1 + \left(\frac{\Delta\omega}{\kappa/2}\right)^2}, \tag{2.19}$$

where $\Delta\omega$ is the frequency difference between the light and the nearest longitudinal mode.

2.1.3 Laser Stability

Laser frequencies need to be stabilized to well within the linewidth of the Yb transition in order to consistently cool, trap and measure the atoms. This can be performed with an external setup using the modulation transfer spectroscopy technique. This section begins with simpler laser locking techniques that were first implemented during the experimental setup. It continues with the theory and experimental setup for the modulation transfer spectroscopy.

Absorption Spectroscopy Absorption spectroscopy is the simplest type of spectroscopy that allows one to see the Yb resonance. When a laser at frequency ω is sent through a small cell containing hot Yb atoms and swept over a resonance of the atoms at ω_a, the atoms absorb the beam and there is a dip in the transmission. Because the Yb in the cell is not cooled, the resonance lines are heavily Doppler broadened. The natural linewidth of a transition has a Lorentzian lineshape of width Γ. Dominated by Doppler broadening, the linewidth instead looks like a Gaussian with half-width-half-max of $\omega_a\sqrt{\frac{2k_BT\ln 2}{mc^2}}$ [LHW97], where k_B is the Boltzmann constant, and T is the sample's temperature. This width can be

as high as 500 MHz in our absorption cell, compared to Yb's $^1S_0 \rightarrow ^1 P_1$ 29 MHz linewidth, which would limit our laser locking stability.

Saturation Absorption Spectroscopy Saturation absorption spectroscopy (SAS) is a technique that yields a signal with resolution on the order of the transition linewidth. Instead of using a single probe beam, it also uses a higher intensity pump beam of the same frequency, which is sent through the cell in the opposite direction as the probe. If, for example, the beams are red-detuned from the atomic transition, the pump will only address atoms Doppler shifted on resonance moving towards the beam. This also holds true for the probe beam, but since the beams are propagating in opposite directions, the two beams will be addressing different sets of atoms. The two beams will only address the same set of atoms, atoms moving perpendicular to both beam paths, when they are on resonance and not Doppler shifted. At this point, the pump beam excites this population of atoms leaving at most half of the sample in the excited state ('saturation'). As the probe beam interacts with this sample, the excited half of the atoms undergo stimulated emission. As stimulated emission is directional, this increases the transmission of the probe beam compared to the case when all atoms were in the ground state. The signal therefore looks like a large Doppler-broadened Gaussian dip, with a small Lorentzian peak in the center right on resonance.

Our experimental realization of this is shown in Figure 2.2. SAS yields a signal that is much narrower than the Doppler linewidth of the atoms. However the signal is difficult to use as a feedback signal because of its offset from zero and its strong dependence on the power in both the pump and probe; see Figure 2.3 for an example.

Modulation Transfer Spectroscopy Modulation transfer spectroscopy (MTS) is a more advanced technique that yields a signal at each atomic resonance on top of a flat background (as opposed to the Doppler broadened background of SAS). This is very useful when applying feedback to the laser, and is what we use to stabilize both our 399 nm and 556 nm lasers.

MTS again uses a pump and a probe beam, although in this technique they are approx-

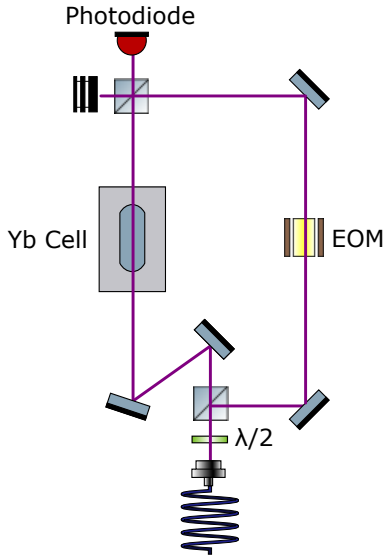

Figure 2.2: Modulation Transfer setup. Or without the electro-optic modulator (EOM), saturation absorption spectroscopy setup. The beam is split by the first PBS into a probe beam (transmission) and a pump beam (reflection). The probe beam is absorbed by a photodiode (PD).

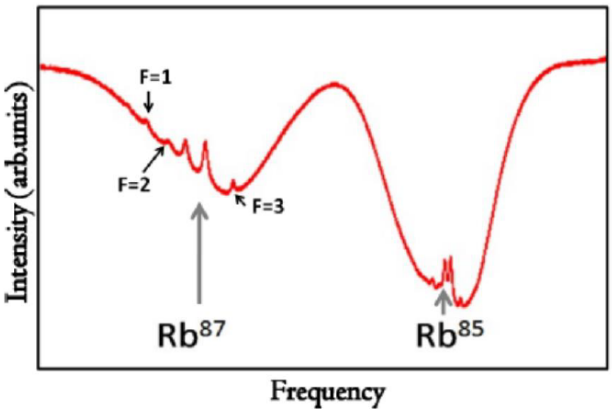

Figure 2.3: An example of a saturation absorption spectrum with rubidium on top of the Doppler broadened absorption dip. Due to the current global pandemic, I was unable to get a trace of our Yb SAS spectrum.

imately equal in power. To produce the desired error signal, the pump beam is frequency modulated to produce two side bands. The pump beam, one of its side bands, and the probe beam mix in the Yb cell to create a fourth beam in a process called four-wave mixing. Non-linear four-wave mixing occurs because of the vapor's $\chi^{(3)}$ susceptibility. The details of four-wave mixing are not necessary to understand the basics of this process. The output of the photodiode is mixed with the modulation signal and filtered. The mathematical description of this process is described next.

An electric field of frequency ω that undergoes frequency modulation at frequency ω_m can be expanded using Bessel functions,

$$\begin{aligned} |\vec{E}| &= E_0 \sin(\omega t + A_m \sin \omega_m t) \\ &= E_0 \big(\sum_{n=0}^{\infty} J_n(A_m) \sin(\omega + n\omega_m)t + \sum_{n=0}^{\infty} (-1)^n J_n(A_m) \sin(\omega - n\omega_m)t \big), \end{aligned} \tag{2.20}$$

where E_0 is the amplitude of the incoming wave, A_m is the size of the modulation, and J_n is the Bessel function of order n. When A_m is small ($A_m \ll 1$) only the $n = 0$ and $n = 1$ terms contribute to the sum, which corresponds to a wave propagating at the original frequency, ω, along with two sideband waves propagating at frequencies $\omega \pm \omega_m$. The Yb atoms act as a non-linear absorbing material and have a third order susceptibility. The probe sidebands beat with the probe beam to produce a signal at the modulation frequency, ω_m. The form of this signal is [Neg09]:

$$\begin{aligned} S(\omega_m) =& \frac{C}{\sqrt{\Gamma^2 + \omega_m^2}} J_0(A_m) J_1(A_m) \\ & \times [(L_{-1} - L_{-1/2} + L_{1/2} - L_1)\cos(\omega_m t) + (D_{-1} - D_{-1/2} + D_{1/2} - D_1)\sin(\omega_m t)], \end{aligned} \tag{2.21}$$

where

$$L_n = \frac{\Gamma^2}{\Gamma^2 + (\delta - n\omega_m)^2} \tag{2.22}$$

is the Lorentzian lineshape, and

$$D_n = \frac{\Gamma(\delta - n\omega_m)}{\Gamma^2 + (\delta - n\omega_m)^2} \tag{2.23}$$

is the dispersive lineshape. Γ is the natural linewidth of the transition and $\delta = \omega_a - \omega$. The sine term is often referred to as the quadrature component, and the cosine term the in-phase component.

This equation can be written in the form

$$S(\omega_m) = L(\omega_m)\cos(\omega_m t) + D(\omega_m)\cos(\omega_m t - \pi/2), \tag{2.24}$$

where the constants have been grouped together so that

$$L(\omega_m) = \frac{C}{\sqrt{\Gamma^2 + \omega_m^2}} J_0(A_m)J_1(A_m)(L_{-1} - L_{-1/2} + L_{1/2} - L_1) \tag{2.25}$$

and

$$D(\omega_m) = \frac{C}{\sqrt{\Gamma^2 + \omega_m^2}} J_0(A_m)J_1(A_m)(D_{-1} - D_{-1/2} + D_{1/2} - D_1). \tag{2.26}$$

The signal from the photodiode is then electronically mixed with the modulation signal, $\cos(\omega_m t + \phi)$, where ϕ is the phase difference between the signal at the detector and the applied modulation signal. This results in,

$$\begin{aligned} &S(\omega_m)\cos(\omega_m t + \phi) = \\ &L(\omega_m)(\cos(2\omega_m t + \phi) + \cos(\phi)) + D(\omega_m)(\cos(2\omega_m t + \phi - \pi/2) + \cos(\phi - \pi/2)). \end{aligned} \tag{2.27}$$

The signal is then sent through a low pass filter to obtain a final error signal given by,

$$S(\omega_m)\cos(\omega_m t + \phi) = L(\omega_m)\cos(\phi) + D(\omega_m)\cos(\phi - \pi/2). \tag{2.28}$$

Applying different phases creates a signal with different amounts of contribution from the Lorentzian and dispersive lineshape. With the right choice of ϕ, near resonance the signal is proportional to the detuning δ, and can be used to linearly feed back and keep the laser frequency locked to the resonance. A simulated example error signal can be seen in Figure 2.4. See Section 6.4 of the Appendix for information about the simulation code.

2.2 Bloch Oscillations

The standing waves of light from the optical lattice create a periodic potential for the atoms. Bloch's theorem gives a general solution for an atomic wavefunction in a periodic potential.

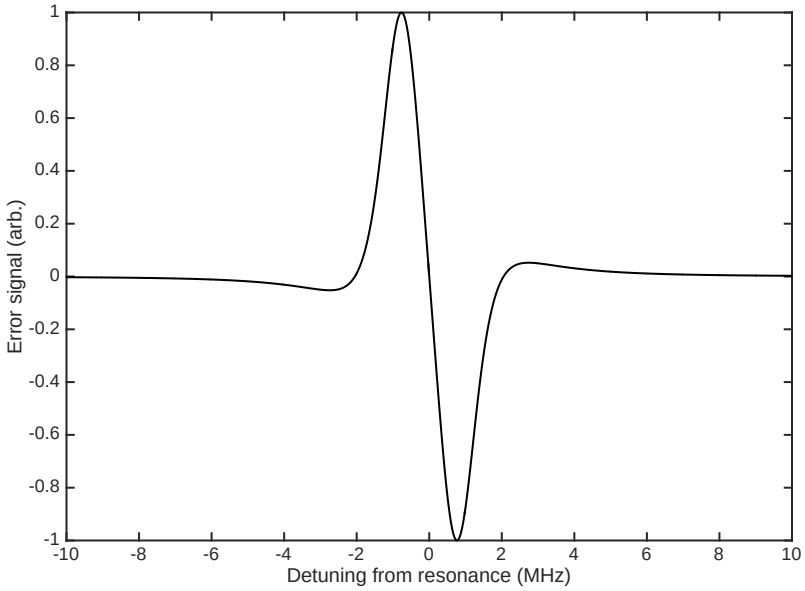

Figure 2.4: A simulated example of an error signal generated by MTS. This simulation was performed with a linewidth of 1 MHz and a driving frequency of 1 MHz.

With the addition of a uniform force (gravity and/or dark matter), atoms also undergo a phenomena called Bloch oscillations, which result in a oscillation frequency proportional to the applied force. Measuring this frequency using feedback from the atoms on the optical cavity transmission allows us to measure forces on the atoms. After reviewing the theory of Bloch's theorem and oscillations, I discuss the specific Hamiltonian of our atom-cavity coupled system. This simulation was used to determine the best optical parameters for our laser and cavity to optimize our measurement on dark matter.

2.2.1 Bloch's Theorem

The time independent Schrodinger equation for an atomic wavefunction is

$$\frac{p^2}{2m}\Psi + U_t(z)\Psi = E\Psi, \tag{2.29}$$

where p is the momentum, m is the atomic mass, $U_t(z)$ is the potential energy, Ψ is the atomic wavefunction, and E is the atomic energy. In a lattice, the potential will be periodic,

$U_t(z) = U_{t,0}(z + \lambda_\ell/2)$, where $\lambda_\ell/2$ is the spacing of a standing wave made from light of wavelength λ_ℓ. Bloch's theorem states that the solution to this equation is of the form [AM76b]

$$\Psi_q(z) = e^{iqz} u_q(z), \tag{2.30}$$

where $u_q(z)$ is some periodic function such that $u_q(z + \lambda_\ell/2) = u_q(z)$, and q is a quantity called the quasi-momentum.

Proof This proof is adapted from Chapter 8 of Ashcroft and Mermin [AM76a]. A periodic potential can be written as a Fourier series,

$$U_t(z) = \sum_n U_n e^{ig_n z}, \tag{2.31}$$

where U_n are the Fourier coefficients and $g_n = 2\pi n/a$ where $n = 0, 1, ..., N$ are the reciprocal lattice vectors. In the assumption that the lattice is large compared to the periodicity, I can apply Born-von Karman boundary conditions on the wavefunction, $\Psi(z + N\lambda_\ell/2) = \Psi(z)$, where N is the number of periods of the lattice. The atomic wavefunction can also be expanded as a Fourier series,

$$\Psi(z) = \int_k \Psi(k) e^{ikz} dk. \tag{2.32}$$

Using the boundary conditions,

$$\Psi(z + N\lambda_\ell/2) = e^{ikN\lambda_\ell/2} \int_k \Psi(k) e^{ikz} dk = \Psi(z), \tag{2.33}$$

it is clear that

$$k_{n'} = \frac{2\pi n'}{N\lambda_\ell/2} \tag{2.34}$$

for integer n'. $k_{n'}$ are the possible values of momentum for the atom in the periodic potential. This turns the integral into a sum,

$$\Psi(z) = \sum_{n'} C_{n'} e^{ik_{n'} z}. \tag{2.35}$$

This sum can be re-written as

$$\Psi(z) = \sum_{n,n'} C_{q_{n'} - g_n} e^{i(q_{n'} - g_n)z}, \tag{2.36}$$

where the substitution $k_{n'} = q_{n'} - g_n$ has been made. This momentum, $q_{n'} = \frac{2\pi n'}{N\lambda_\ell/2}$, is restricted to the first Brillouin zone to avoid over counting in the sum. The first Brillouin zone contains the integer values of $q_{n'}$ that fall between $-N/2$ and $N/2$.

The full Schrodinger equation can now be written as

$$\sum_{n'}\left[\sum_{n}\left(\frac{\hbar^2}{2m}(q_{n'}-g_n)^2+\sum_{n''}U_{g_{n''}}e^{ig_{n''}}-E\right)C_{q_{n'}-g_n}e^{i(q_{n'}-g_n)z}\right]=0. \tag{2.37}$$

Each value of $q_{n'}$ in the sum is a basis wavefunction that solves the Schrodinger equation,

$$\Psi_{q_{n'}}(z)=\sum_{n}C_{q_{n'}-g_n}e^{i(q_{n'}-g_n)z}. \tag{2.38}$$

Pulling out the constant exponential term reveals the form of the Bloch state,

$$\Psi_{q_{n'}}(z)=e^{iq_{n'}z}\sum_{g_n}C_{q_{n'}-g_n}e^{-ig_nz}\equiv e^{iq_{n'}z}u_{q_{n'}}(z). \tag{2.39}$$

2.2.2 Bloch Oscillations

Semi-Classical Model The lattice atoms not only experience the potential from the standing wave, but they also experience a constant force from gravity, $F_g = mg$. The full Hamiltonian is now

$$H=\frac{p^2}{2m}+U_t(z)+F_gz. \tag{2.40}$$

This constant force results in a phenomenon called Bloch oscillations. Bloch oscillations can be understood using a semi-classical argument.

The semi-classical model used to describe these oscillations can be justified by considering length scales. $U_t(z)$ has a periodicity of π/k_ℓ, where k_ℓ is on the order of $1/\mu$m, making the periodicity length scale much smaller than the change in the potential due to gravity over the same distance. $U_t(z)$ is therefore treated quantum mechanically to obtain the wavefunction, as was done above, and F_gz is treated classically to determine how the wavefunction changes with time. It is also important to note that the semi-classical model ignores transitions between different Brillouin zones; therefore the band index n which defines the Brillouin zone of the wavefunction is constant in time. This approximation holds true when the

Landau-Zener tunneling rate [Bal08],

$$r = e^{-\frac{m\lambda_\ell \Delta E^2}{4\hbar^2 F}} \tag{2.41}$$

is small, where ΔE is the band gap. In the limit of a shallow lattice, the band gap is directly proportional to the lattice depth, $\Delta E = 8U_t$. For our experimental parameters this tunneling rate is extremely small.

Because q is the good quantum number for this system, one can show that the classical velocity is given by $v(q) = \frac{1}{\hbar}\frac{dE}{dq}$. See Appendix E in Solid State Physics by Ashcroft and Mermin [AM76b] for a derivation of this result for periodic potentials. In order to see how a constant force changes the classical momentum q, first I expand $\frac{dq}{dz}$,

$$\frac{dq}{dz} = \frac{dq}{dt}\frac{dt}{dz} = \frac{dq}{dt}\frac{1}{v(q)}. \tag{2.42}$$

Next, I rearrange and substitute in for $v(q)$,

$$\frac{1}{\hbar}\frac{dE}{dq}\frac{dq}{dz} = \frac{1}{\hbar}\frac{dE}{dz} = \frac{dq}{dt}. \tag{2.43}$$

Classically, $\frac{dE}{dz}$ is simply the negative force in the z direction, which in this case is $-F_g$. This gives the change in momentum with respect to time as,

$$\frac{dq}{dt} = -\frac{F_g}{\hbar}. \tag{2.44}$$

Integrating this simple differential equation for momentum I get

$$q(t) = q(0) - \frac{F_g}{\hbar}t. \tag{2.45}$$

Assuming that the band index does not change, q plus a reciprocal lattice vector can be mapped back onto q : $\Psi_q(z) = \Psi_{q+g}(z)$. Therefore, $q(0) + \frac{2\pi}{a} = q(T_B)$, where T_B is the Bloch period. The Bloch period can then be solved for, obtaining

$$T_B = \frac{2\hbar k_\ell}{F_g}. \tag{2.46}$$

The frequency of Bloch oscillations due to gravity is therefore

$$\omega_g = \frac{2\pi}{T_B} = \frac{\pi F_g}{\hbar k_\ell}. \tag{2.47}$$

The Bloch oscillation frequency is proportional to the linear force applied. Therefore, measuring the Bloch oscillation is equivalent to measuring the applied force.

This semi-classical approach does a nice job of finding the Bloch oscillation frequency, but a more thorough quantum mechanical approach is needed to find the specific atomic dynamics. In addition, the light field itself changes in reaction to the atomic dynamics, which results in the need to solve coupled differential equations for the atoms and light.

Next I discuss the fundamental Hamiltonian used to model Bloch oscillations. This Hamiltonian leads to a pair of coupled equations between the atoms and the cavity light field. The pair of coupled equations are solved numerically in MATLAB to predict the experimental signal. The simulation is used to optimize this signal from a unknown force. The derivation of the coupled equations and the simulation model are followed from P.V. Balasubramanian's master's thesis [Bal08].

Quantum Mechanical Model The Hamiltonian for our system consists of terms for the atom, for the light, and for the atom-light interaction:

$$H = H_{\text{atom}} + H_{\text{light}} + H_{\text{int}}. \tag{2.48}$$

I model the atom as a two state system, so the atomic Hamiltonian consists of a kinetic energy term, a gravitational potential term, and an excitation energy term:

$$H_{\text{atom}} = \frac{p^2}{2m} + F_g z + \frac{\hbar\omega_a}{2}\sigma_z, \tag{2.49}$$

where σ_z is the Pauli matrix. The Hamiltonian for the light in the cavity consists of a photon energy term, a term for light leaking out of the top cavity mirror, and one for light being pumped in from the bottom cavity mirror:

$$H_{\text{light}} = \hbar\omega_\ell a^\dagger a - i\hbar\kappa a^\dagger a + i\hbar\eta(a^\dagger e^{-i\omega_\ell t} - a e^{i\omega_\ell t}), \tag{2.50}$$

where a is the photon ladder operator, $\eta = \sqrt{\kappa I_i}$ is the pumping parameter.

The interaction term is the dipole energy, or Stark effect, from Eq. 2.10,

$$H_{\text{int}} = \frac{1}{2} erE. \tag{2.51}$$

The dipole vector can be expanded as $r = \mu(\sigma_+ + \sigma_-)$, where $\mu = \left(c\epsilon_0\pi^2\Gamma^2\hbar^2/I_{sat}\right)^{1/2}$ is the electric dipole moment and $\sigma_\pm$ are the raising and lowering operators for the atomic two state system. The electric field can be written in terms of raising and lower operators as $|\vec{E}| = \sqrt{\frac{\hbar\omega_\ell}{2\epsilon_0 V_\ell}}(a + a^\dagger)\cos(k_\ell z)$, ϵ_0 is the vacuum permittivity.

Since we are using a cavity frequency that is close enough to resonance with our atomic transition, I can use the rotating wave approximation to simplify the interaction term: $H_{\text{int}} = \hbar g_0 \cos(k_\ell z)(a\sigma_+ + a^\dagger\sigma_-)$, where I have defined $g_0 = \mu\sqrt{\frac{\omega_\ell}{2\epsilon_0 V_\ell \hbar}}$ which is proportional to the single-atom-cavity-mode interaction frequency. Specifically, for this approximation to hold, I need $\omega_\ell + \omega_a >> |\omega_\ell - \omega_a|$, which can simultaneously be satisfied with the far-detuned condition earlier $|\omega_\ell - \omega_a| >> \Gamma$.

Because of this far-detuned condition, I can assume that fractional population in the excited state is very low ($R_{\text{scatt}} << \Gamma$). This allows us to derive a Hamiltonian that has adiabatically eliminated the excited state to obtain an effective Hamiltonian modeling the light-induced potential for the ground state of the atom. The details of this derivation are not shown, and the result is quoted from [Bal08]:

$$H = \frac{\hbar\omega_a}{2}\sigma_z + \frac{p^2}{2m} + F_g z + \hbar\omega_\ell a^\dagger a - \frac{\hbar g_0^2\cos^2(k_\ell z)a^\dagger a}{\delta_{\ell a}}\sigma_z - i\hbar\eta(ae^{i\omega_\ell t} - a^\dagger e^{-i\omega_\ell t}) - i\hbar\kappa a^\dagger a, \quad (2.52)$$

where the detuning is $\delta_{\ell a} = \omega_\ell - \omega_a$. Here we can see the expected scaling of the Stark shift $g_0^2/\delta_{\ell a}$.

Next, I make a unitary transformation, $U_u = e^{\left(it\omega_\ell(a^\dagger a + 1/2\sigma_z)\right)}$, that allows us to express the Hamiltonian in terms of the the detuning of the light:

$$H = \frac{\hbar\delta_{\ell a}}{2}\sigma_z + \frac{p^2}{2m} + F_g z - \frac{\hbar g_0^2\cos^2(k_\ell z)a^\dagger a}{\delta_{\ell a}}\sigma_z - i\hbar\eta(a - a^\dagger) - i\hbar\kappa a^\dagger a. \quad (2.53)$$

With this Hamiltonian, I can second-quantize the atomic wavefunction and derive the equations of motion using the Heisenberg equation of motion equations $i\hbar\dot{\Psi} = [\Psi, H]$ and $i\hbar\dot{a} = [a, H]$. We assume that the light is in a coherent state with coherent parameter α, which is valid for laser light. Without explicitly deriving them here, I get the coupled equations:

$$i\hbar\dot{\Psi} = \left(-\frac{\hbar^2}{2m}\partial_z^2 + U_t(t)\cos^2(k_\ell z) + F_g z\right)\Psi \quad (2.54)$$

$$\dot{\alpha} = -i\frac{\alpha}{\delta_{\ell a}}g^2(t) + \eta - \kappa\alpha, \tag{2.55}$$

where I have defined two useful parameters: the atomic back action on the field is defined as

$$g^2(t) = g_0^2 \int |\Psi|^2 \cos^2(k_\ell z) dz, \tag{2.56}$$

and the lattice depth as a function of time as

$$U_t(t) = \frac{\hbar g_0^2}{\delta_{\ell a}} \alpha^*(t)\alpha(t). \tag{2.57}$$

2.2.3 Simulation

The basic steps of the simulation are: 1) Determine the initial $\alpha(0)$ and $\Psi(0)$ values, 2) determine $\alpha(t + \Delta t)$ and $\Psi(t + \Delta t)$ as functions of $\alpha(t)$ and $\Psi(t)$, 3) incrementally step α and Ψ forward in time by amount Δt.

I begin by examining the evolution of the coherent parameter, starting with Eq. 2.55. I can assume for a small enough time step Δt, $g^2(t)$ is approximately a constant. This equation can then be separated and directly integrated,

$$\int_{\alpha(t)}^{\alpha(t+\Delta t)} \frac{d\alpha}{\eta - \alpha(ig^2/\delta_{\ell a} + \kappa)} = \int_t^{t+\Delta t} dt. \tag{2.58}$$

Therefore the time evolved α is

$$\alpha(t + \Delta t) = \frac{\eta}{\kappa} \frac{1}{ig^2/(\delta_{\ell a}\kappa) + 1} \left(1 - e^{(-ig^2/\delta_{\ell a} + \kappa)\Delta t}\right) + \alpha(t) e^{(-ig^2/\delta_{\ell a} + \kappa)\Delta t}. \tag{2.59}$$

I find the steady state value of the parameter by setting the time derivative to zero in the differential equation, obtaining

$$\alpha_{ss} = \frac{\eta}{\kappa} \frac{1}{-ig^2/(\delta_{\ell a}\kappa) + 1}, \tag{2.60}$$

which can be used as a good approximate guess for the initial value of α.

The plan for the wavefunction is to transform it into momentum space, and calculate the time evolution for the coefficients of the momentum eigenstates. For the physical system, I use Born-Von Karmann (BVK) periodic boundary conditions on the wavefunction which

discretizes the momentum. I say that the system has size $L = N\pi/k_\ell$, N wavelengths of the periodic potential. Using Bloch theory analysis, this restricts the allowed values of the momentum from Eq. 2.34.

At this point I make a variety of definitions to simplify the equation and make it dimensionless. I can set $k_\ell z = x$ and $\bar{t} = t/T_B$, where T_B is the Bloch period. I also use $c_1 = \frac{2mg_0^2}{\delta_{\ell a} k_\ell^2}$ and $c_2 = \frac{4m}{T_B k_\ell^2}$ to scale the cavity depth and atomic function respectively, reducing the equation to

$$\left(-\frac{\partial^2}{\partial x^2} + c_1\alpha^*\alpha\cos^2(x) + c_2 x\right)\Psi(x,t) = i\frac{c_2}{2}\Psi(x,t). \tag{2.61}$$

Next, I make a simplifying transformation, $\Psi(x,\bar{t}) = \tilde{\Psi}(x,\bar{t})e^{-2i\bar{t}x}$ and expand the new field in momentum space using

$$\tilde{\Psi}(x,\bar{t}) = \sum_n b_n(\bar{t})e^{ink_0x}, \tag{2.62}$$

where in the new dimensionless variables, $L = N_0\pi$ and the allowed values of the momentum are multiples of $k_0 = 2\pi/L$. I now have a differential equation for the momentum state coefficients of the wavefunction,

$$b_m(mk_0 - 2\bar{t})^2 + \frac{1}{4}c_1\alpha^*\alpha(2b_m + b_{m-N_0} + b_{m+N_0}) = i\frac{c_2}{2}\frac{db_m}{d\bar{t}}. \tag{2.63}$$

For the numerical simulation, I have to make a choice of how many momentum states to keep in order to make the calculation finite. This equation can be written in matrix notation as

$$A\vec{b} = i\frac{c_2}{2}\frac{d\vec{b}}{d\bar{t}},$$

where $\vec{b} = [b_1, b_2, ...]$ and the matrix A is (take $N_0 = 1$ for this example)

$$A = \begin{bmatrix} (mk_0 - 2\bar{t})^2 + c_1\alpha^*\alpha/2 & c_1\alpha^*\alpha/4 & 0 & \cdots \\ c_1\alpha^*\alpha/4 & (mk_0 - 2\bar{t})^2 + c_1\alpha^*\alpha/2 & c_1\alpha^*\alpha/4 & \cdots \\ 0 & c_1\alpha^*\alpha/4 & (mk_0 - 2\bar{t})^2 + c_1\alpha^*\alpha/2 & \cdots \\ \vdots & \vdots & \vdots & \ddots \end{bmatrix}. \tag{2.64}$$

This equation can be solved incrementally by $b(\bar{t}+\Delta\bar{t}) = \exp\left(-\frac{i\Delta\bar{t}A}{c_2/2}\right)b(\bar{t})$. The initial vector of momentum coefficients can be approximated by the eigenvector of A corresponding to the lowest eigenvalue.

After the momentum vector has been found, I can use it to calculate the atomic back action in momentum space using

$$\langle\cos(x)\rangle = \sum_n \frac{|b_n|^2}{2} + \frac{1}{4}b_n^*(b_{n+N_0} + b_{n-N_0}). \tag{2.65}$$

I can plug that back into $\alpha(t+\Delta t)$ for the next optical time step, and use the new value of α to get a new Hamiltonian and calculate the next atomic time step.

Results The simulation was used to determine the maximum signal to noise ratio possible by optimizing the lattice depth given our expected experimental parameters. The signal to noise ratio (SNR) is the power in the Bloch oscillation frequency divided by the power in the noise. The signal to noise ratio scales linearly with the contrast of the oscillations, ϵ. Here we only consider noise due to shot noise, so the SNR scales as the square root of the laser intensity into the cavity, I_i.

I fixed the scattering rate to $R_{\text{scatt}} = 1$ Hz to allow 1 s of coherent Bloch oscillations. Setting the lattice depth and the scattering rate fixes the cavity detuning and the input intensity. Given those restrictions, I scanned the lattice depth and observed that the SNR decreased for increased lattice depth. Figure 2.5 shows the simulation results for a variety of lattice depths. Although decreasing the lattice depth increases the SNR, the lattice depth eventually becomes too small to confine the atoms against gravity, and the oscillations are obscured, see Figure 2.5(a). A lattice depth amplitude of $U_{t,0} = 3E_R$, where $E_R = \frac{(\hbar k_\ell)^2}{2m}$ is the recoil energy of the atom, was found to be a good compromise between SNR and lack of confinement. This leads to a detuning of $\delta_{\ell a} = -2\pi\cdot 2$ GHz, an intensity of $I_i = 130$ mW and a contrast of $\epsilon = .03$. See Section 6.4 in the Appendix for information about the simulation code.

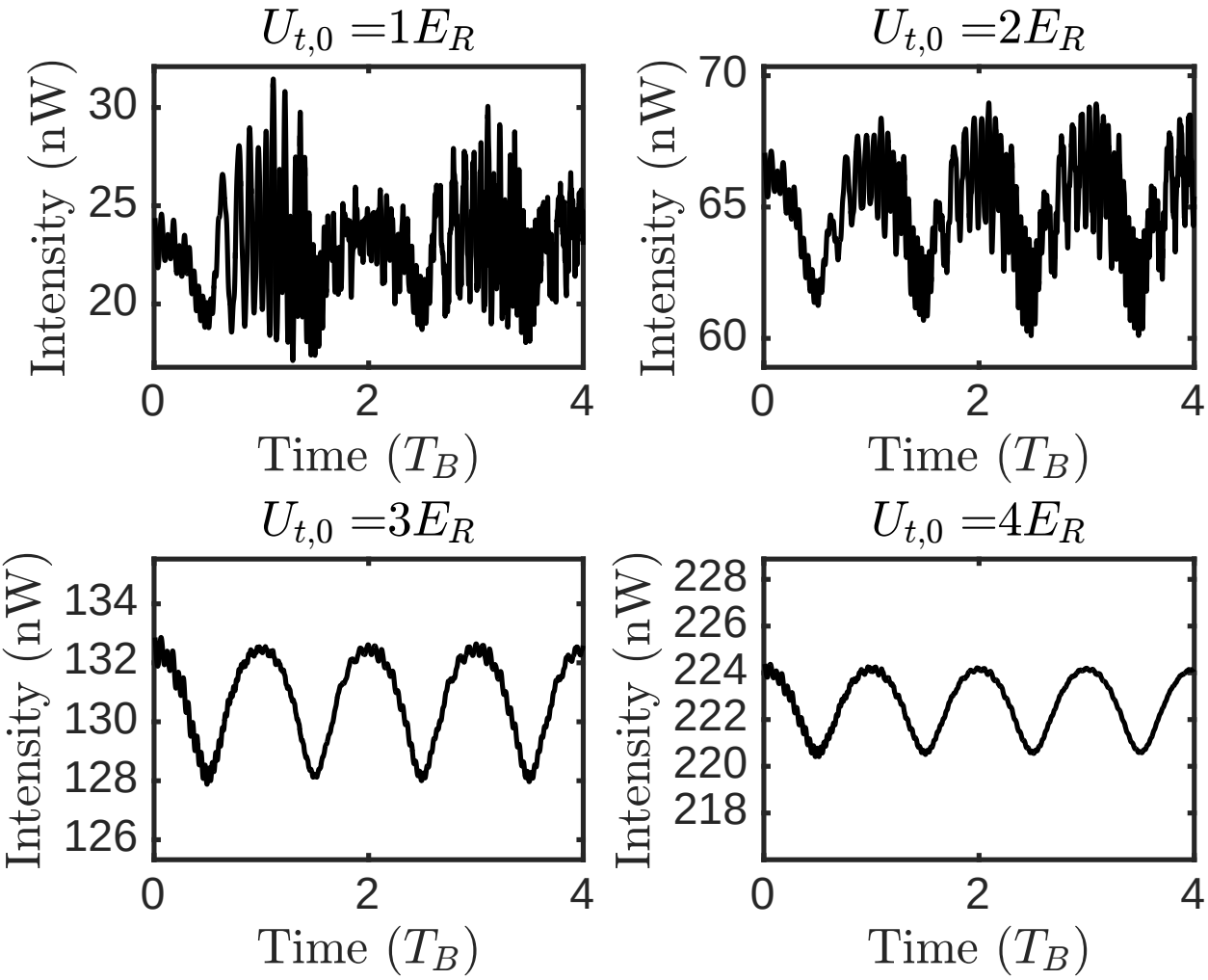

Figure 2.5: Simulation results. Each figure shows the expected laser intensity transmitted by the cavity assuming 100% transmission, with varying lattice depths for the atoms undergoing Bloch oscillations due to gravity.

CHAPTER 3

Apparatus

3.1 Atoms

3.1.1 Ytterbium

When choosing an atomic species to work with in a neutral atom lab, the most important property an atom can have is a cycling transition. Cycling transitions allow many repeated photon scatters at a single laser frequency, which is necessary for efficient slowing and cooling. Atoms with one or two valence electrons typically have accessible cycling transitions; some common alkalis (one valence electron) used in neutral atom labs are rubidium and cesium, and a common alkaline-earth (two valence electrons) is strontium. Ytterbium, a lanthanide, is also commonly used due to being alkaline-earth-like; having two valence electrons.

Each species has different benefits to exploit for different science goals, for example rubidium has a particularly rich Feshbach resonance spectrum, an essential feature for the control of quantum-degenerate gases [CGJ10]. Our experiment focuses on achieving low-background measurements in search for new fundamental physics. Because strontium and ytterbium have two valence electrons, their ground state S levels have no net orbital or spin angular momentum. This causes them to be particularly magnetically insensitive, which helps eliminate one possible background systematic from environmental magnetic field fluctuations for future measurements. In our experiment we plan on achieving high sensitivity by holding our atoms in an optical lattice and observing Bloch oscillations. Low atom-atom interactions allow for both another elimination of a possible background systematic, and for long hold times in the lattice allowing for long measurement integrations. Ytterbium 171

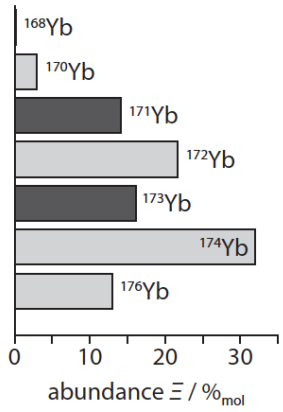

Figure 3.1: Natural abundance of stable Yb isotopes. Light gray isotopes are bosonic, and dark gray fermionic. [D13]

has an extremely low ground-state (S-wave) self-scattering cross section of order 10^{-19} m^2 [KEK08]. These favorable properties, along with others such as the rich isotope spectrum, led us to choose Yb for our experiment.

Isotopes One of the benefits of working with Yb is that it has a large variety of naturally-abundant stable isotopes; see Figure 3.1. This variety allows us to choose between fermionic or bosonic atoms, and between atoms with different nuclear spin states. With a nuclear spin of $I_{\text{nuc}} = 0$, ^{174}Yb lacks ground state structure. Because of that and its high natural abundance, ^{174}Yb has the highest MOT loading rate and tends to be the easiest to work with. However, we plan on doing our Bloch oscillation experiment with ^{171}Yb because of its extremely low self cross section, four orders of magnitude lower than that of ^{174}Yb, allowing for longer lattice hold times. The hyperfine structure of ^{171}Yb, due to a nuclear spin of $I_{nuc} = 1/2$, allows for the use of a "magic lattice", where both the ground state and excited state of the atom are equally trapped. Note that the ground state of ^{171}Yb has total angular momentum $F = 1/2$, and the excited state is split into $F' = 1/2$ and $F' = 3/2$.

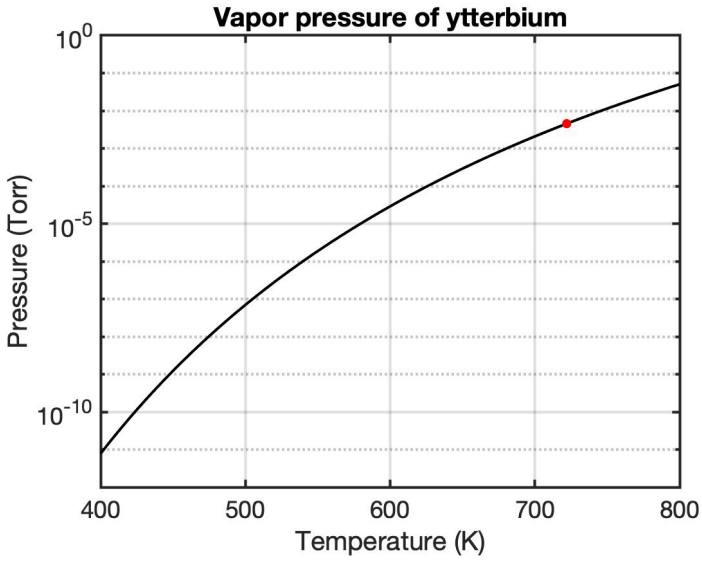

Figure 3.2: The vapor pressure for ytterbium; see Eq. 3.1 . The red circle indicates where we usually sit on this curve.

Vapor Pressure One drawback to using Yb is that the oven used to produce a gaseous beam of atoms needs to be kept at a very high temperature to maintain a workable vacuum pressure; see Figure 3.2. The vapor pressure for Yb is

$$\log_{10}(P/\text{Pa}) = 5.006 + 9.111 - 8111\text{K}/T + 1.0849\log_{10}(T/\text{K}), \tag{3.1}$$

where T is in Kelvin [Wik19]. Our oven is kept at 450° C to maintain a vacuum pressure for Yb of order 10^{-3} torr, while rubidium for example only needs to be heated to 50° C to achieve similar pressures.

Electronic Properties Ytterbium has two transitions we use for dual-stage cooling. A diagram of the relevant transitions can be seen in Figure 3.3.

The singlet transition ${}^1\text{S}_0 \rightarrow {}^1\text{P}_1$ at $\lambda_1 = 399$ nm obeys all of the selection rules for an electric dipole transition. It thus has a broad transition linewidth of $\Gamma_1 = 2\pi \cdot 29.1$ MHz and is used for our first stage of cooling, the Zeeman slower. The broad transition would only

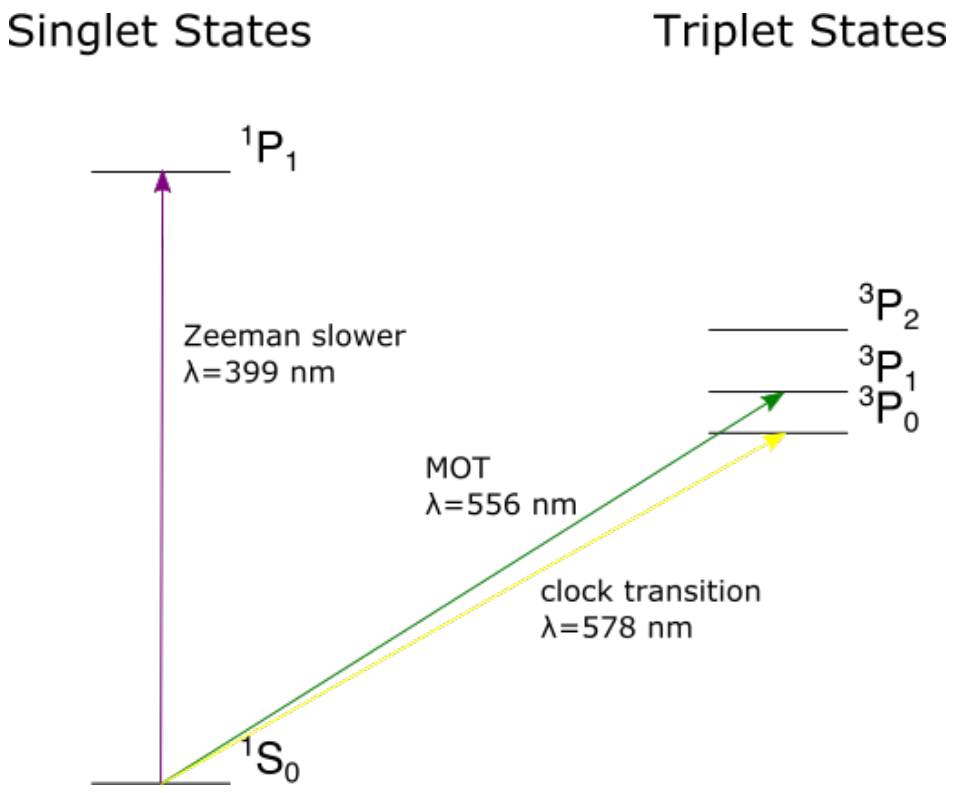

Figure 3.3: Level diagram for ytterbium showing the relevant states for our experiment. The states are labeled using the convention $^{2S+1}L_J$, where S is the total spin, L is the orbital angular momentum and J is the total angular momentum.

allow us to cool to 700 μK due to the Doppler cooling limit scaling with linewidth:

$$T_D = \frac{\hbar\Gamma}{2k_B}. \tag{3.2}$$

The saturation intensity also scales with linewidth,

$$I_s = \frac{\pi ch\Gamma}{3\lambda^3}, \tag{3.3}$$

and for this transition is 60 mW/cm^2. The transition wavelength 399 nm is produced by a doubled Ti:Sapphire laser, with an absolute frequency of $f_1 = 751525987$ MHz for ^{174}Yb and isotope shifts of $\Delta f_1(1/2 \to 1/2) = 1153$ MHz and $\Delta f_1(1/2 \to 3/2) = 832$ MHz for the two excited states of ^{171}Yb.

The three available triplet states, $^3\mathrm{P}_{0,1,2}$, break at least one of the electric dipole selection rules, and therefore have narrower linewidths than the singlet transition. Of the three, the broadest linewidth of $\Gamma_3 = 2\pi \cdot 182$ kHz is on the intercombination $^1\mathrm{S}_0 \to ^3\mathrm{P}_1$ transition, making it a good choice for balancing the fast photon cycling needed in a MOT and the lower Doppler cooling limit. The intercombination transition has a much smaller Doppler cooling limit of 4 μK and saturation intensity of 0.13 mW/cm^2. The transition wavelength is $\lambda_3 = 556$ nm and is produced by a doubled diode laser, with an absolute frequency of $f_3 = 539385610$ MHz for ^{174}Yb and isotope shifts of $\Delta f_3(1/2 \to 1/2) = -1177$ MHz and $\Delta f_3(1/2 \to 3/2) = 4759$ MHz for the two excited states of ^{171}Yb. Yb also has an available clock transition from $^1\mathrm{S}_0 \to ^3\mathrm{P}_0$ which is not used in this experiment, but could be useful for future applications.

Magnetic Properties In the weak field regime (where L-S coupling holds — see Chapter 6 in [Foo05]), a state's energy is shifted by $\Delta E = g_F \mu_B B m_F$ (see Section 2.1.1).

The contribution to the total angular momentum F in the ground states of both isotopes is solely from the nuclear magnetic moment, which is suppressed by three orders of magnitude compared to the electronic magnetic moment. The ground state shift of ^{174}Yb is precisely zero in this coupling scheme as it has $m_F = 0$. For ^{171}Yb the ground state g-factor is $g_F(F = 1/2) = -2.282 \cdot 10^{-4}$. The g-factors for the excited states are listed in Table 3.1.

	$g_F(^1P_1)$	$g_F(^3P_1)$
^{171}Yb F$'$= 1/2	1.380	1.990
^{171}Yb F$'$= 3/2	.690	.995
^{174}Yb F$'$= 1	1.035	1.493

Table 3.1: (Experimentally measured) Landé g-factors for the excited states of transitions from the S ground state for ^{171}Yb and ^{174}Yb[D13].

3.1.2 Oven

The oven converts solid ytterbium chunks into a beam of Yb atoms aimed at the MOT capture region. Our oven design is extremely simple, but also functional and reliable. It consists of ytterbium pieces, ranging from flakes to centimeter sized chunks, placed inside of a nipple with a blank flange on the back end, and a nozzle on the other. 316 stainless steel vacuum parts and silver gaskets[1] are used, both to minimize corrosion from Yb. The nipple and nozzle are covered with layers of UHV foil, wiring, and insulation. The resistance wire used is 21 AWG solid ceramic braid insulated wire with a temperature rating of 1200°C[2]. The insulation is made of ceramic fiber and is rated to 1300°C. The wire is split into a section around the nozzle and a section around the oven so that the temperatures can be controlled independently. It was important that the nozzle stayed as hot or hotter than the oven so the Yb did not condense and clog the holes.

There are various nozzle designs used by the community, ranging from a simple single hole drilled into a blank flange, to a set of hundreds of micro-capillary tubes [SRG15]. We decided to go with a fairly simple design to start, and have continued researching more advanced designs to increase our atomic flow rate into the MOT region.

An ideal nozzle has a tube radius and length chosen to maximize the flow rate of the

[1]Lesker Company, GA-0275NSP

[2]PelicanWire, P2721A875CB

atoms arriving in the capture region of the MOT, while not wasting Yb in order to maintain a long oven lifetime. The flow rate of atoms out of a long skinny tube is

$$\dot{N}_a = \frac{2\pi}{3}\frac{n_0 v_{\text{avg}} r_t^3}{L_t} N_t, \tag{3.4}$$

where n_0 is the number density of atoms, r_t is the radius of the tube, L_t is the length of the tube, N_t is the number of tubes and $v_{\text{avg}} = \sqrt{\frac{8k_BT}{\pi m}}$ is the average velocity of atoms in the oven[GW60]. For ballistic flow the rate of atoms reaching the MOT at the other end of the vacuum chamber is the ratio of areas of the atomic beam size and the MOT region multiplied by $\dot{N}_a$,

$$\dot{N}_M = \dot{N}_a \frac{\pi r_M^2}{\pi r_t^2} = \dot{N}_a \frac{r_M^2/L_M^2}{r_t^2/L_t^2}, \tag{3.5}$$

where $r_M = 1.5$ cm is the radius of the MOT capture region, and $L_M = 110$ cm is the distance from the tube to the MOT. Here I have used the small angle approximation $\tan\theta_e = r_t/L_t \approx \theta_e$ where θ_e is the exit angle out of the nozzle tubes. The optimal tube size would have 100% of the atoms entering the MOT region, $\dot{N}_a = \dot{N}_M$, which would lead to a relationship between the tube radius and length: $r_t = \frac{r_M}{L_M} L_t$. For ease of manufacturing our "tube" was constructed by drilling holes into a blank flange of length $L_t = 12.7$ mm, which results in an optimized tube radius of $r_t = .2$ mm. Due to manufacturing constraints, our final design has a tube size of $r_t = .5$ mm. Observing that the number of atoms entering the MOT region scales with N_t, we added four extra holes of the same radius each 1.5 mm away from the center hole. The number of extra holes and the distance from the center were also chosen based on machining constraints.

The oven is heated from the outside using resistance wire to 450°C resulting in a vapor pressure of $P = 5 \cdot 10^{-3}$ torr (see Fig. 3.2), while the nozzle is kept at 550°C to avoid clogging. This vapor pressure can be converted into a number density via $n_0 = \frac{P}{k_BT} = 7 \cdot 10^{10}$ atoms·mm^{-3} which results in a flow rate out of our nozzle of $\dot{N}_a = 2 \cdot 10^{15}$/s. With an estimate of our machine running 10 hours on weekdays (the oven automatically turns on and off so this is a good estimate), this leads to an ytterbium consumption of 5 grams/year. With an input of (at least) 25 grams, we expect to run out no earlier than late 2022.

3.2 Cooling

3.2.1 Laser Systems

The slower and the MOT require two laser wavelengths, 399 nm and 556 nm respectively. In order to effectively and consistently address the two transitions, each laser must be capable of a frequency stability much less than the linewidth of the respective transition. This is accomplished both by internal relative stability components of each laser system, as well as external absolute stability to the specific Yb transition frequency. I start by discussing some of the common tools and techniques we use to control our lasers, then I describe each laser individually and how we use those tools for stability.

Tools and Techniques We use modulation transfer spectroscopy (MTS), described in Section 2.1.3, to lock both of our Yb transition lasers. For these MTS locking systems, we use an electro-optic modulator (EOM) to provide phase modulation to our beam. We use broadband EOMs with AR coatings to limit reflections[3]. The EOM drive amplitude needs to be on the order of tens of volts to obtain sufficient phase modulation, and a tank circuit to match the 50 Ω input impedance at the desired modulation frequency is necessary to minimize back reflection of the RF signal. Details of this circuit are in Appendix 6.2.

EOMs naturally have some birefringence, so it is important to align the laser polarization along a single axis of the EOM crystal to limit polarization modulation, which is translated to amplitude modulation after a PBS. We also found that temperature stabilizing the EOMs is crucial to limit polarization modulation on the output.

Other than providing sidebands for stability, these sidebands can be used directly as frequency shifted light. We use a fiber EOM[4] to provide 556 nm light shifted up to 6 GHz away from the Yb resonance for our optical cavity. Our cavity acts as a filter allowing only the first order at the modulation frequency to transmit, and blocks the on-resonance zero

[3]Thorlabs, EO-PM-NR-C4

[4]AdvR, WPM - K0556 - P48P48AL0

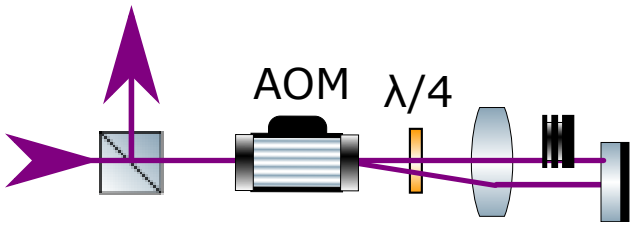

Figure 3.4: Typical double pass AOM configuration. A beam is sent in through a PBS and deflected by the AOM. The deflected beam then goes through a lens and retroreflected back by a mirror. This allows the angle of the deflection to be changed without changing the retroreflected alignment of the beam back through the AOM. The beam passes through a quarter-wave plate twice, changing its polarization by $\lambda/2$, allowing it to get reflected by the initial PBS. To ensure the beam remains collimated, the distance from the AOM to the lens, and from the lens to the mirror, are both the focal length of the lens. We typically reach an efficiency of 50%.

order that would cause Yb heating. Similarly, it is important to temperature control the fiber EOM for maximum efficiency.

A different tool, the acousto-optical modulator (AOM) is used when the frequency modulated beam needs to be physically separated from the zeroth order. The angle at which the beam is separated depends on the modulation frequency, which could cause problems with alignment when sweeping over frequencies, for example in the 532 nm locking setup, Section 3.2.1. This challenge is overcome by using a simple clever optical set up that sends the beam through the AOM twice [DHL05]. This double-pass configuration can be seen in Figure 3.4. We are typically able to get 50% efficiency through this setup, with improvements when optimizing for beam size and focus through the AOM.

399 nm Laser Our continuous wavelength (CW) 399 nm light comes from a doubled Ti:Sapphire laser[5]. As the name suggests, the lasing medium consists of a sapphire crystal

[5]Entire laser system, including Ti:Sapph, external cavity doubler, and pump were purchased and installed by M-Squared Lasers

(Al_2O_3) doped with titanium. The Ti:Sapph is pumped with a diode-pumped solid-state laser which lases at 1064 nm and is doubled to the Ti:Sapph pump frequency of 532 nm[6]. The system provides >1 W of light at our desired wavelength with a linewidth of < 100 kHz. The wavelength is highly tunable, which allows other possible future applications such as measuring the $^3P_1$ transition's magic wavelength.

The 399 nm laser wavelength is set near the transition frequency of 751.5260 THz by fiber coupling an undoubled pick off beam to a wavemeter. We use the system's etalon lock and ECDL lock, and have found that using the reference cavity for linewidth narrowing was unnecessary (and caused extra problems). A triangle wave voltage is applied to the piezo controlling the mirror in the laser's reference cavity, sweeping over the frequency with a response of 6 GHz/V. For MTS, a 10 mW beam is split in two to form a pump and probe beam, both sent counterpropagating through an Yb optogalvanic hollow cathode lamp (HCL)[7], with the probe directed into a photodiode.

A HCL is a glass tube that contains a cathode with Yb on one end, an anode on the other, and a buffer gas in the middle. A large voltage is applied across the anode and cathode, causing the buffer gas to ionize and be accelerated into the cathode, sputtering off Yb atoms. This high voltage is run across a 100 kΩ - 25 W resistor, then through the HCL. 15 mA is the maximum allowed current through our HCL, but we typically keep it at 2.5 mA (300 V) to maximize the signal without using excess Yb.

The probe beam is sent into a photodiode[8], amplified[9], and mixed[10] with the RF signal. The mixed signal is sent through a low pass filters[11]. This all produces an error signal similar to that of Figure 3.5. See Figure 3.6 for a schematic of the optical and electrical set up.

[6]Lighthouse Photonics, Sprout-G

[7]Hamamatsu, exact model no longer available. Other companies that sell a similar model are Analytical West, Spectrolamps and Photron.

[8]Thorlabs, PDA36A

[9]Mini Circuits, ZFL-500LN-BNC+

[10]Mini Circuits, ZFM-3+

[11]Thorlabs, EF502

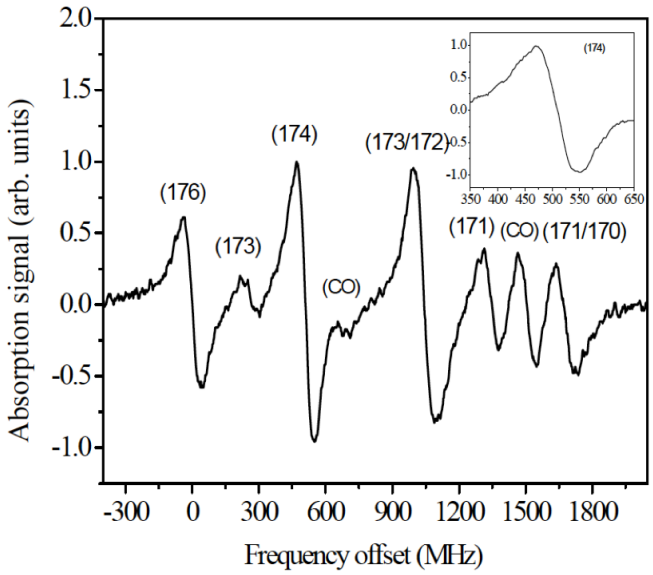

Figure 3.5: Example of a modulation transfer spectroscopy signal for the $^1P_1$ transition of Yb. [WYJ11] CO refers to a crossover resonance.

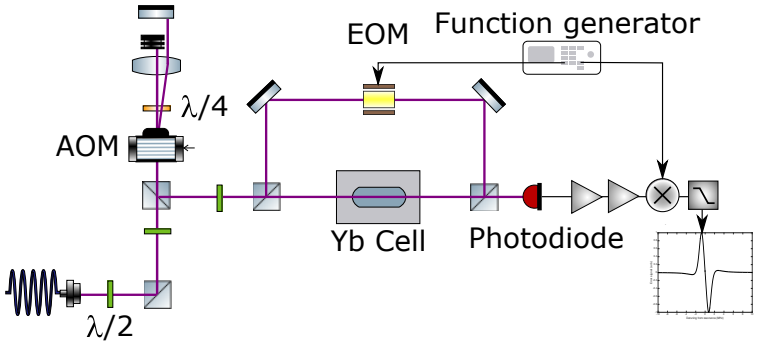

Figure 3.6: 399 nm modulation transfer spectroscopy set up. The photodiode signal is sent through two amplifiers, a mixer, and a low pass filter to produce the error signal. Note that the initial PBS after the fiber is used as a pick off to send 399 nm light into a test setup for an injection locked based 399 nm laser system.

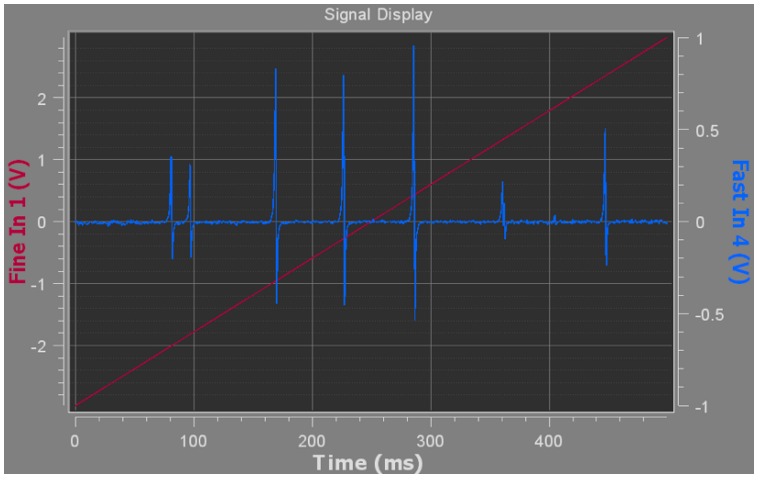

Figure 3.7: Example of our modulation transfer spectroscopy signal for the $^3P_1$ transition of Yb. "Fine In 1" in red is the voltage applied to the cavity piezo which controls the laser frequency. "Fast in 4" is the modulation transfer signal.

556 nm Laser Our CW 556 nm light comes from a tunable frequency-doubled diode laser[12]. The diode is amplified with a high power semiconductor and doubled with a crystal. The system provides >800 mW of light at our desired wavelength with a linewidth of < 500 kHz.

The 556 nm transition is much weaker than the 399 nm one, leading to a smaller MTS signal. This can be countered by using a longer Yb cell, allowing for higher absorption by the beam through the longer beam path. For the 556 nm lock, we used a larger home-built cell instead of a HCL. Yb metal is held in a vacuum pumped nipple, surrounded by heating wire keeping the chamber at 450°C with 3 A of current (70 V). The error signal for all of the isotopes is in Figure 3.7.

532 nm Laser A 532 nm laser is used as a stable reference laser for our optical cavity length. This wavelength was chosen because it is close enough to 556 nm to be included in the cavity mirror bandwidth, while far enough for separation from the 556 nm using a off-

[12]Toptica, TA-SHG Pro system

the-shelf filter. Additionally, 532 nm is a common wavelength, and we were able to purchase a 50 mW Coherent Compass 215M-50 laser head from eBay. Much of our knowledge about the inner workings of this laser came from Sam's Lasers FAQ [Com].

An iodine cell is used as a reference for this laser due to its rich spectra around this wavelength [SR05]. Because the exact frequency of this laser wasn't necessary (only frequency stability), we lock to whichever iodine line is nearest to the laser output without the need for large frequency tuning. We adjust the current and temperature of the laser to bring it near an iodine line while quickly scanning a double-passed AOM. We then use MTS with feedback to the AOM to lock the laser to this line.

3.2.2 Vacuum System

Ultra high vacuum (UHV) is necessary in order to keep background particles from knocking trapped particles out of the MOT and optical lattice. The vacuum pressure is directly correlated with the MOT lifetime. A decrease in vacuum pressure therefore increases the amount of time we can load before atoms begin to decay out of the MOT, which combined with a constant loading rate allows for a larger number of atoms to be captured.

Vacuum Components Our vacuum system consists of an Yb oven, a Zeeman Slower nipple, a MOT chamber, and a variety of gates, pumps and readouts. There are multiple types of flanges used to connect vacuum parts, including the most common KF (Klein Flansche - translation "small flange") and CF (Conflat). 2.75" CF flanges are used in our experiment based on the higher baking temperatures and lower vacuum pressures achievable. These flanges have a knife edge that cuts into a (typically copper) metal gasket[13] to create a vacuum seal. Out of the most common materials available for viewports, Kodial, Quartz and Sapphire, we chose to use Quartz[14] due to it having the lowest absorption at 399 nm and 556 nm. We AR coated the 2.75" viewports surrounding the MOT chamber to further minimize

[13]Lesker Company, GA-0275

[14]Lesker Company, VPZL-275DU

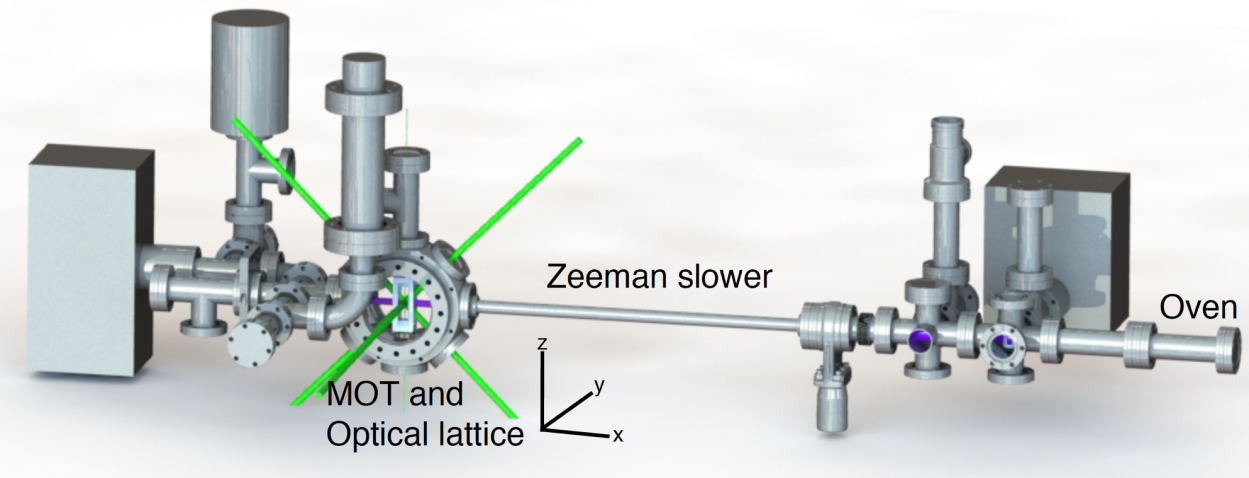

Figure 3.8: 3D Solidworks model of our vacuum chamber.

reflections.

From $+x$ to $-x$ in Figure 3.8, a Solidworks model of our vacuum system, we start with the oven nipple[15] described in 3.1.2, followed by a buffer nipple to decrease temperature conductance from the hot oven to the rest of the vacuum system. Next, we have a 6-way cross[16] that branches off into an ion pump, rotary feedthrough[17], a viewport, and the rest of the system (with the remaining two ports attached to blanks).

The rotary feedthrough attached to a custom shutter, see Figure 3.9, is used to block the Yb beam when not in use in order to decrease cold Yb build up on vacuum parts and viewports. The rotary is controlled via a stepper motor (attached to the feedthrough), which is in turn driven by a microstepping motor driver[18]. This is set up to be rotated via TTL inputs if necessary, but it is typically turned manually at the beginning and end of each day.

Next down the beam line is an identical 6-way cross with three viewports, and one output to a turbomolecular pump. This optical access is used as an optional transverse narrowing of

[15]Lesker Company, FN-0275

[16]Lesker Company, C6-0275

[17]Accu-Glass, 102110

[18]Circuit Specialist, QJ-215

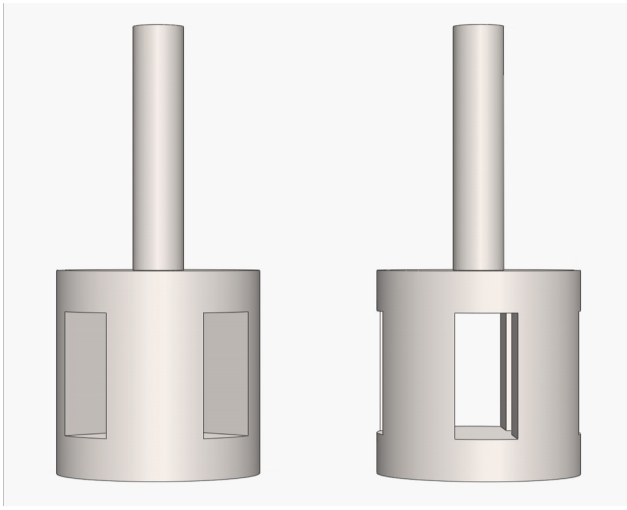

Figure 3.9: Custom shutter designed in Solidworks that was attached to the vacuum chamber via a rotary feedthrough. This could be manually or electronically rotated to turn the atom beam off (left) and on (right).

the atomic beam in the vertical direction, and as a monitoring port of the beam divergence in the horizontal direction. This right portion of the vacuum system is connected to the left portion via hydro formed bellows[19]. The bellows are used for optimization of the alignment of the beam down the vacuum system. After the bellows is a gate valve[20], which allows us, if needed, to separately open the two halves of the vacuum system without re-pressurizing the other. Fun fact: the rubber parts of the gate valve do not like to be soaked in acetone.

The left side of the system contains most of the science. First after the gate valve is the Zeeman slower nipple, which is a custom Lesker 20"-long 1.33"-CF nipple. Following the slower is the 6" spherical octagon chamber[21], which allows optical access for the MOT beams, and enough room for an in-vacuum optical cavity. This chamber has two 6" viewports[22],

[19]Lesker Company, MH-CF-C03

[20]Duniway, GVMM-150-CF

[21]Kimball Physics, 53-180200

[22]Lesker Company, VPZL-600DUC2

5 2.75" viewports and one tee[23]. The top of the tee has a viewport, and the side has a electronic feedthrough[24] used for the optical cavity piezos. Coming out of the left side of the MOT is a variety of tees and elbows that branch off to a titanium sublimation pump, ion pump, and ion gauge. The final tee has a viewport on the bottom which looks up onto an in-vacuum 45°-set mirror, which allows the 399 nm beam to be sent down the length of the slower.

Pumps A variety of pumps are needed to get the system at or below 10^{-9} Torr. A roughing pump is a first stage pump, used between room pressure and 10^{-3} Torr. The turbomolecular pump (turbo pump) is used to bridge the gap between the roughing pump and the sensitive ion pumps, which could break above 10^{-6} Torr. Once the pressure reaches 10^{-6}, an angle valve [25] is used to close off the roughing and turbo pump before turning on the ion pumps, which continuously run during experimental operation. The final titanium sublimation pump (ti-sub) is turned on once or twice as the final step and only decreases the pressure by a few 10^{-10} Torr. Following is a list of each pump part, and a brief description of operation.

- Roughing Pump: The Agilent IDP-3 Dry Scroll Vacuum Pump can reach 10^{-3} Torr. It consists of two archimedean spirals, one rotating on top of the other. As the spiral rotates, it lets air in between the two spirals, then seals off the opening and compresses the air, pushing it through the spirals out of the system.

- Turbomolecular Pump: The Agilent Turbo-V 81-M Vacuum Pump reaches the next level of vacuum, approximately 10^{-6} Torr. This pump is made up of fast rotating angled blades which hit molecules and give them momentum in the direction of the exhaust.

- Ion Pump: The Duniway 30l/s Ion Pump and the Agilent VacIon Starcell Plus 40 allow

[23]Lesker Company, T-0275

[24]Lesker Company, EFT0143058

[25]Agilent, 9515027

the system to get down to 10^{-9} Torr. Ion pumps accelerate electrons with electric and magnetic fields that bombard particles creating ions. These ions then get accelerated by a kV voltage towards a grounded cathode plate covered in Titanium. The fast heavy ions sputter titanium that coats the nearby surfaces. Titanium is highly reactive with typical air molecules which then stick to the surfaces lowering the gas pressure of the system.

- Titanium Sublimation Pump: The Agilent Titanium Sublimation Cartridge is the last stage of the pumping process and can push the vacuum down to levels of 10^{-10} Torr. It works by sputtering off titanium, coating the local surfaces, and trapping gas particles on the reactive titanium.

Pressure Before and after the Zeeman slower, the atoms are directed through differential pumping tubes into the 3D MOT region. This allows for the 3D MOT region to maintain a pressure of $< 10^{-9}$ torr when the Zeeman slower region is at a higher value of $\approx 10^{-7}$ torr, and the chamber right after the oven as high as $\approx 10^{-5}$ torr. The pressure ratio between two chambers connected by a tube can be found using $P_r = \frac{S_r}{C} + 1$, where $S_r = 30$ L/s is the pumping rate on the lower pressure side and C is the molecular conductance. The conductance of molecules through a tube is $C = \frac{\pi d_d^3}{12 L_d}\sqrt{\frac{k_B T}{2\pi m}}$, where d_d is the diameter of the tube and L_d is the length. For air at 20°C and a differential pumping tube with $d_d = 0.5$ cm and $L_d = 7$ cm, the pressure ratio is $P_r = 340$. The Zeeman slower nipple also acts as a long differential pumping tube with $d_d = 2$ cm and $L_d = 30$ cm, leading to an additional pressure ratio of $P_r = 12$. The two differential pumping tubes and the Zeeman slower nipple combine to a pressure ratio between the first chamber after the oven and the 3D MOT chamber of 10^6, ensuring a low enough vacuum pressure to maintain long coherence times (>1 s) in our optical cavity.

Obtaining UHV A meticulous procedure for all of the vacuum parts is followed to ensure that UHV levels were reached. A lot of these procedures are lore, but since it would be

extremely time consuming to try different cleaning techniques, each followed by vacuum assembly and multiple day bake-out, we follow them religiously.

All parts that come from vacuum manufacturing companies are soaked in ultrasonic baths of acetone and methanol for 30 minutes each. The acetone cleans the surfaces of the parts but leaves a residue. A methanol bath is then used to clean off the residue left by the acetone. Any parts that are made by the machine shop are first washed with Alconox, a de-greaser. After 30 minutes of the ultrasonic bath filled with Alconox and water, the parts go through two 30 minute ultrasonic baths with clean water to get rid of the Alconox residue, then go through the acetone methanol treatment.

In order to get rid of particles stuck to the wall of the chamber and light elements trapped within the stainless steel itself, the entire chamber is wrapped in heating tape and baked. In order to ensure uniform heating, a tight layer of aluminum foil, which has a thermal conductance 17 times higher than steel [The], is applied over the heating tape. Loosely fit foil over the tight layer provides insulating air pockets. If the chamber is not uniformly baked, temperature gradients can cause leaks or can cause the glass windows to break. The goal temperature of 175°C must be reached by slowly ramping up the temperature so a gradient is not formed and the glass does not break. The temperature is brought up from room temperature at approximately 1°C per minute. The final baking temperature of 175°C is limited by the maximum allowed temperature for the windows of 200°C.

Before baking, the roughing pump and turbo pump are run for about an hour, resulting in a vacuum of $5 \cdot 10^{-5}$ Torr. Once the system reaches its final temperature, it is baked for a couple of days. After the system is cooled back down (again at approximately 1°C per minute), the ion pumps and the titanium sublimation pump are used to decrease the pressure further, to obtain a final vacuum pressure of $\sim 1 \cdot 10^{-9}$ Torr. We expected to be able to obtain vacuum pressure closer to $1 \cdot 10^{-10}$ Torr, and suspect the limitation comes from a small leak in the tee that houses the 45^o angle mirror due to the difficulty in tightening the double-flange, and due to the stresses incurred as a mounting point for the vacuum chamber.

3.2.3 Zeeman Slower

A beam of particles exiting a tube have a velocity distribution

$$f(v) = \frac{v_z^3}{2\bar{v}^4} e^{-v_z^2/(2\bar{v}^2)}, \tag{3.6}$$

where $\bar{v} = \sqrt{k_B T/m}$. The MOT has a capture velocity of 2-10 m/s [KHT99] depending on the broadening (see Section 3.2.4), while the atoms coming out of the oven at 450°C have a most probable velocity of $v_p = \sqrt{\frac{3kT}{m}} = 322$ m/s.

Adding a slowing stage before the atoms reach the MOT can greatly increase the number of atoms below the capture velocity. A simple slowing design consists of aligning a counterpropagating resonant laser down the atomic beam path. An atom absorbs a photon with momentum in the opposite direction, then spontaneously emits it isotropically. After many absorptions, on average, the atom loses momentum. However, since the atoms start at $v_p = 322$ m/s and end at near zero velocity, they experience a massive Doppler shift,

$$\frac{\Delta\omega_D}{\omega} = \sqrt{\frac{1 + v_p/c}{1 - v_p/c}} - 1, \tag{3.7}$$

by as much as $\Delta\omega_D = 2\pi \cdot 800$ MHz from the counterpropagating laser. Since the linewidth of the 399 nm transition for Yb is $2\pi \cdot 28.9$ MHz, the laser can only address a small portion of the atoms at any given time. The laser can be kept on resonance either by changing the frequency of the laser as the atoms slow down, or by changing the resonance of the atoms directly. The Zeeman slower uses a magnetic field to directly change the resonance of the atomic transitions.

We use the 399 nm cycling transition of $m_F = 0 \to m_{F'} = -1$ for ^{174}Yb (we equivalently could have used $m_F = 0 \to m_{F'} = 1$) and $m_F = 1/2 \to m_{F'} = 3/2$ (or equivalently $m_F = -1/2 \to m_{F'} = -3/2$) for ^{171}Yb. Table 3.1 can be used to determine $\Delta\mu$ for these two transitions. Conveniently, both transitions yield $\Delta\mu \approx \mu_B$ because of the difference in $m_{F'}$ sublevels, and we don't have to change the magnetic field parameters when switching isotopes.

The design of the Zeeman slower amounts to choosing the magnetic field profile, Eq. 2.8, the atoms experience as they travel down its length, repeated here for reference,

$$B(z) = B_{\text{bias}} + B_0\sqrt{1 - \frac{2a_{\max}z}{v_0^2}}.$$

The design allows us to get estimates for B_{bias}, B_0, the length of the slower, and the detuning. In reality, we set up our experiment with these parameters, then scan each one to determine the value which maximizes the trapped atoms in the MOT.

The span of the magnetic field, B_0, is determined by the maximum desired acceptance speed of Yb from the oven, v_m. Compromising high acceptance with ease of magnetic coil construction, we chose $B_0 \approx -600$ G, which has an acceptance velocity of $v_m = 350$ m/s, accepting around half of the atoms that come out of the oven. The value of B_{bias} is set by the detuning of the beam from the atomic transition. Because the slower beam necessarily travels directly through our MOT region, a far detuned beam is necessary to keep from heating and pushing the MOT atoms. We chose a detuning of $\omega - \omega_0 = -2\pi \cdot 700$ MHz, which only displaces the MOT 3 mm and yields a heating rate which is less than the self-heating rate of the MOT [Fre15]. This leads to $B_{bias} \approx 500$ G, yielding a magnetic field range of -100 G to 500 G, which we determined to be manufacturable.

The length of the slower necessary for the atoms to slow to a final speed of v_f is $L_s = \frac{v_0^2 - v_f^2}{2a_{max}}$ (rearranged from Eq. 2.7). Choosing v_f requires balancing the increase in atoms that are at or below the MOT capture velocity as v_f is decreased, and the increase in atoms from the large divergence out of the slower when v_f is increased. We chose a final velocity of $v_f = 10$ m/s, which would allow for a length as small as $L_s = 6$ cm. It is typical to decelerate the atoms at a rate slower than the maximum deceleration in order decrease the sensitivity to small imperfections in the magnetic field profile and decrease the amount of laser power needed. We chose to go with the maximum length possible given physical constraints on our optics table, $L_s = 35$ cm, which gives us flexibility with beam power, and makes the construction of the complicated magnetic field profile easier.

The coils needed to make the desired magnetic field were simulated in MATLAB; their

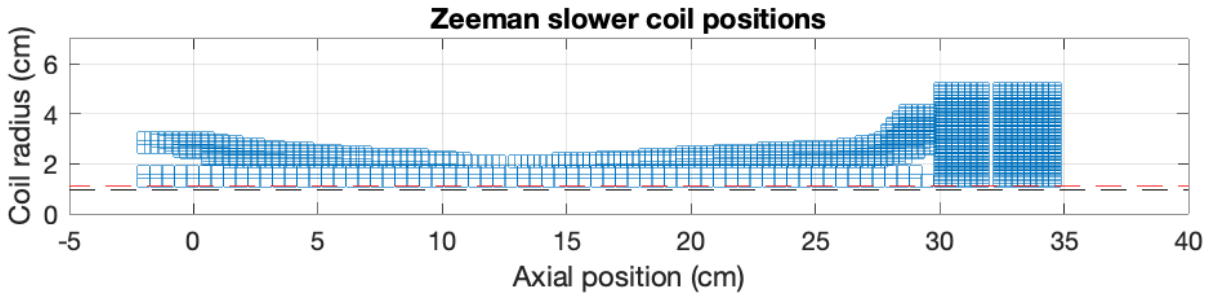

Figure 3.10: Zeeman slower coil layout. Five distinct coils were used for maximum control of the magnetic field.

arrangement is in Figure 3.10. The coils consist of five sections of wrapping that are independently current controlled. Details about the wiring can be found in Table 3.2. The first layer is a solenoid made from hollow square kapton-coated wire[26] allowing for water cooling through the middle of the coils. On top of that there are two sets of coils made from flat solid rectangular kapton-coated wire[27], one with a negative taper and one with a positive taper. On the end of the slower coils on the side leading into the MOT, there are be two larger sets of coils. The first coil enables the magnetic field to reach its peak value, and the second coil sharply turns off the magnetic field so that the atoms had a clean break out of the system at v_f, and the magnetic field leakage into the 3D MOT system was limited. The contribution of each coil to the total magnetic field can be seen in 3.11.

Between the winding layers there is thermal epoxy[28] to aid in thermal conductivity so that the system can be efficiently cooled. Some photos of the construction process are shown in Figure 3.12. The hollow inner layer of coils has water running through them for cooling. The large peak and turn-off coils are flanked by metal disks (similar to the plastic one seen in Figure 3.12), which are also water cooled. These measures allowed for continuous running

[26]We borrowed this from the Hudson lab and I don't know the part number.

[27]Swiger Coil Systems, 033X0.098R

[28]Duralco, 4525-IP

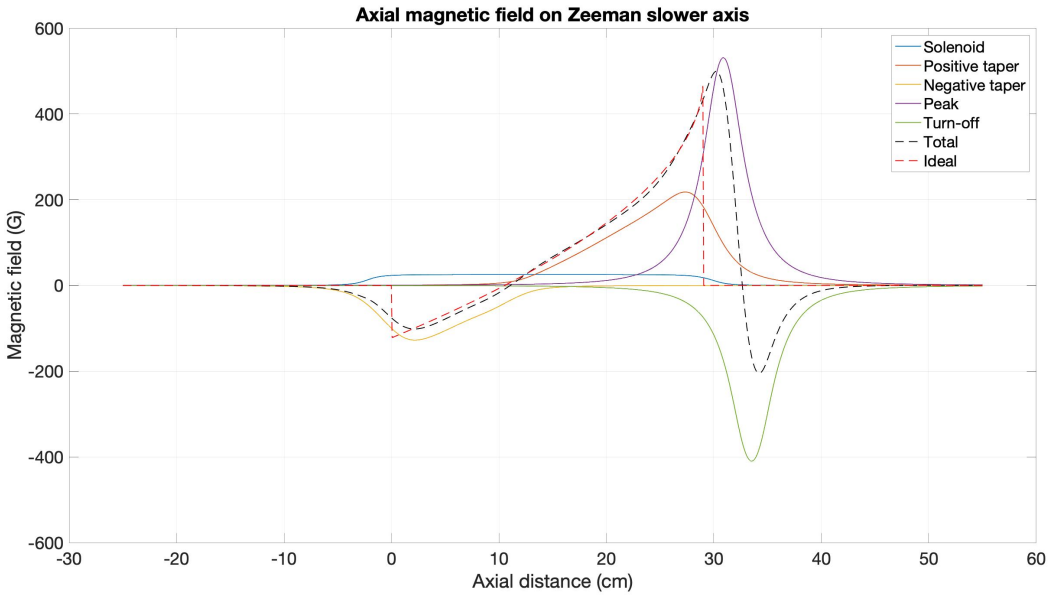

Figure 3.11: Magnetic field contribution from each of the five coils used to make the appropriate total field for the Zeeman slower.

of the coils with no over-heating.

The 399 nm laser is locked -270 MHz detuned to the transition by locking a first order mode of an AOM to an Yb reference cell. It is then further red detuned via a double pass AOM system[29] at drive frequency 260 MHz which also allows for small adjustments in the detuning for optimization. This drive frequency is created by a voltage controlled oscillator (VCO), with calibration shown in Figure 3.13. Choosing the correct order out of the AOM gives us a total detuning of -790 MHz. The beam is then blown up to about 0.5 cm radius, reflected off of an in-vacuum 45° mirror, and sent through the length of our chamber. We use a camera focused on the differential pumping tube near our oven to roughly align the laser, but ultimately make small aligning adjustments by watching the number of atoms in the MOT. The complete optical setup for the 399 nm laser is in Figure 3.14.

The slower was tested with the oven at 400°C. The power in the slower beam laser was

[29]Isomet, 1250C-829A

Figure 3.12: The long nipple was covered in tin foil and heating tape for vacuum baking purposes. A thermocouple was placed inside to monitor temperature. The magnetic wire was wound on a lathe.

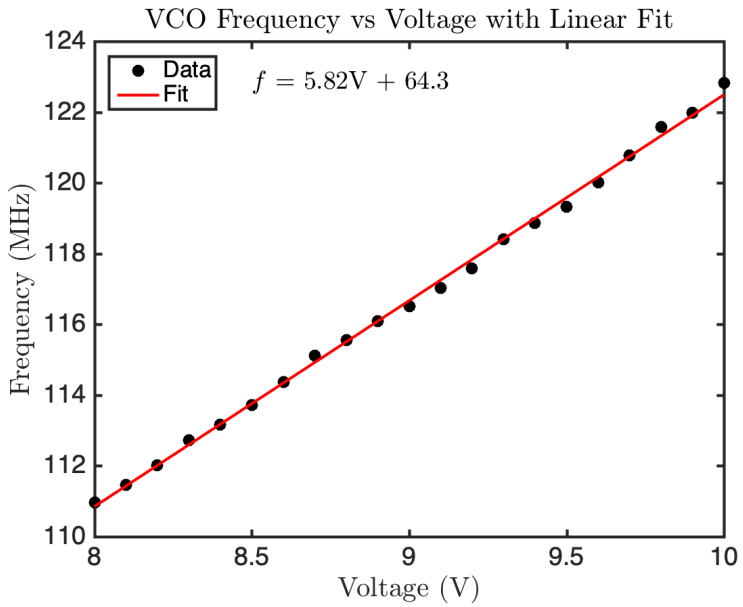

Figure 3.13: Voltage controller oscillator (VCO) calibration for voltage to drive frequency. This VCO controls the double passed AOM for our MOT laser. To obtain the MOT detuning, subtract two times this drive frequency from -270 MHz.

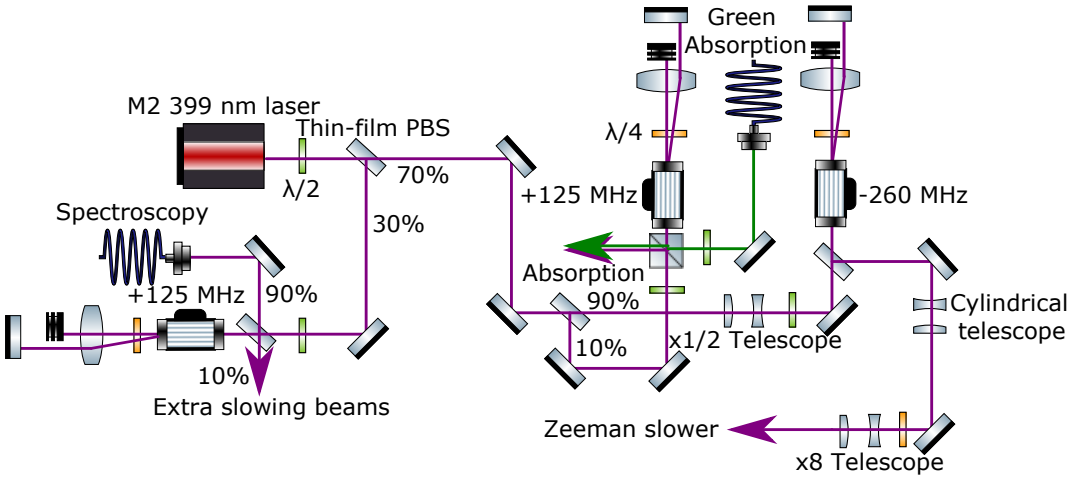

Figure 3.14: Complete optical setup for the 399 nm laser. The thin film polarizers (Eksma Optics, number 420-1253E) were used due to the high laser power. The percentages represent the laser power in each direction with respect to the incoming beam.

	Size of Wire (mm)	Current (A)
Solenoid	4 x 4	9.5
Positive Taper	0.8 x 2.5	5.2
Negative Taper	0.8 x 2.5	−5.2
Peak	0.8 x 2.5	6
Turn-off	0.8 x 2.5	−4.1

Table 3.2: Details about the wires used to create the slowing magnetic field.

92 mW, and is subsequently kept at ≈100 mW. The atom number was measured using an absorption beam that was $\theta_a = 3°$ off from perpendicular. The absorption beam detuning was swept and mapped onto the $-x$ direction velocity of the atoms using the Doppler shift $\Delta\omega_D = k_3 v \sin\theta_a$, where k_3 is the wavenumber for the 556 nm laser. With the slower off, the atom distribution peaked close to the expected most probable velocity of $v_p \approx 300$ m/s. With the slower on, a large population of the atoms was slowed to a center velocity of 8 m/s.

3.2.4 Magneto-Optical Trap

The Zeeman slower slows the high velocity Yb from the oven to a few meters per second. The magneto-optical trap (MOT) then cools these atoms and spatially traps them at the center of our vacuum chamber. It is important for the atoms to be much colder than our optical cavity lattice depth ($< 100\ \mu K$) to ensure efficient loading. The MOT can nominally cool the atoms down to their Doppler cooling limit, $T_D = \frac{1}{k_B}\frac{\hbar\Gamma}{2} = 4\ \mu K$ for the 556 nm transition, but we typically observe temperatures of 10–20 μK.

The optical set up uses three pairs of counterpropagating beams along three perpendicular axes. The beams are separated using PBSs, sent through quarter-wave plates to obtain circular polarization, and magnified by a factor of four with a telescope. A larger beam size increases the capture region, but decreases the maximum intensity per beam (we use the maximum available laser power typically ¿100 mW). Our setup also consists of an in-

vacuum optical cavity which has cut outs for the beams, limiting the beam size, leading to a final beam size of $1/e^2$ intensity radius 1.5 cm. We initially struggled to get large Gaussian beams without rings. We were using Thorlabs PM-405-XP fibers for all of the beams in our lab, and found that increasing the center wavelength of the fibers, switching to Thorlabs PM-488, greatly reduced the contrast of the rings. Note that the easier solution of increasing the NA of the collimation lens after the fiber was not enough with the 405 nm centered fiber. Our choice of specific MOT parameters closely follows that of Dörscher's thesis [D13], with small adjustments made to optimize our system. Each diagonal beam receives 21% of the total 100 mW of power, and each axial beam received 8%. A diagram of the optical setup can be seen in Figure 3.16. A diagram of the complete 556 nm optical setup that produces the MOT beams can be seen in Figure , as well as the beams used for the optical cavity talked about in the next section.

The narrow intercombination transition used for the MOT allows for the low Doppler cooling temperature limit, but also results in a very low capture velocity. If we were to release the atoms from the Zeeman slower at the capture velocity according to the natural linewidth of the transition, 2 m/s, the beam expansion would greatly limit the flux into the MOT capture region. To increase the capture range and therefore increase the flux into the MOT, we modulate the beam frequency at 300 kHz, slightly larger than the linewidth. The modulation is performed by modulating the input to the VCO controlling the MOT detuning. As the atoms slow down, they are resonant with sidebands closer and closer to their transition frequency. The beam is red-detuned $\approx$3.7 MHz from the transition, and symmetrically broadened to a width of $\approx$3 MHz to ensure there was very little power in any blue sidebands which heats the atoms.

The quadrupole magnetic field is made using a pair of coils in the anti-Helmholtz configuration. Two plastic spools are designed and machined to screw directly onto the vacuum chamber. We use hollow square wire to allow for the possibility of having large magnetic fields in the future that would require water cooling. The wire is wrapped with 8 turns per layer and 7 layers using a lathe, providing a magnetic field gradient at the atoms of roughly

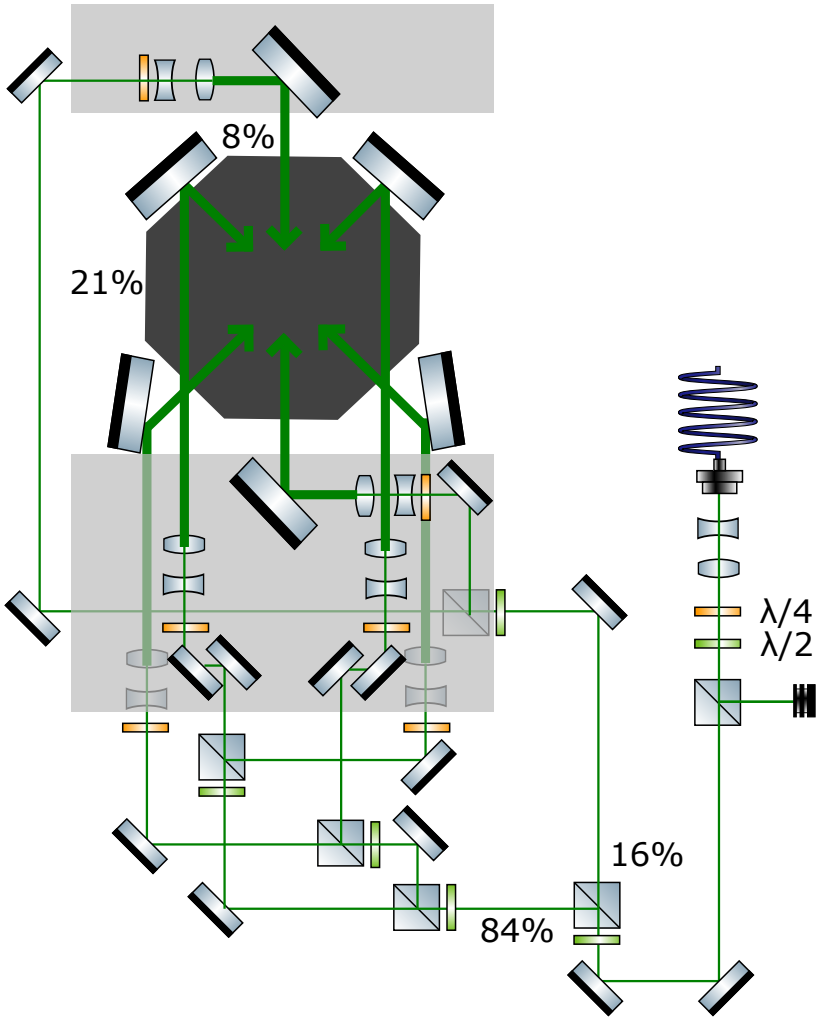

Figure 3.15: The beam used for the MOT is typically 100 mW at the fiber exit. It then passes through a telescope, and a filtering PBS. The beam is subsequently split up into the 6 beams needed for the MOT. Angles and sizes not to scale. The percentages shown are out of the 100 mW; each of the horizontal beams has 8% of the total power and each of the diagonal beams has 21% of the total power.

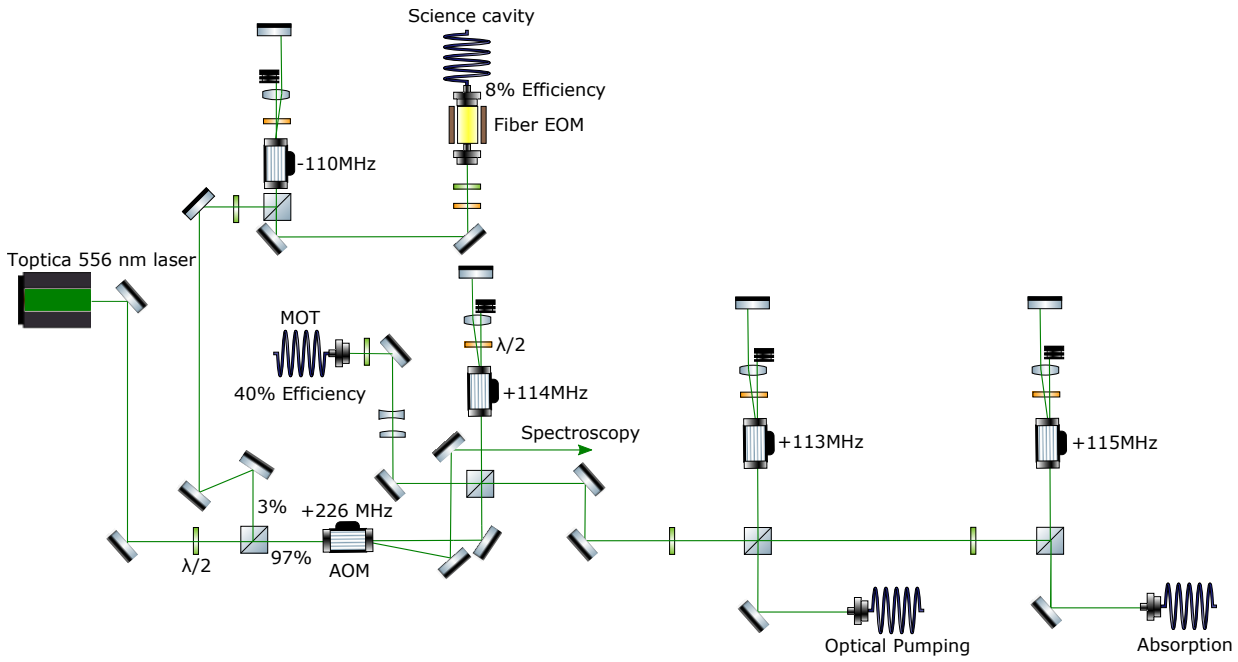

Figure 3.16: Complete optical setup for the 556 nm laser. The percentages represent the laser power in each direction with respect to the incoming beam.

0.4 Gauss/cm/A. A MATLAB simulation of the coil setup was performed to check the linearity of the magnetic field gradient at the center of the MOT. The gradient was determined to be a constant within ±1% in the ±1 cm region around the center of the chamber.

Atoms are typically cooled to ~ 20 μK at a loading rate of 10^7 atoms/s for Yb^{174}.

3.3 Trapping

3.3.1 Optical Cavity

Atoms trapped in an optical lattice are the crux of our experimental apparatus. The coupling between the atoms and the lattice allows us to extract information about the atoms by reading out information from the light. Using an optical cavity to form this lattice has many benefits compared to other methods like a retro-reflected beam. The light bounces between the cavity mirrors many times before exiting. Because of this and the boundary conditions, the amplitude of the standing wave is greatly amplified and decreases our laser power requirements. In addition, the cavity restricts the geometric spatial mode and phase relation of the beam, decreasing issues with shot-to-shot fluctuations in the lattice position and amplitude.

We have a variety of requirements and limitations to keep in mind when designing the cavity. Spatially, the cavity spacer has to fit within our octagonal vacuum chamber, and be mounted via brackets[30] to one of the windows. Because we directly load the MOT atoms into the optical lattice, the spacer needs to allow optical access for all six 1.5 cm-diameter MOT beams. Since we are located in California, the mounting system should also be earthquake proof.

Fluctuations in the cavity length on the order of one wavelength of the light cause large fluctuations in the transmitted light, adding noise to our signal. We specifically want to avoid length fluctuations with frequencies around our expected signals: 1 kHz for gravita-

[30]Kimball Physics, MCF275GrvGrbC02

tional Bloch oscillations, $<$ 100 Hz for dark matter and 500 kHz-1 MHz for temperature measurements. Slow temperature fluctuations can be managed by using piezo actuators to correct for length changes, however their limited range means we still needed to consider thermally insensitive materials. Finally, we have to consider machining capabilities and cost since we are using a glass spacer.

The specifications for the cavity mirrors are important for considering our expected signal to noise ratio. We also consider ease of alignment and cost when choosing radius of curvature and transmission requirements for the mirrors. First, I describe spacer design and mounting system, and walk through some vibrational analysis I performed on the set up. Next, I discuss our choice of mirror cavities, which is crucial in obtaining the best atom-cavity coupling for our science goals.

Spacer And Mount Design The cavity spacer we designed was based a cavity spacer in Justin Bohnet's PhD thesis [Boh14] in which he explores superradiant lasing and spin squeezing.

The geometry of the cavity spacer is constrained by the length of the cavity, the space available inside of the 3D MOT chamber, and the optical access needed for the 3D MOT beams. The length of the cavity was chosen to be as large as possible given the chamber constraints, with large cut outs for 3D MOT beam access while not sacrificing rigidity. The length of the cavity is therefore $L_c = 3.6$cm. On the top and bottom of the spacer there are holes for cavity laser access. On the inside of the spacer, there are flattened level surfaces to which piezos and cavity mirrors are epoxied. See Figure 3.17, and see Appendix 6.1 for a machining drawing for technical details.

To limit the vertical "squishing" vibrational modes, which change the length of the cavity, the spacer is designed to only have contact with the cavity mount legs near the vertical center, and to be as symmetric as possible. The material used is Zerodur, a type of glass with extremely low thermal expansion, orders of magnitude less than steel.

The squishing modes were estimated before construction by using a simple model of the

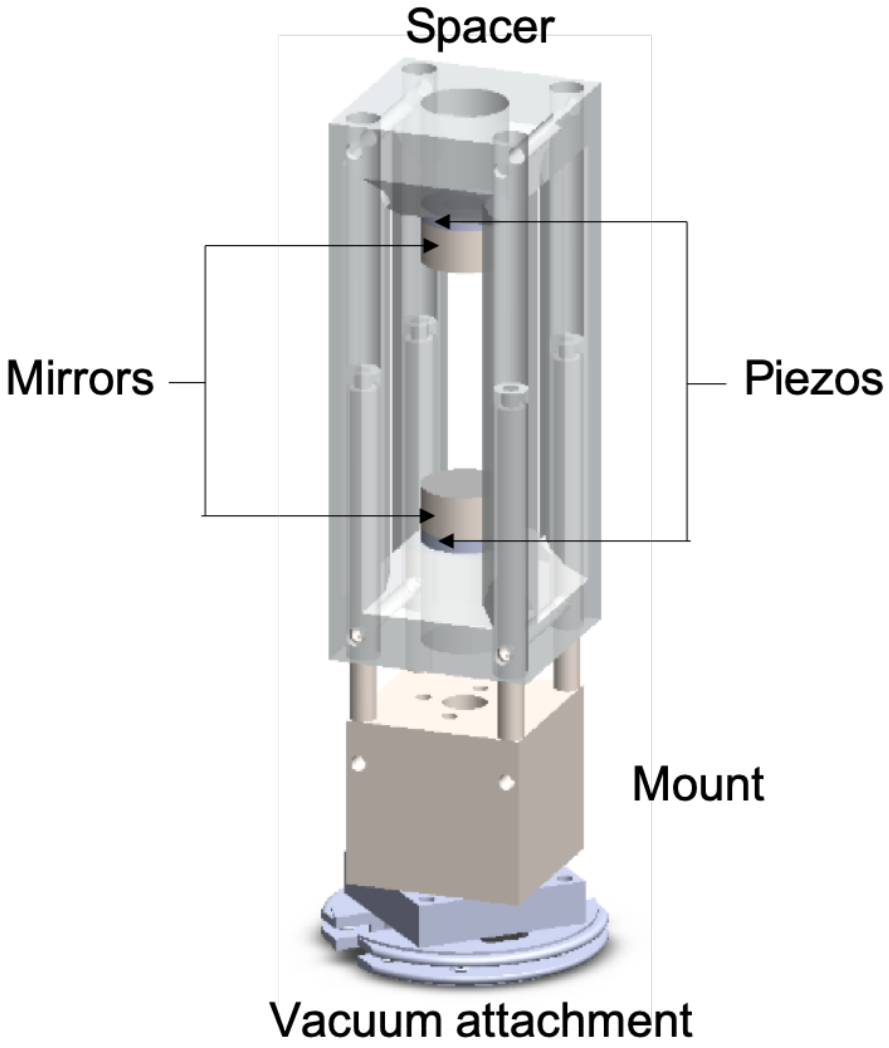

Figure 3.17: Optical cavity and mount. The mirror spacer is made of Zerodur, and has cut outs to allow optical access for the MOT beams. There are two highly reflective mirrors, each on top of a piezo for cavity length control. The stainless steel base connects the spacer to the vacuum chamber.

system to ensure that the resonance were not in one of the design-excluded regions. The spring constant of a physical system is $k_S = S_S Y / L_S$, where S_S is the surface area of the spring, Y is the material's Young's Modulus and L_S is the length of the spring. The Zerodur piece, with $Y = 90.3$ GPa [Zer], was modeled as four rectangular springs in parallel. With the projected mass I estimated the resonant frequency as $\frac{1}{2\pi}\sqrt{\frac{k_S}{m}} = 10$ kHz. Using the manufacturer's spring constant for the piezos and material estimates for the mirrors, the expected resonances are 115 kHz and 70 kHz, well out of our problematic ranges.

We are also concerned about total vertical acceleration of the spacers, which by symmetry would mimic an atomic acceleration in the opposite direction. For this I calculated the transfer function system, in other words how well a vibration of the table transfers to a vibration of the cavity. I then used the expected acceleration of the optics table to estimate the total acceleration the cavity will feel within each frequency range of interest. A mount rigidly attached to the vacuum chamber, which is in turn rigidly attached to the table, would have a transfer function of one for all frequencies. I compared this to including four rubber balls for damping in between the vacuum chamber and the cavity mount. The results of this analysis are that a rigidly mounted cavity is better than adding an extra layer of passive damping, but I would like to include my calculations as a reference for how to analyze mechanical systems in the lab.

I was interested in comparing the transfer function of a four-ball passive damping system to a rigidly mounted system. The differential equation for a driven system is simply

$$m\ddot{x} + b\dot{x} + k_S x = F_d \cos(\omega t), \tag{3.8}$$

where m is the mass, b is the damping coefficient, x is the displacement of the mass, F_d is the driving force, and ω is the driving frequency. The solution to this equation is

$$x(t) = \frac{F_d/m}{\sqrt{(k_S/m - \omega^2)^2 + \omega^2 b^2/m^2}} \cos(\omega t). \tag{3.9}$$

I am interested in the acceleration response, so the second derivative of the solution is

$$\ddot{x}(t) = \frac{-\omega^2 F_d/m}{\sqrt{(k_S/m - \omega^2)^2 + \omega^2 b^2/m^2}} \cos(\omega t). \tag{3.10}$$

$\frac{\omega^2}{k_S}F_d$ is the amplitude of the driving acceleration, so I can divide that out to obtain the transfer function:

$$\frac{k_S/m}{\sqrt{(k_S/m-\omega^2)^2+\omega^2 b^2/m^2}}. \tag{3.11}$$

The benefit of using a damping mechanism is clear when I look at driving frequencies much higher than the resonance of the system $\sqrt{k_S/m}$. When $sqrtk_S/m << \omega$, the function scales as ω^{-2}, sharply decreasing the acceleration transfer. It is also important to look at the maximum of the transfer function, which occurs at the critical driving frequency $\omega_c = \sqrt{k_S/m - b^2/(2m^2)}$, and has a transfer function greater than one. This should not fall on, for example, the resonance of the optical table.

I modeled the rubber balls as ideal springs, estimating the surface area to be the cross section of the sphere, and the length to be the diameter of the sphere, 1.5 mm. There are four balls in parallel, giving a spring constant of $k_S = 2.8 \cdot 10^4$ N/m. The damping equation for Viton, the rubber of choice for UHV applications, is found in [CVD]. The loss factor is $\frac{b}{b_c}$, where $b_c = 2\sqrt{k_S m}$ is the critical damping coefficient. After reviewing possible materials, I decided to use a loss factor of 0.1 for this calculation.. This gives an estimated damping coefficient of $b = 56$ kg/s.

I obtained the mass of the Zerodur cavity and steel cavity spacer in Solidworks, which together are approximately 0.2 kg. To lower the spring constant, I also included a cage mount for a large tungsten cylindrical tube which adds a mass of up to 2.6 kg to the system.

Finally I'd like to compare all of these response frequencies to the amplitude of the driving frequencies on a typical optical table. Our lab has optical tables[31] that include a passive damping mechanism. Because the table is heavy, the resonance of this damping is quite low, usually around 1 Hz. These background levels of the table were measured in Achim Peters' PhD thesis [Pet98], and can be seen in Figure 3.18.

Because the table already provides damping from the environment above 2 Hz, we only expect large improvements in the total acceleration if our additional passive system has a

[31] Newport,RS2000-48-12 tabletop with S-2000A-423.5 stabilizing legs

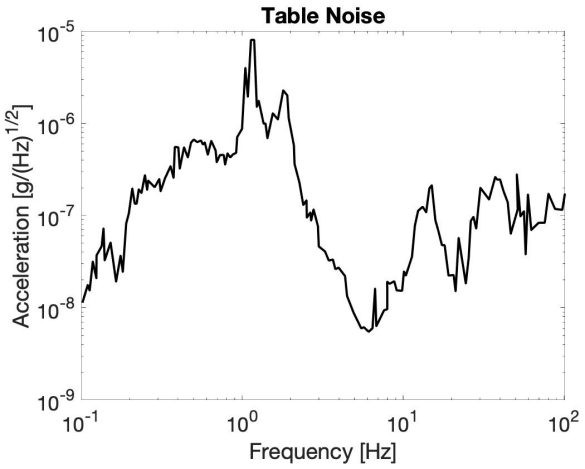

Figure 3.18: Noise profile of a floating Newport table.

resonance below 2 Hz. However, I found that the critical resonance with and without the extra tungsten weight would be 16 Hz and 50 Hz respectively. In order to get our system to have a resonance below 2 Hz, we would need an extra weight of 175 kg. This is not feasible with simple engineering for our system. One group [Boh14] added large support rods that connect their cavity to a heavy pendulum that hangs below their chamber, but they still observed low frequency vibrations on their system at 17 Hz.

Cavity Mirrors Specifications for the mirrors include the coating on two sides and the radius of curvature. The outside faces of the mirrors are AR coated to minimize spurious reflections. When choosing an intensity reflectivity R of the inner coating, we consider its effects on the linewidth of the cavity and the finesse. From the simulation (Section 2.2.3) I found that decreasing the linewidth increases SNR. The lower limit for our cavity linewidth is the Bloch frequency. This is countered by the manufacturing challenge of having both high reflectivity and efficient transmission while maintaining low loss. Loss can come from both absorption by the mirrors and scattering. Working with manufacturers, the lowest reasonable loss possible for a single wavelength mirror is 10 ppm. This means that we have a maximum reflectivity of $R = 0.99999$ ($\kappa = 2\pi \cdot 6$ kHz) with no transmission. Again working with manufacturers, we settled on $R = 0.999$ which allowed for transmission 100

Cavity Parameter	Expected Value	Measured Value
Length (L_c)	3.6 cm	3.63121(4) cm
Radius of Curvature (R_c)	70 cm	70.52 cm
Reflectivity (R)	.999	.9986
Linewidth (κ)	$2\pi \cdot 1.5$ MHz	$2\pi \cdot 1.8$ MHz
Finesse ($\mathcal{F}$)	3100	2293
Waist (w_ℓ)	140 μm	$\sim$

Table 3.3: Summary of cavity parameters (at time of manufacturing).

times greater than the expected loss. We could consider pushing this reflectivity higher in the future for a narrower cavity. This results in a nominal linewidth of $\kappa = 2\pi \cdot 1.5$ MHz and finesse of $\mathcal{F} = 3100$.

The larger radius of curvature increases the mode volume of the lattice allowing for a higher capture percentage of atoms from the MOT. We also took into consideration that a high radius of curvature increases the difficulty in aligning the cavity mirrors because of the increased angular precision necessary to keep the light from walking off the mirrors after many bounces. We decided on a radius of curvature of $R_c = 70$ cm. As the coating run is the expensive part of manufacturing (as opposed to the number of mirrors), we added $R_c = 20$ cm and $R_c = 125$ cm mirrors as options for the future. The intensity $1/e^2$ waist radius of the cavity mode is $w_\ell = 140$ μm. We can calculate the expected number of atoms loaded into the cavity by multiplying the lattice mode volume by the diameter of the MOT divided by the length of the cavity. For 10^7 atoms in the MOT with a loading time of 1 s and a density of 10^{11} cm^{-3}, we are able to load 10^6 atoms into the cavity.

Piezos Because the exact laser frequency is quite restricted by the atom resonance and desired detuning, it is convenient to be able to change the cavity length to match the laser resonance. Adding piezo-actuators in between the spacer and the cavity allow for scanning

the length of the cavity and therefore the frequency for fine-tuning. Minimally, we want a piezo that can scan one free spectral range. However, if we're trying to match modes of lasers with two different frequencies, being able to scan multiple FSRs can be very helpful. We decided to install Noliac NAC2123 piezos on both mirrors in case of accidentally shorting one during the bake-out. These piezos are ring shaped for optical access, and have a max free stroke of 3.3 μm, allowing us to scan about 3.3 μm/556 nm$\sim$ 5 FSR's with each piezo. We have found the flexibility of having two working piezos very useful - one for gross scanning, and one for locking feedback.

After failing at manually aligning the piezos and mirrors to a precision necessary to get a centered cavity mode, the piezos and mirrors were epoxied[32] to the spacer by the same company that machined the spacer.

Stabilizing The cavity length needs to be stabilized to well within the length of our laser wavelength, $\Delta L_c \ll \lambda_\ell$. We use the stabilized 532 nm laser as a reference to lock our cavity length via the Pound-Drever-Hall technique [DHK83]. An EOM generates sidebands at 24 MHz on the 532 nm laser, then the light is split by a PBS and sent into the science cavity. The phase change in the reflection from the cavity when near resonance can be used to create an error signal very similar to that of MTS 2.1.3, see Figure 3.19.

Testing The cavity was manufactured by Stable Laser Systems. After installing the cavity into the MOT vacuum chamber, and baking down to UHV, we tested the cavity to check the mirror specifications.

We found that the linewidth was limited by our ability to clean the mirrors, and that First Contact Cleaning Solution was the best cleaning method. (This solution is also used by LIGO.) To measure the linewidth, we lock the cavity to a stable reference, then scan the AOM frequency of the 556 nm laser across the resonance. The transmission is recorded and fit to a Lorentzian curve. Our first measurement on April 26th, 2018 was $\kappa = 2\pi \cdot 1.8$ MHz.

[32]Masterbond, EP21TCHT-1

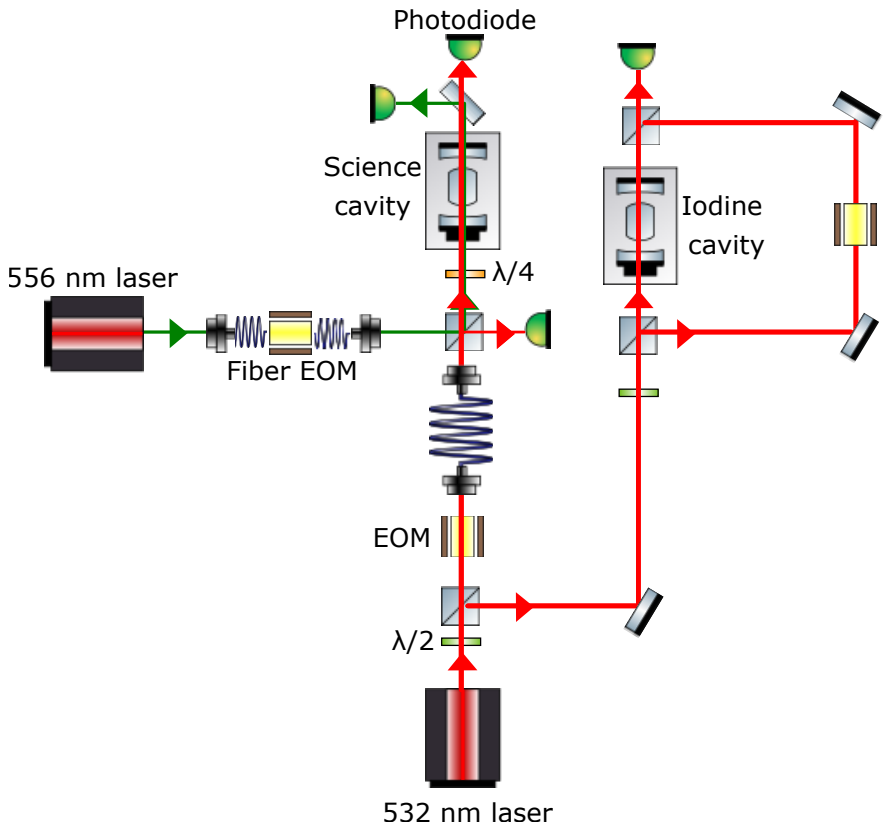

Figure 3.19: Optical setup for 532 nm stabilizing laser and 556 nm lattice laser into the optical cavity.

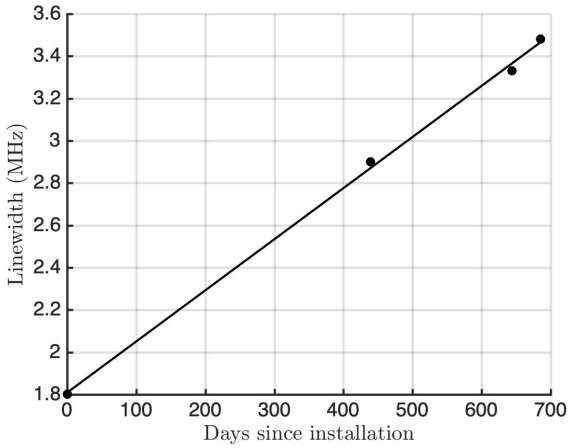

Figure 3.20: Science cavity linewidth as a function of days since installation. The data fit well to a line, $y/\text{MHz} = 0.0024 \cdot \text{days} + 1.81$.

We also measured the length of the cavity by measuring the FSR to find $L_C = 3.63121(4)$ cm. These two measurements allow us to infer the reflectivity as $R = 0.9986$, only slightly more than 1σ lower than spec. The free spectral range can also be measured by scanning the laser frequency this time with an EOM, and was found to be FSR = 4128.0(5) MHz. With these two values, we can calculate the finesse $\mathcal{F} = 2\pi \cdot \text{FSR}/\kappa = 2293$.

Assuming that each mirror has the same reflection and loss values, we expect the ratio of the output to input power to be $\frac{1}{(1+l/(1-l-R))^2}$, where l is the loss of each mirror. Using a photodiode, we measured the power ratio on resonance to be 0.39, corresponding to a loss of $l = 0.05\%$. Although this is quite a bit higher than the 10 ppm mentioned by a manufacturer, we understand that making these mirrors and keeping them perfectly clean is very challenging, and a total transmission through the cavity of 39% is certainly workable.

We found that over the last two years of use the cavity linewidth has linearly increased; see Figure 3.20. We are unsure as to why this is happening, but suspect the cause is Yb build up on the bottom mirror. See more discussion about how this affects our experiment in Section 5.1.1.

3.3.2 Loading

Compensation Coils We now have cold trapped atoms in a MOT, and a stable optical lattice nearby. In order for the atoms to efficiently load into the lattice, the MOT needs to be well overlapped with the mode volume of the lattice. The lattice is fixed by the cavity spacer, but the MOT is slightly mobile, as the atoms are trapped at the zero of the magnetic field. Adding a constant offset to the MOT trapping magnetic field does not affect the quadrupole form, but does move the location of the zero.

Compensation coils, or shim coils, are located around the science vacuum chamber along all three axes to have fine control over the zero point of the magnetic field. For each axis there was a pair of either square or circular coils in the Helmholtz configuration. The size and shape was restricted by our optical and vacuum chamber set up, but each pair was placed as close to the MOT as possible. They were all made from 10–20 windings of magnetic wire, with each pair connected in series to ensure symmetric current in each coil for a uniform magnetic field. The y and z coils are the closest to the MOT and provide a magnetic field of 0.21 Gauss/Amp. The x coil is farther away (constrained by the vacuum pumps) and provides closer to 0.1 Gauss/Amp.

The current ran from the power supply through a control circuit, which allowed us to set up remote operation by the computer for magnetic field switching as part of our sequence. This was also very convenient as the optimal currents for loading into the lattice drifted, and we could perform easy current scans each day to maximize atom number. Details of the control circuit can be found in Appendix 6.3.

Compressed MOT In addition to optimizing the center of mass overlap, it is possible to compress the MOT increasing the atom density and therefore the number of atoms overlapped with the lattice mode volume. This is done simply by increasing the strength of the quadrupole MOT magnetic field by a factor of two, tightening the trap. At the same time the laser intensity in all six MOT beams is ramped down from 100 mW to < 1 mW, while turning off the broadening modulation and moving the beam frequency to -3.2 MHz.

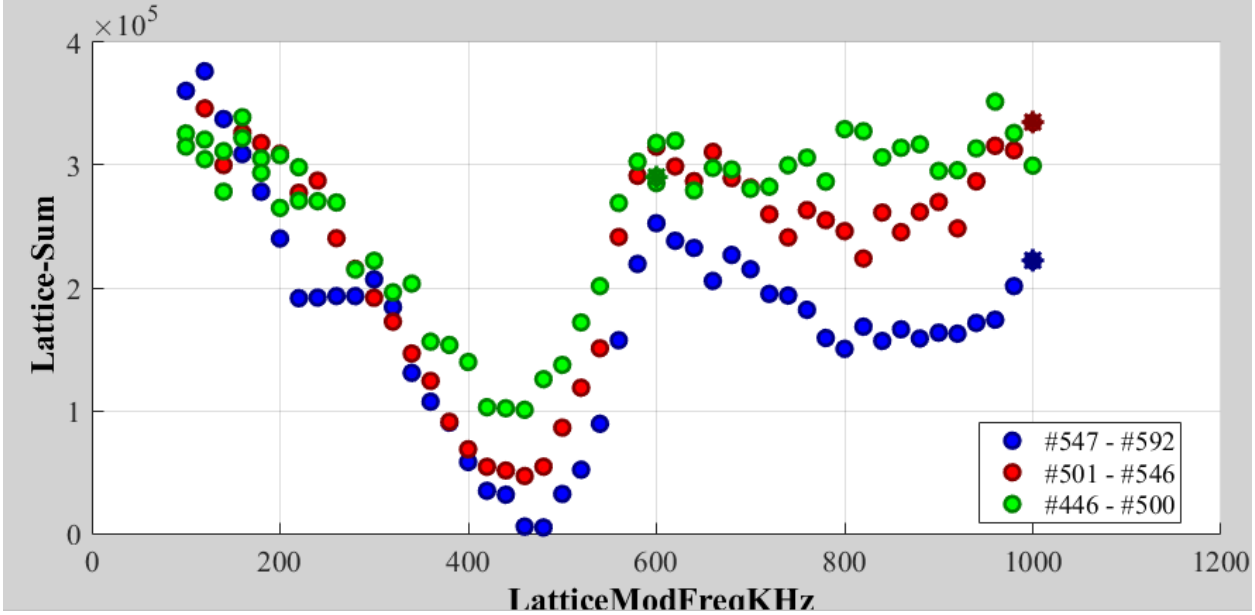

Figure 3.21: Trap frequency measurement via trap lattice modulation. This plot shows atoms being heated out of the lattice as we scan the frequency of modulation. The modulation depths are 0.005 (green), 0.02 (red) and 0.05 (blue). The largest atom loss occurs at a drive frequency 1.85 times the lattice frequency.

This reduces the heating rate by decreasing the scattering rate and allows us to reach lower temperatures, further increasing the number of atoms loaded into the trap.

Lattice Depth The lattice is turned on during the end of the compressed MOT phase to allow atoms to cool into the potential. The depth is estimated using the power in the transmission through the cavity and the known amplification due to the large finesse. It was experimentally confirmed by modulating the lattice depth by 5% at varying frequencies about the expected trap frequency. The largest heating of atoms out of the lattice occurs at 1.85 times the lattice frequency due to the anharmonicity of the potential [JPR01]. The broad resonance is due to the fact that atoms radially far off-center have a smaller trap frequency.

Loading Sequence I have now described all of the technical components that are used when loading our atoms into the optical lattice. The following is a typical loading sequence into the lattice:

1. Initialize all necessary AOMs for MOT loading[33].
2. Turn on MOT coils (7 A) and MOT beams for the MOT loading time, typically one second. Simultaneously set the compensation coils at best current for lattice loading.
3. Ramp up the MOT magnetic field to 15 A over 50 ms.
4. Turn off the slower beam.
5. Turn off broadening of MOT lasers, change detuning and decrease power. Hold for 100 ms.
6. Turn on the lattice and hold with compressed MOT for 30 ms.
7. Turn off MOT beams and hold in lattice.

3.4 Taking Data

3.4.1 Atom Imaging

Software The example loading sequence in the previous section and all other sequences were carried about by an open source software package called Cicero [KK13]. See Figure 3.22 as an example of the steps we would use to load atoms into the lattice. This package allows us to set precise timing sequences with resolutions below a microsecond, set up analog ramps (see step 16 in Fig. 3.22), and easily connect with National Instrument hardware[34].

[33] All AOM frequencies and amplitudes are controlled by Novatech Instruments' DDS9ms.

[34] National Instruments, PCIe-6321

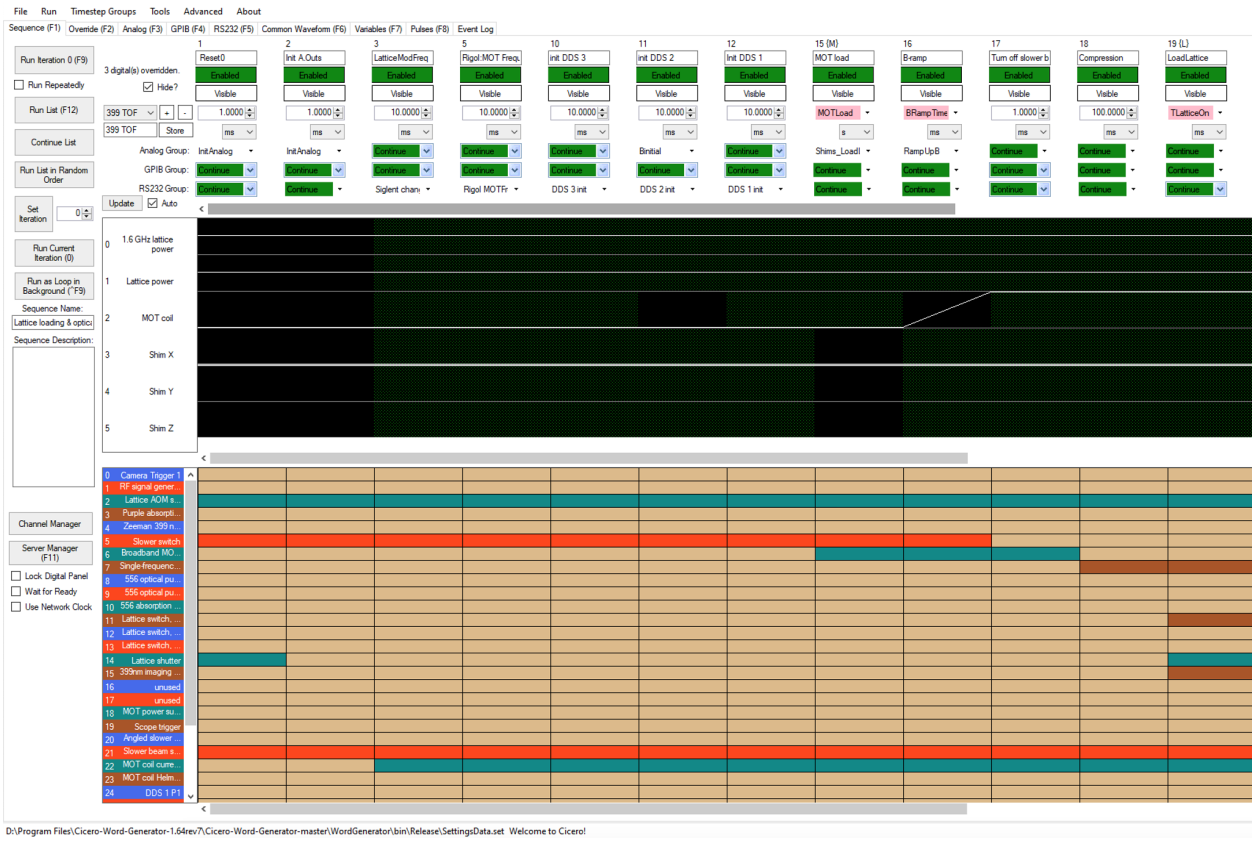

Figure 3.22: Software used to control loading sequences and timing.

Absorption Beam A ≈1 cm diameter on-resonance 399 nm absorption beam is sent through the center of the cavity and directed onto a camera. The absorption cross section for ytterbium is

$$\sigma_a = 3\lambda^2/2\pi, \tag{3.12}$$

where the factor of three comes from the three-fold degeneracy of the excited state. The 399 nm transition has a broad line width compared to the Doppler broadening expected of our cold atoms, so we don't have to worry about the Lorentzian lineshape of the cross section when detuned. The transmission of the beam through the sample is

$$\frac{I_{out}}{I_{in}} = e^{-\sigma_a n L_s}, \tag{3.13}$$

where n is the atomic density and L_s is the path length through the sample. By comparing the intensity with and without atoms, the quantity nL_s can be measured and converted into an atom number. Images for TOF analysis are obtained in 200 μs exposures using an absorption beam with saturation parameter $1.7 \cdot 10^4$.

Image Analysis We use a CCD camera[35] with a nominal 5.5 μm pixel width. We attach a zoom lens providing a magnification of 6.6, which is calibrated using the image of a ruler, resulting in an effective pixel size of $w_p = 36.1$ μm. This enabled us to resolve our atom cloud in the lattice, which is typically not smaller than 70 μm in width. The image was processed in MATLAB and displayed with interactive analysis software that allows us to choose regions of interest and set background regions for calibration. The software calculates a number of useful quantities from our region of interest such as atom number, cloud width, and cloud position.

The atom number is calculated using two images: a cloud image and a background picture with no atoms taken immediately after. Because we are getting a 2D image of a 3D cloud, we can only infer the column density of each pixel. The column density ρ_{col} is calculated by

[35] Allied Vision, Prosilica GB1380

inverting the absorption formula,

$$\rho_{\text{col}} = -\log\left(C_a/C_b\right)/\sigma_a, \tag{3.14}$$

with C_a and C_b the atom and background pixel counts, respectively. The total atom number in the region of interest is a sum over all of the included pixels multiplied by each pixel's area,

$$N_a = \sum \rho_{\text{col}} w_p^2. \tag{3.15}$$

The same calculation was performed in a background region of interest where we did not expect any absorption to be subtracted off for a final atom count.

To calculate the cloud's width and position, each dimension of the cloud is fit to a Gaussian function. For the z direction, each column of pixels in the region of interest is summed and fit to MATLAB's Gaussian function of form,

$$f_G(x) = a_1 e^{-\left(\frac{x-a_2}{a_3}\right)^2} + a_4, \tag{3.16}$$

where a_3 is the $1/e$ width of the fit, and the width definition we will use for the rest of the thesis is the $1/e^2$ width $\sigma_i = a_3/\sqrt{2}$, where i refers to the direction.

Time-of-Flight Temperature Method Time-of-flight image analysis is the standard method for analyzing a sample's temperature in the field of neutral atoms. It involves taking a series of absorption images at several time delays. A thermal cloud in free expansion has a Gaussian width that grows as,

$$\sigma_i = \sqrt{\sigma_{i,0}^2 + \sigma_{v_i}^2 t^2}, \tag{3.17}$$

where $\sigma_{i,0}$ is the initial width of the trapped atoms and $\sigma_{v_i} = \sqrt{k_B T_i/m}$ is the thermal velocity spread of atoms at temperature T_i in the $i = x, y$, or z direction [BMZ02].

Following the loading sequence described in Section 3.3.2, the atoms are non-adiabatically released from the lattice by turning off the lattice light with an AOM. Here, the adiabatic criteria is that the atoms are released in a time much faster than their trap oscillation period.

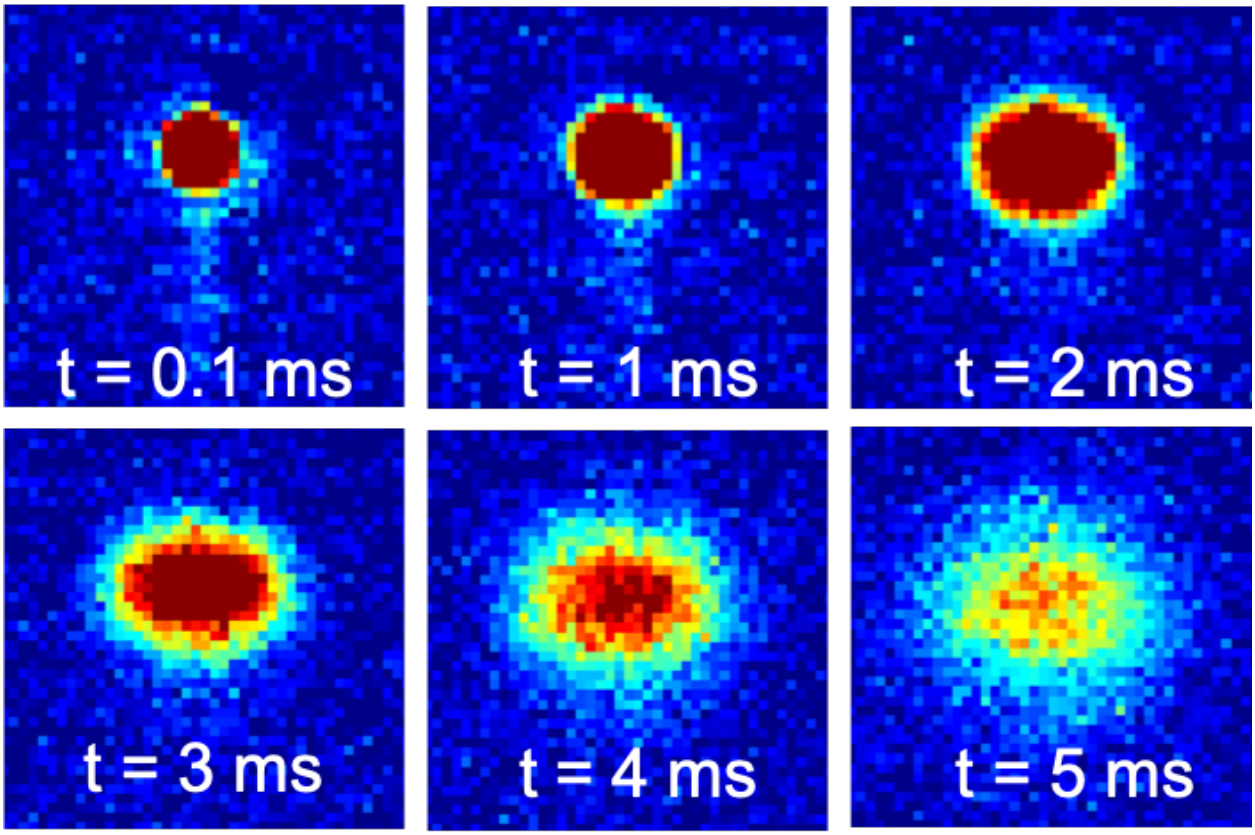

Figure 3.23: Images taken of the atom cloud after a variety of wait times from releasing them from the optical lattice. Red represents high density and blue low density.

We release them in 100 ns with a trap oscillation period typically >1 μs. Each time they are loaded and released they are allowed to expand for a variable time ranging from 0-10 ms. Typically after 7 ms the cloud has expanded to more than twice its original size and is too diffuse to obtain a reliable width. An example of the time-of-flight images is in Figure 3.23. An example of the analysis of these images with their fit temperatures is in Figure 3.24.

3.4.2 Cavity Transmission

A simple schematic of the cavity laser can be seen in Figure 3.19. After cavity transmission the 532 nm and 556 nm laser are separated by a filter and the 556 nm light is directed into a photodiode. For both our new temperature measurement and our Bloch oscillations, we

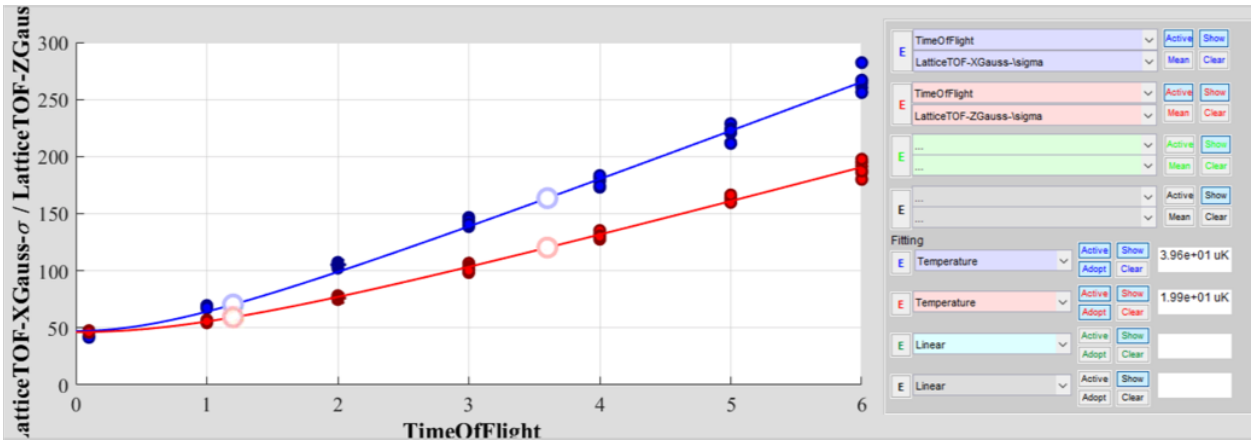

Figure 3.24: Gaussian widths fit for the x and z directions of an expanding atom cloud, fit to Eq. 3.17, resulting in $T_x = 39.6$ μK and $T_z = 19.9$ μK. This image is taken directly from our analysis program. These fits were performed with 10 data points taken at each of the seven time of flight times. The x axis is in milliseconds, and the y axis is in microns.

need a very weak laser (< 1 μW) which is below the threshold of the typical photodiode[36] we use around the lab due to excess electrical noise.

Focusing on optimizing signal-to-noise for our future Bloch oscillation experiment, we chose to use an avalanche photodiode[37] (APD). This photodiode has an internal gain stage that adds relatively little noise (compared to, for example, a voltage amplifier). It also has a large wavelength range of 200–1000 nm and a large bandwidth of DC to 10 MHz, allowing it to be useful for many future applications, and was immediately put to use for our our new temperature measurement.

For our dark matter measurements, we do not need to use the entire bandwidth range (need up to ∼10 kHz) so we use the photodiode at maximum gain. The APD's responsivity at our wavelength is 20 A/W and has a transimpedance gain of 500 kV/A for high-impedance termination. With our wavelength we expect 10 mV/nW at maximum gain.

The background noise expected from the APD is 10^{-13} W/$\sqrt{\text{Hz}}$. Using a bandwidth of

[36] Thorlabs, PDA36A

[37] Thorlabs APD410A2

10 kHz for our Bloch oscillation measurement, the expected background noise contribution of the APD is 0.01 nW, or 0.1 mV at maximum gain. The new temperature measurement is performed in < 10 μs and needs the entire bandwidth to capture the atom dynamics, and therefore expects background noise of 0.3 nW. Without gain the expected background noise is 1 mV.

Shot noise from the laser also contributes to the expected transmission noise. The standard deviation of the laser power due to shot noise is $\sigma_p = \sqrt{2\mathcal{P}\hbar\omega B}$ where $\mathcal{P}$ is the laser power and B is the detector bandwidth. Our APD has a minimum gain of 50, meaning the expected measurement noise due to shot noise is amplified by a factor of 50.

CHAPTER 4

Applications

4.1 New Atomic Temperature Measurement

This section is based on the manuscript "Cavity probe for real-time detection of atom dynamics in an optical lattice" written by me and my co-authors, Paul Hamilton and Robert Niederriter, in preparation for submission to Physical Review Letters.

The spatial distribution of atoms in an optical lattice is important for applications of trapped atoms such as cavity optomechanics [BBS12], atom interferometry [XJP19], and real-time observation of Bloch oscillations [PTH09, PMC09b, KKV16]. The prototypical cavity QED system consisting of an atomic two-level system and an optical cavity provides a minimally invasive means to probe the atomic spatial distribution. This coupled system has been used successfully for atom counting [ZMC12], optomechanical sensing [BBS12], and spin squeezing [SLc10, CGW16].

Measuring the spatial properties of a distribution extending over many lattice sites requires nearly uniform coupling at each lattice site. Typically atoms are trapped in a far-detuned standing wave and probed with a different cavity mode near the atomic resonance [BBS12, SLc10, CGW16] leading to non-uniform coupling between the atoms and probe. The same standing wave can be used to both trap and probe the atom density [PTH09, KKV16], but this scheme reduces flexibility to independently choose the trap depth and probe detuning; in particular, the trap detuning from the atomic resonance must be small enough to allow sufficient sensitivity for probing. In addition, strong atom-cavity coupling in this case leads to coupling between the atom dynamics and trapping field, which is not always desired.

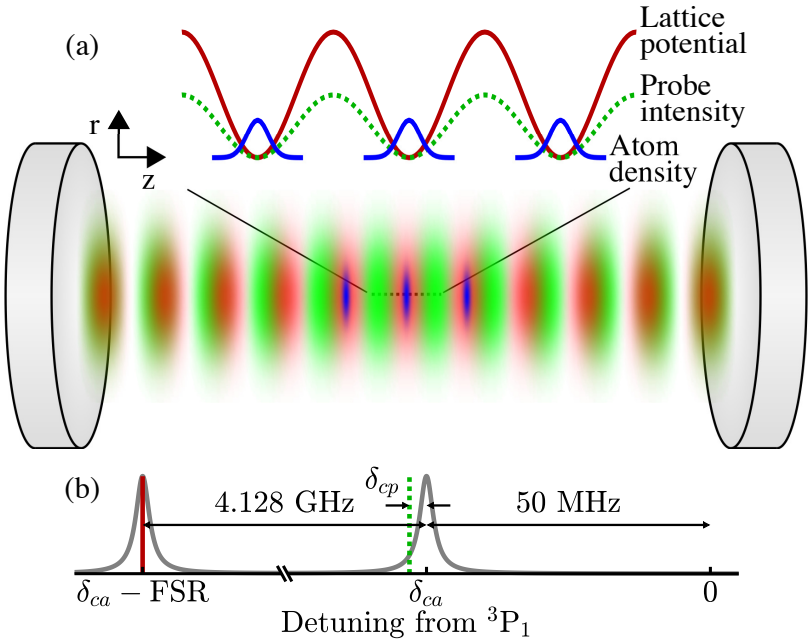

Figure 4.1: Experimental setup. (a) Two standing waves of light are formed by driving adjacent longitudinal modes of an optical cavity. The red (solid) line indicates the red-detuned trapping lattice used to confine ^{174}Yb atoms, shown as blue Gaussian distributions. The green (dotted) line represents a weak probe beam used to measure the spatial extent of the atom density. Note the lattices are not drawn to scale; there are actually $\approx 300,000$ lattice sites between the mirrors. (b) Detuning of lattice (red solid), probe (green dotted), and cavity resonances (black) from the $^3P_1$ transition. δ_{ca} and δ_{cp} are the detuning of the cavity resonance from the bare atomic transition and the probe beam, respectively.

The difference between trap and probe wavelengths, λ_ℓ and λ_p respectively, can lead to a limited range over which atoms can be coupled uniformly to the probe. The distance (in lattice sites) over which the atomic distribution remains nearly uniformly coupled to the probe is $d_{\text{uniform}} \approx \pi/\Delta\phi$, where $\Delta\phi = 2\pi(\lambda_\ell - \lambda_p)/\lambda_p$ is the phase shift of the probe standing wave between adjacent sites of the trap standing wave. When using a far-off-resonance lattice and a near detuned probe beam with a typical wavelength difference of $\sim$50 nm, $d_{\text{uniform}} < 10$. While this can be useful for addressing individual lattice sites [BBS12], it limits the observation of global dynamics. In contrast, this work uses a trap lattice separated from the probe by one free spectral range (FSR) of 4128.0(1) MHz, as shown in Fig. 4.1. Over the $\approx$1000 lattice sites ($\approx$300 μm) occupied by the atoms, the probe standing wave is shifted by only $\approx$1 nm. The coupling uniformity allows observing spatial dynamics of the trapped atoms while remaining far off resonance ($2.3\times10^4\,\Gamma_3$) compared to the narrow linewidth of the Yb intercombination transition, $\Gamma_3 = 2\pi\times180$ kHz. The narrow transitions in alkaline-earth-like atoms such as Sr and Yb provide opportunities for trapping with moderate detuning as used in this work.

Site-independent coupling enables extracting global information about the atomic distribution in real time. By time-averaging or probing using adjacent cavity longitudinal modes, others have demonstrated coupling that is independent of atom position [CGW16], [VBE17], [HBV19]. In contrast, we demonstrate coupling that is independent of lattice site, but importantly still dependent on position within the lattice site. In this way, we are able to continuously monitor the sub-wavelength motion on microsecond timescales of atoms both tightly bound in the lattice and recently released from the lattice. We derive theoretical expressions for the uniform probe coupling to a trapped atomic distribution and demonstrate an application of this method for a minimally invasive temperature measurement performed in $<$10 μs on ytterbium atoms that begin trapped in an optical lattice.

4.1.1 Theory

Consider a cloud of ultracold two-level atoms with atomic resonance frequency ω_a trapped in a 1D optical lattice with potential depth U_t and optical frequency resonant with a longitudinal mode of a Fabry-Perot cavity. A probe lattice is also present with trap depth $U_p \ll U_t$ and a frequency ω_p, near resonance with another longitudinal mode at ω_c and nearly one FSR detuned from the trap lattice at ω_ℓ (see Fig. 4.1). Interaction of the cavity with the atoms shifts the cavity resonance and therefore changes the probe transmission through the cavity. We start by deriving the expected cavity mode shift due to the atom-cavity coupling and its effect on the probe transmission. We then discuss the specific atomic distribution for our system and derive the time-dependent probe transmission during axial and radial expansion after releasing the atoms from the trapping lattice.

The atom-cavity system acts as coupled oscillators with normal modes detuned from atomic resonance by

$$\Delta\omega_\pm = \frac{-\delta_{ca} \pm \sqrt{\delta_{ca}^2 + \Omega^2}}{2}, \tag{4.1}$$

where $\delta_{ca} = \omega_c - \omega_a$. $\Omega = 2g_0\sqrt{N_a\mathcal{I}}$ is the collective vacuum Rabi frequency for N_a atoms trapped in the lattice with single-atom vacuum Rabi frequency $2g_0$ and dimensionless atom-probe overlap integral $\mathcal{I}$ [RTB89]. When $\delta_{ca} = 0$, the system exhibits symmetric mode splitting, known as vacuum Rabi splitting, with peaks detuned from the bare cavity by $\pm\Omega/2$. In the far-detuned limit where $|\delta_{ca}| \gg \Omega$, the resonances split into a cavity-like mode, $\Delta\omega_-$, and an atom-like mode, $\Delta\omega_+$. We will focus on the cavity-like mode which is shifted from the bare cavity resonance, in the far red-detuned limit ($\delta_{ca} \ll 0$), by

$$\Delta\omega_- = \frac{\Omega^2}{4\delta_{ca}}. \tag{4.2}$$

Loss from transmission through the cavity mirrors leads to a broadening of this mode given by the cavity full-width-half-max linewidth, κ. Scattering into free space due to spontaneous emission also leads to broadening but is negligible in the far-detuned limit considered below. In addition to a shift from the atom-cavity coupling, the probe frequency can be detuned, $\delta_{cp} = \omega_c - \omega_p$, from the bare cavity resonance resulting in a total detuning of $\Delta\omega = \Delta\omega_- - \delta_{cp}$.

See Fig. 4.1.

The cavity transmission power, Θ, at detuning $\Delta\omega$ follows a Lorentzian lineshape

$$\Theta = \Theta_0 \frac{1}{1 + \left(\frac{\Delta\omega}{\kappa/2}\right)^2}, \tag{4.3}$$

where Θ_0 is the resonant transmission of the empty cavity. Monitoring the cavity resonance shift thus gives information on the evolution of the atomic spatial distribution as the coupling integral, $\mathcal{I}$, changes (Eq. 4.4).

Next we consider dynamics of the atomic distribution when the trapping lattice is turned off non-adiabatically and the atoms begin to freely expand. Observing the resonance shift of the cavity mode via the probe transmission provides a real-time measurement of the width of the atomic distribution. We obtain a functional form for the probe transmission given the atomic distribution in the lattice and later use this as a model to extract the temperature from probe transmission measurements. The timescales for changes in transmission due to the axial and radial dynamics are determined by the corresponding spatial scale of the probe beam, which is a TEM_{00} mode of the optical cavity. The atoms are assumed to be confined at the center of the optical cavity over a region much smaller than the Rayleigh length.

The coupling integral,

$$\mathcal{I} = \int \rho(\phi, r, z, t) M(\phi, r, z) \mathrm{d}V, \tag{4.4}$$

is a dimensionless overlap integral between 0 and 1 indicating the coupling between the atomic spatial distribution given by the normalized number density $\rho = \rho_\phi \rho_r \rho_z$ and the cavity probe through its spatial intensity profile, $M = M_\phi M_r M_z$. The probe mode and the atomic distribution are cylindrically symmetric and we can factor the coupling integral into radial and axial contributions, $\mathcal{I} = \mathcal{I}_r \mathcal{I}_z$. The spatial mode near the waist is

$$M(r, z) = \sin^2(k_p z) \exp\left(-2r^2/w_\ell^2\right) \tag{4.5}$$

where $k_p = 2\pi/\lambda_p$ is the wavenumber of the probe beam. Because the waist is much larger than the lattice spacing, $w_\ell \gg \lambda_p$, the axial overlap integral $\mathcal{I}_z$ changes much faster than the radial overlap integral $\mathcal{I}_r$.

In the 1D trapping lattice, the initial positions and velocities of thermalized atoms at each lattice site are well described in the simple harmonic oscillator limit by Gaussian distributions with standard deviations $\sigma_{i,0}$ and $\sigma_{v_i} = \sqrt{k_B T_i/m}$, where $i = r, z$ refer to the radial and axial directions, respectively, k_B is the Boltzmann constant and T_i is the temperature. When the atoms are released from the trapping lattice, the atomic distribution evolves as [BMZ02]

$$\rho(r,z,t) = \rho_r(r,t)\rho_z(z,t) = \frac{e^{-\frac{r^2}{2\sigma_r^2(t)}}}{\sqrt{2\pi}\sigma_r^2(t)} \frac{e^{-\frac{z^2}{2\sigma_z^2(t)}}}{\sigma_z(t)}, \tag{4.6}$$

with

$$\sigma_i^2(t) = \sigma_{i,0}^2 + \sigma_{v_i}^2 t^2. \tag{4.7}$$

The atoms start localized at the anti-nodes of the trap lattice and the nodes of the probe lattice (Fig. 4.1(a)), which we define as $r = z = 0$. Because we have uniform coupling over the $\approx 10^4$ lattice sites that the atoms occupy, the overlap integral for a single lattice site describes the dynamics of the entire ensemble. While below we consider a thermal distribution with no coherence between trapping lattice sites, a full quantum mechanical calculation of the evolution of the spatial distribution can be used when coherent effects are important [PTH09].

With the functional form of the lattice and the atomic distribution, we can evaluate the coupling integrals for both directions. The axial integral is

$$\begin{aligned} \mathcal{I}_z(t,T_z) &= \frac{1}{2}\left(1 - e^{-2k_p^2\sigma_z^2(t)}\right) \\ &= \frac{1}{2}\left(1 - e^{-2k_p^2\left(\sigma_{z,0}^2 + \frac{k_B T_z}{m}t^2\right)}\right) \end{aligned} \tag{4.8}$$

and the radial integral is

$$\begin{aligned} \mathcal{I}_r(t,T_r) &= \left(1 + \frac{4}{w_\ell^2}\sigma_r^2(t)\right)^{-1} \\ &= \left(1 + \frac{4}{w_\ell^2}\left(\sigma_{r,0}^2 + \frac{k_B T_r}{m}t^2\right)\right)^{-1}. \end{aligned} \tag{4.9}$$

These overlap integrals set the normal mode frequency (or cavity resonance shift in the far-detuned limit), and produce the time and temperature dependence of the probe beam transmission.

Verification of Atomic Distribution I would like to make a digression into some analysis I performed on the expected atomic distribution widths. Originally, we attempted to specify the initial width of our atom cloud, $\sigma_{i,0}$, as a function of temperature based on our known lattice potential. We found that for the radial direction this resulted in fit temperatures that did not match our TOF measurement, in comparison to successfully letting $\sigma_{i,0}$ be a free fit parameter. As the TOF fit also allows $\sigma_{i,0}$ to be unspecified, in retrospect it is perhaps unsurprising that freeing it improved agreement between the TOF method and our new method. Despite not including details of this analysis in the final version of our paper, we still found it interesting because of a mismatch in our expected widths and our measured widths, which is why I include it here. I start with analysis for the axial direction which resulted in expected widths that matched fit widths. I follow by discussing the mismatch in the radial expected widths compared to the measure width of our trapped atoms.

Ytterbium atoms in a lattice are well approximated as non-interacting particles. To determine our specific ensemble's axial spatial distribution, I performed a variety of both quantum and classical estimations assuming a thermal sample.

The quantum energy eigenstates for the full sinusoidal axial lattice potential are not particularly simple, so I evaluated a variety of approximate potentials and analyzed the quality of the estimation. I start with the simple harmonic oscillator potential, and build up a few other approximations based on the results. I then compare these quantum results to a classical numerical simulation.

The full axial lattice potential is $U_z(z) = U_t \sin^2(k_\ell z)$. When the energy of the potential is much larger than the energy of the atoms, $U_t \gg k_B T_z$, we expect the atoms to only feel the bottom of the potential, in other words $|k_\ell z| \ll 1$. With that approximation we expand the lattice potential as $U_z(z) \approx U_t(1 - (k_\ell z)^2)$, a simple harmonic oscillator (SHO). The effective trap frequency can be determined by equating the SHO coefficients $\frac{1}{2} m\omega_t^2 z^2 = U_t k_\ell^2 z^2$, resulting in a trap frequency,

$$\omega_t = \sqrt{\frac{2U_t k_\ell^2}{m}}. \tag{4.10}$$

The wavefunctions of the SHO are

$$\Psi_n(z) = \frac{1}{\sqrt{2^n n!}} \left(\frac{m\omega_t}{\pi\hbar}\right)^{1/4} e^{-\frac{m\omega_t^2 z^2}{2\hbar}} H_n\left(\sqrt{\frac{m\omega_t}{\hbar}} z\right), \tag{4.11}$$

where H_n are the Hermite polynomials. The ensemble's spatial Boltzmann thermal distribution with characteristic temperature T_z is then

$$\rho_z(z) = \frac{\sum_{n=0}^{\infty} |\Psi_n(z)|^2 e^{-\frac{E_n}{k_B T_z}}}{\sum_{n=0}^{\infty} e^{-\frac{E_n}{k_B T_z}}}, \tag{4.12}$$

where the energy eigenvalues are $E_n = \hbar\omega_t(n + 1/2)$. This summation was numerically performed in MATLAB and and $\rho_z(z)$ was fit to a Gaussian. Based on the fit ρ_z is well approximated by a Gaussian with standard deviation

$$\sigma_{z,0} = \sqrt{\frac{(\langle n\rangle + 1/2)\hbar}{m\omega_t}}, \tag{4.13}$$

where the thermal occupation number is

$$\langle n\rangle = \left(e^{\frac{\hbar\omega_t}{k_B T}} - 1\right)^{-1}. \tag{4.14}$$

This standard deviation is shown in black in Figure 4.2 as a function of the atomic temperature. Somewhat surprisingly the Boltzmann summation of the SHO wavefunctions is precisely a Gaussian, as proved in pages 46–51 of Feynman's Statistical Mechanics: a set of lectures[Fey73].

The next assumption, which I call the warm SHO, is that the average atom energy is much larger than the ground state of the oscillator, $k_B T_z \gg \hbar\omega_t$. Qualitatively, this assumption states that the majority of the atoms are not in the ground state of the oscillator. By Taylor expanding $\langle n\rangle$ and using $\langle n\rangle \gg 1$, the standard deviation of the Gaussian simplifies to

$$\sigma_{z,0} = \sqrt{\frac{k_B T_z}{m\omega_t^2}}. \tag{4.15}$$

The final quantum mechanical consideration, named the chopped SHO, accounts for the fact that the potential is not an infinite simple harmonic oscillator, but one with a fixed depth. This was implemented in the numerical calculation of the ensemble spatial distribution by

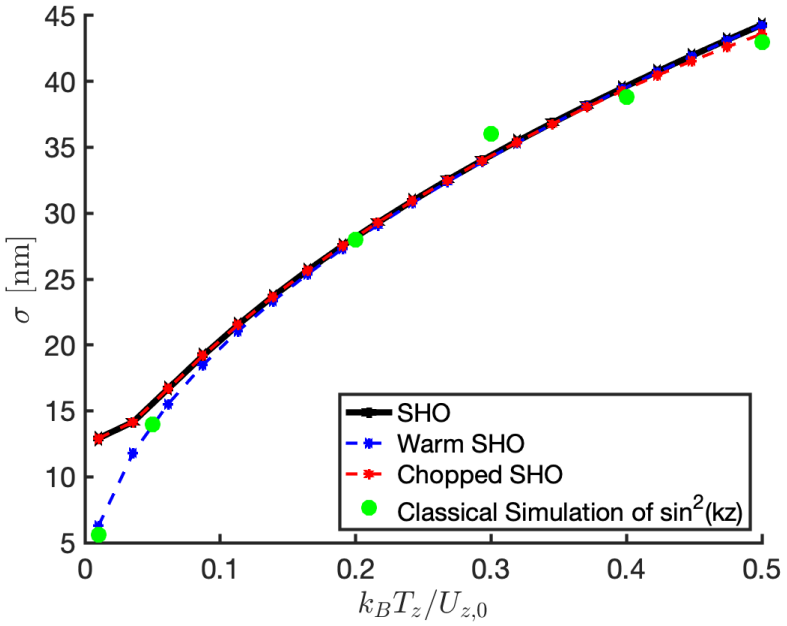

Figure 4.2: Comparison of Gaussian widths for the simple harmonic oscillator (SHO), the warm SHO and the chopped SHO, all defined in text, as well as a classical simulation of the full sinusoidal potential. All approximations converge at our typical thermalization temperature $k_B T_z = 0.2 U_t$.

only including energy levels which satisfy $E_n < U_t$. I did not determine a closed form solution for this standard deviation, but the Gaussian fit width can be compared with the widths from the other approximations in Figure 4.2.

The full sinusoidal potential was simulated classically. A large number of particles were assigned energies from a Boltzmann distribution. The particles started at $z = 0$, and were assigned initial velocities consistent with energy conservation. They were released, and incrementally stepped according to the force from the local curvature of the potential. After waiting a large enough number of steps such that the distribution was no longer changing in time, the distribution was fit to a Gaussian. Figure 4.2 shows that this simulation agrees well with the warm SHO, which is expected as there is no zero point energy in the classical simple harmonic oscillator.

All of approximations work in their appropriate limits, namely the warm SHO breaks down when $k_B T_z/U_t \ll 0$ and that the chopped SHO breaks down when $k_B T_z/U_t \gg 0$. The approximations converge between $0.15 < k_B T_z/U_t < 0.45$ to $\sigma_{z,0}$ values within 2%, which is within the typical thermalization temperature of our atoms, $k_B T_z \approx 0.2 U_t$. See Section 6.4 in the Appendix for information about the simulation code. Directly measuring atomic ensemble distributions in individual lattice sites is beyond our absorption measurement spatial resolution. However, I note that for the axial direction the temperature fits did not change when floating $\sigma_{z,i}$, and the fit value for the width matches very well with all of the above approximations.

For the radial direction, the Gaussian approximation was confirmed directly by absorption imaging; see Figure 4.3. Interestingly, the width is larger than expected based on some simple calculations. The simplest model approximates the Gaussian potential as a classical simple harmonic oscillator, resulting in an expected width of

$$\sigma_{r,\mathrm{SHO}} = \sqrt{\frac{k_B T_x w_\ell^2}{4U_t}} = 40\ \mu\mathrm{m}, \tag{4.16}$$

using our typical temperature of $T_x = 0.3 U_t/k_B$. This can be compared to the measured width of 70 μm. We are deep in the classical regime as our expected thermal average level occupation number for an SHO is 6000. We do expect a broader width than this simple model because we have yet to take into account that we are in a 3D lattice. A more accurate model integrates over the z-direction in the 3D phase space weighted by Boltzmann factors. The thermal phase space is given by

$$\rho_{\mathrm{PS}} = e^{-\frac{H}{k_B T}} r\, \mathrm{d}r\, \mathrm{d}z, \tag{4.17}$$

where the Hamiltonian $H = U_t M(r, z)$ is the lattice potential and $1/k_B T$ is the Boltzmann weight. I numerically integrated out the z dependence and fit the result to a Gaussian, leading to a larger estimate, $\sigma_{r,\mathrm{PS}} = 48\ \mu$m; the result is shown in Figure 4.4. This model has some obvious flaws, as we have different temperatures in the z direction and the r direction and the Boltzmann distribution assumes the entire sample has a uniform temperature. In addition, the z direction is not well represented classically as the average level occupation

number is $\mathcal{O}(1)$. It was at this point that we realized retaining $\sigma_{r,i}$ as a fit parameter rather than trying to obtain a functional form with respect to the temperature was more efficient and less model sensitive. Perhaps a more sophisticated calculation would yield the correct width (and a more precise fit), and we would be interested in looking into this further in the future.

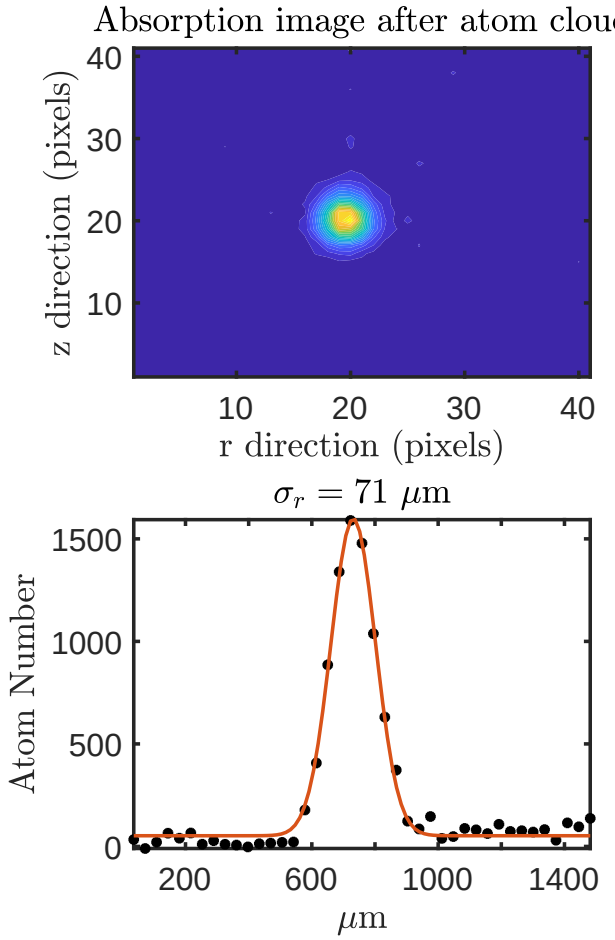

Figure 4.3: Absorption image of the atom cloud in the optical lattice. Yellow represents high density and blue represents low density. On the bottom plot, each column from the picture was averaged (black points) and the resulting row fit (red) to a Gaussian resulting in a width of $\sigma_{r,i} = 71$ μm.

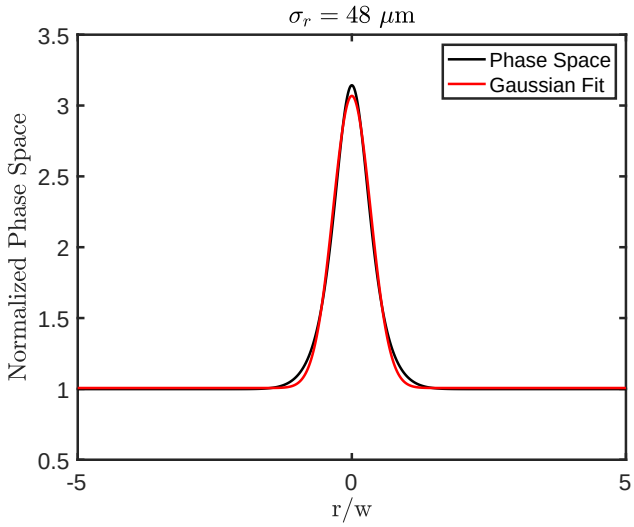

Figure 4.4: A 1D radial projection (black) of the 3D phase space, Eq. 4.17, integrated over the axial direction, fit to a Gaussian (red).

4.1.2 Experiment

A weak probe beam ($U_p < 0.05\,U_t$) is coupled into an adjacent TEM_{00} mode of the optical cavity with a linear polarization orthogonal to the trap lattice polarization and red-detuned $\delta_{ca} = -2\pi \times 50$ MHz from the atomic resonance. The intensity of the probe beam is kept small to prevent mechanical forces during the free expansion of the atomic cloud. This has been verified through numerical simulations and by observing the same temperature values when the probe is blue-detuned from the atom transition. The trapping lattice detuning is set one FSR red-detuned from the probe beam, causing the probe and lattice standing waves to be $\pi/2$ out of phase at the center of the cavity. The relative positions of the trap and probe lattices are shown in Fig. 4.1.

The atoms are released non-adiabatically by switching off the trapping lattice in ≈100 ns. They expand for 10 μs–10 ms (Fig. 4.5a), where large overlap with the probe beam occurs (Fig. 4.5b) and the normal mode resonance is shifted by up to several MHz (Fig. 4.5c). Fast temperature measurements are performed by monitoring the probe transmission through the optical cavity using a 10 MHz bandwidth avalanche photodiode (APD). The signal is digitized with a 100 MHz bandwidth oscilloscope, and fit with Eq. 4.3 using Eqs. 4.8 and 4.9.

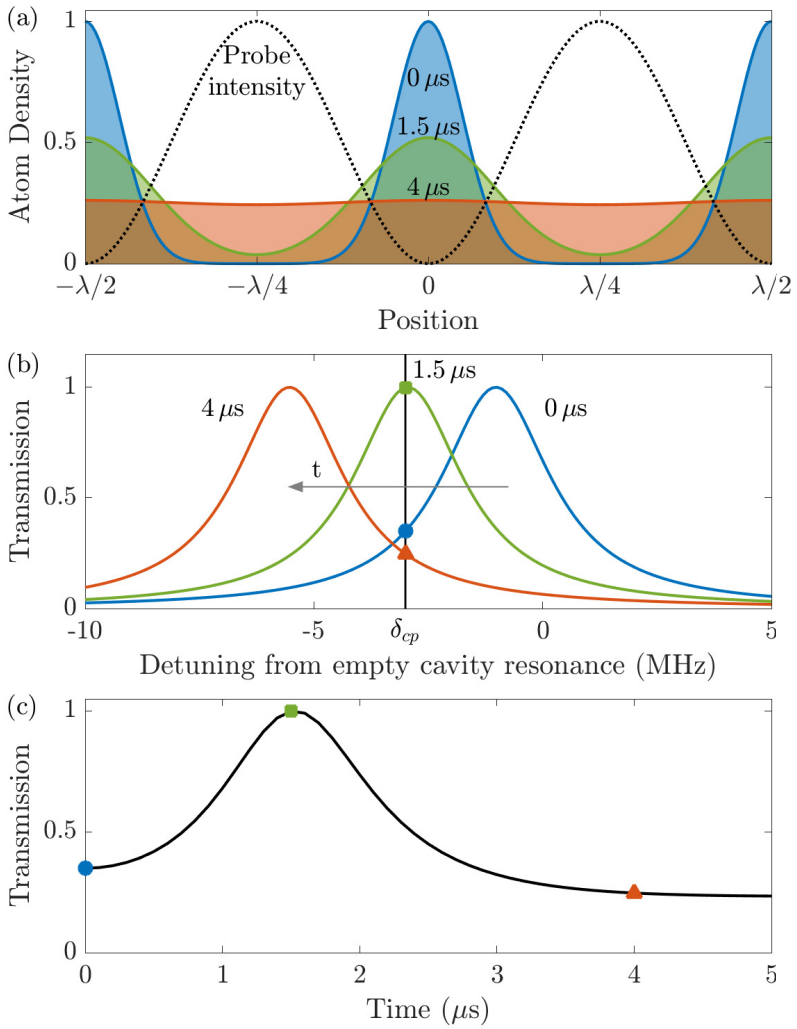

Figure 4.5: Time evolution of the overlap between the atoms at temperature 30 μK and the probe beam. (a) Atom density at t=0 μs (blue), 1.5 μs (green), and 4 μs (red) after atoms are released from the optical lattice. The black (dotted) curve shows the 556 nm probe standing wave intensity for reference. (b) Cavity transmission spectrum showing the normal mode resonance shift at the same 0, 1.5, and 4 μs time delays after releasing the atoms from the optical lattice. The vertical line indicates fixed probe detuning at $\delta_{cp} = -2\pi \times 3$ MHz, and the three shapes indicate where the laser frequency falls on the Lorentzian transmission curve at each time. (c) Probe transmission vs time. Colored shapes correspond to times in part (b).

4.1.3 Results

We observe that the strong atom-cavity coupling has a predictable effect on the probe beam transmission through the cavity. Qualitatively, the atoms' expansion changes the overlap with the probe mode, which shifts the cavity resonance frequency. The atom expansion sweeps the cavity resonance frequency across the probe frequency, mapping out the Lorentzian cavity transmission (Eq. 4.3). At long time scales, the transmission tends to the empty cavity value as the atoms leave the cavity mode. Quantitatively, we fit the transmission curves with the models described above to measure the axial and radial temperatures. The probe beam transmission is recorded for the axial and radial timescales and compared with standard time-of-flight (TOF) temperature measurements.

For different values of the lattice depth (which corresponds to different atomic temperatures), the temperature of the atoms is measured using TOF and the new technique each ten times. As shown in Fig. 4.6, the new probe measurement obtains similar temperatures to TOF for both axial and radial directions. There are several systematic differences between the two methods. In particular, the probe measurement is sensitive to the coupling of all atoms in the optical cavity mode. Since the signal in the absorption measurement used for TOF is proportional to density it is less sensitive to a background of diffuse atoms.

Time-of-Flight The time-of-flight (TOF) measurements are performed with a 1 cm radius 399 nm absorption beam with saturation parameter 1.7×10^{-4}. The beam is directed along the radial axis of the lattice into a CCD camera with a lens resulting in an effective pixel size of 36(1) μm. Typically six absorption images are taken at post-lattice-release times ranging from 0–5 ms, loading new atoms for each image. At each delay time, the radial and axial widths are determined by Gaussian fits. Fitting the measured $\sigma_i(t)$ with Eq. 4.7 yields the sample's temperature in each direction.

In the TOF measurement a 3% uncertainty in the magnification of the imaging system leads to a 3% uncertainty in the temperature. A tilt of the absorption beam with respect to the horizontal axis leads to an effective measured temperature of $T_z' = T_z \cos^2\theta_t + T_r \sin^2\theta_t$,

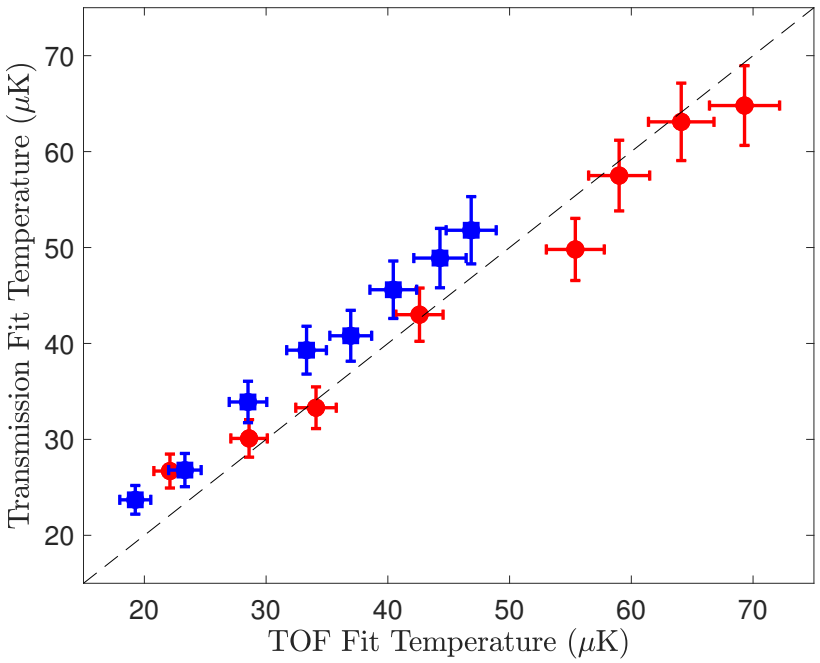

Figure 4.6: Comparison of axial (blue squares) and radial (red circles) temperatures obtained using the new method and the standard time-of-flight technique. The error bars are the quadrature sum of the systematic errors described in the text and the standard error on the mean of ten data points.

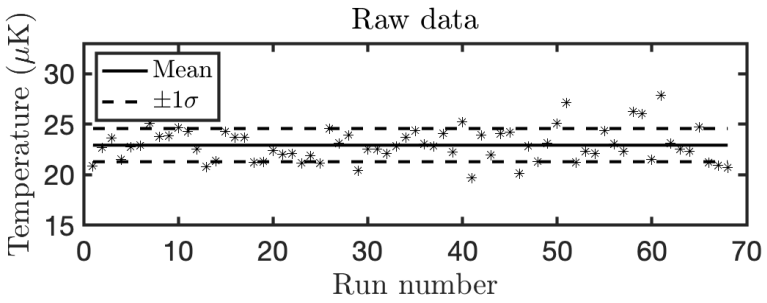

Figure 4.7: TOF measurement taken every 15 seconds for 15 minutes. Fitting the data results in a linear drift of 0.03 ± 0.04 μK/minute, consistent with no drift.

where the tilt angle is $\theta_t = 13.1 \pm 1.8°$. The quoted axial temperature corrects for this offset and produces a 1% uncertainty on T_z. We estimate an upper limit to the heating from the absorption beam of $\approx$1 μK at our saturation parameter 1.7×10^{-4}. These added in quadrature lead to a 5% systematic error. The statistical error on a TOF temperature measurement comprising seven absorption images is 10%, leading to an effective single-shot error of 27%.

Beyond these quantified systematics we performed a variety of other checks that did not significantly contribute errors. Because there was often at least a minute delay between TOF and probe data, we checked that the TOF measurements did not drift. Over the course of 15 minutes, a time-of-flight temperature measurement was taken every 15 seconds, see Figure 4.7 for results. Fitting the data results in a negligible drift of 0.03 ± 0.04 μK/minute. We also saw negligible systematics due to absorption beam power and position, lattice turn off time, and non-Gaussian distribution effects (see Figure 4.3).

New Temperature Measurement The transmission function (Eq. 4.3) is fit to the measured probe transmission using a non-linear least squares algorithm, with five free parameters: $\Theta_0, N_a, \sigma_{i,0}, T_i$, and δ_{cp}. The experimentally set initial probe detuning, δ_{cp}, is included as a free parameter to account for background atoms shifting the resonance by a constant value. Fig. 4.8 shows example raw data traces of the probe beam transmission observed after release of the atoms. Experimentally using a probe detuning such that the experiment starts

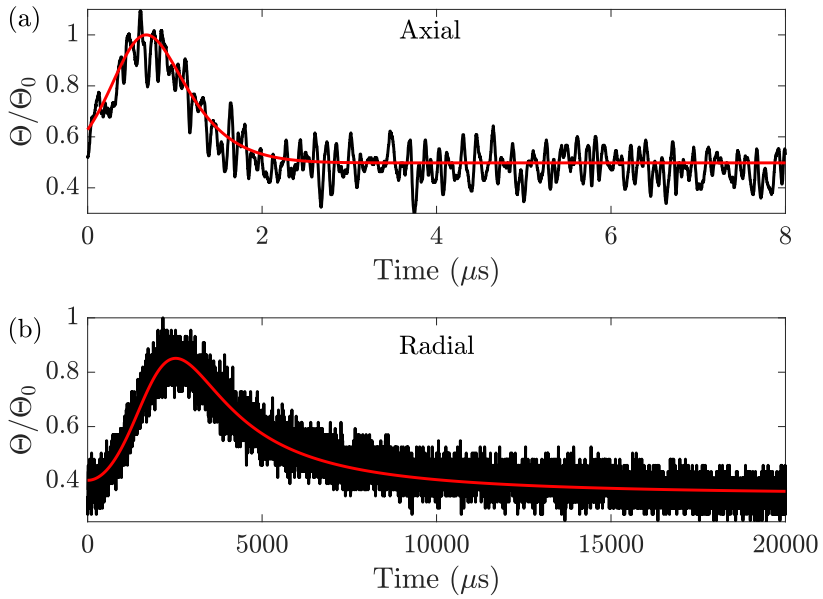

Figure 4.8: Example normalized raw traces (black) of probe transmission after releasing the atoms from the trapping lattice. The fits (red) use five free parameters: $\Theta_0, N_a, \sigma_{i,0}, T_i$ and δ_{cp}. The data were taken with $\delta_{ca} = -2\pi \times 50$ MHz, $N_a = 8 - 10 \times 10^5$ atoms. The axial trace (a) was taken with $\delta_{cp} = -2\pi \times 4$ MHz and TOF $T_z = 45$ μK, and the radial trace (b) was taken with $\delta_{cp} = -2\pi \times 2$ MHz and TOF $T_r = 22$ μK. Each trace amounts to a single-shot temperature measurement.

and ends on the side of the Lorentzian transmission curve gives the lowest uncertainty.

The systematic errors in the new measurement are analyzed by varying aspects of the fit to obtain uncertainties in the temperature. For high probe beam intensity, back-action causes the probe transmission to vary due to atoms oscillating in the probe potential, in agreement with numerical simulations. The intensity of the probe beam is kept low to reduce the frequency and amplitude of these oscillations. Sensitivity to the final background value in numerical testing gives an upper limit of 5% uncertainty in the temperature from fitting the tail of the data (≈3–8 μs in Fig. 4.8a). Resolution of the turn-off time of the trapping lattice is limited to ±20 ns uncertainty from a combination of the APD bandwidth and the ring down time of the optical cavity. Changing the start time in the fitting by this amount leads to 3% change in the temperature. Finally the uncertainty in the background

DC voltage of the APD causes a 1% error on the fit temperature. These combine for a total 6% systematic error. The statistical error on a temperature measurement is 10% for the axial data and 3% for the radial data.

As with the TOF measurement, there were a variety of additional checks we did to ensure the accuracy of the new measurement that did not lead to additional systematics. With respect to fitting, I made small variations in the cavity linewidth and the starting point in time with no effects, and ensured that the starting points of the five free parameters did not influence the results. I also tried fewer and additional free parameters, with fewer resulting in poor fitting, and additional resulting in unconstrained fits due to high correlations. With respect to the experiment, we verified that small variations in the initial probe detuning and power did not affect the temperature. We also confirmed that a blue-detuned probe led to the same results as a red-detuned probe.

We observe a small offset for the axial data between the two methods. We suspect this arises from the fact that the probe method is more sensitive to the dynamics of a dilute background of atoms that the TOF method misses. The simple assumption that the background distribution of atoms is constant in time is only approximately true; instead, the un-trapped background atoms, which comprise $10\% - 30\%$ of the total, will retain some periodicity due to the trapping lattice potential. This contributes additional time dependence to the coupling integral, Eq. 4.8, when the lattice is turned off. If this population comes from atoms that were heated out of the trap with low radial velocity, they remain overlapped with the probe mode as they fall due to gravity. This population of atoms can be seen in absorption images; however, due to the vertical extent ranging from the trapped atom cloud to the bottom of the optical cavity, we are unable to directly measure their axial temperature with TOF. These atoms will therefore raise the observed temperature of the new measurement without being observed via TOF, consistent with the results in Fig. 4.6.

As discussed in Section 4.1.1, we also observe a discrepancy between the fit results for the radial width free parameter $\sigma_{r,0}$ in the new temperature measurement compared with the calculated width based on a classical phase space distribution for a Gaussian potential.

Both the fitting of the probe transmission and the direct measurement of the width via absorption imaging produced a width up to 70% larger than the calculated width. We expect a broadening of the width when considering the 2-D phase space including the axial sinusoidal potential, but simulations suggest this only accounts for a 25% increase. We suspect a more complicated model including a heating term would be necessary to predict the width more accurately, and are interested in continuing to understand this discrepancy and compare observations with other experiments.

4.1.4 Conclusion

We have shown that site-independent coupling between atoms and the cavity mode can be exploited to provide nondestructive real-time information about the spatial distribution of atoms in an optical lattice. We demonstrate one useful application of this by measuring the temperature of atoms confined in an optical lattice.

This thermometry technique has many benefits over the commonly used TOF measurement. Because the measurement in the axial direction can be obtained while turning off the trapping lattice for only 10 μs, the atoms can easily be re-captured in the lattice. By turning the MOT beams and magnetic field back on, we were able to recapture about 75% of the atoms after the measurement. With additional cooling into the lattice, this recapture percentage should approach 100%. The technique can be extended to *in situ* thermometry of trapped atoms without releasing them from the optical lattice by monitoring the probe resonance shift as a function of lattice depth. Measuring the cavity resonance shift in reflection using a PDH error signal or even locking the probe beam to the (shifted) cavity resonance could increase the dynamic range and resolution of the cavity probe technique.

Other applications of this technique include single-shot observation of optomechanical oscillations as well as heating and cooling dynamics of trapped atoms. We expect the minimal perturbation caused by the probe beam will even allow *in situ* detection of the changes in atom wavefunction during Bloch oscillations [PTH09, KKV16, GVK17] and enable quantum sensors based on Bloch oscillations of atoms coupled to an optical cavity.

4.2 Nondemolition Bloch Oscillation Measurement

In the weak lattice regime, we expect our atoms to undergo Bloch oscillations due to the periodic potential and the force of gravity. Bloch oscillations are technically happening in the strong lattice regime described in the previous section as well, but the amplitude of oscillations would be too small to see due to the confining trap lattice. We plan on measuring the oscillation signal by observing the Bloch oscillation frequency on our cavity transmission, monitoring *in real time* the atoms' oscillations. In this section I describe a proposed use for this experiment, a precision measurement search for ultralight dark matter.

4.2.1 Dark matter Review

Dark matter (DM) is one of the most intriguing mysteries of our age. The evidence of its existence spans fields and techniques: the cosmic microwave background (CMB) angular power spectrum, velocity dispersion curves within a galaxy, and gravitation lensing from galaxies, to name just a few [Wik20]. It is approximated to make up 85% of the matter in our universe, and is likely to be a window into physics beyond the Standard Model.

Research to directly detect dark matter has recently focused on "cold dark matter" because it is the simplest model consistent with the observed galaxy formation properties. Two leading candidates are axions, very light particles that are a consequence of the Peccei–Quinn theory that solves the strong charge-parity (CP) problem of the Standard Model, and weakly interacting massive particles (WIMPs), a heavy particle motivated by supersymmetry. There are many expensive experiments to observe a heavy dark matter particle colliding with a large volume of material, which leads some in the community to feel that we are on the brink of detecting a WIMP particle. Unfortunately some have felt that way for >10 years, with still no detection.

Experimental physicists have also looked for a range of other candidates including axions, sterile neutrinos, gravitinos and other ultralight particles [Pet12]. Tabletop experiments typical of AMO experiments do not provide the volume necessary for a direct scatter as the

large-volume WIMP experiments do, but we do have extremely sensitive experiments that would be able to detect small continuous forces coming from ultralight dark matter. This type of dark matter goes by a variety of names including dilatons (due to their oscillating nature), virialized ultralight fields (VULFs) (due to their stable nature) or ultralight axion-like particles (ULAPs) (due to their similarities to the axion model).

A wide range of laboratory experiment techniques have been used to look for these ultralight particles. The Axion Dark Matter eXperiment (ADMX)[ACH10] has been looking for axions since 1995. Atom interferometry has compared either two atomic isotopes or two atomic species in search for equivalence principle violations that are dependent on atomic composition, motivated by a theory that predicts a boson force mediator coupling that scales as $A^{-1/3}$, where A is the atomic mass number [DD10]. Experiments have also used atom interferometry to look directly for mass oscillations of both the atom and the Earth predicted by some theories, in a composition independent manner, as we do with our experiment. Besides oscillations in the mass, other fundamental constants are expected to oscillate. Atomic clocks use their long-term stability to look for slow drifts in the fine-structure constant or the proton-electron mass ratio, which could indicate a slowly oscillating dark matter particle [AHV15]. Networks of atomic clocks could strengthen their limit; other network experiments, like the Global Network of Optical Magnetometers for Exotic physics (GNOME) [PJP13], look for clumps or walls of dark matter traveling through the Earth. There are also lab experiments searching for produced DM particles, such as the Heavy Unseen Neutrinos from Total Energy-momentum Reconstruction (HUNTER) [Smi19] experiment looking for sterile neutrinos.

Our experiment focuses on the composition independent search for a coherent oscillation in the mass of our atoms. From cosmological observations we have an estimate of the energy density of dark matter in our galaxy, $\rho_\phi \approx 0.3$ GeV/cm^3 [AHV15]. The mass of ultralight dark matter particles range from 10^{-21} eV/c^2 to 1 eV/c^2. The lower mass limit comes from the upper limit on the size of the deBroglie wavelength, λ_{dB}, capped at the size of a galaxy, the largest coherent dark matter object we have observed. The upper mass limit comes from

requiring a high enough particle density to observe macroscopic phenomena; the density is large enough, $\rho_\phi \gg \lambda_{dB}^{-3}$, that the bosonic particles can be modeled as a coherent wave [KMW85]. This particle also can act as a force carrier. Due to its mass it should provide a force with a spatial dependence given by the Yukawa potential. These features are analogous to a photon, which can act as a classical coherent wave as part of a laser at high density or act as a mediating force particle for the electric field.

In more detail, the general solution for the field equation of motion for dark matter is

$$\phi(t, x) = \phi_0 \cos(\omega_\phi t - k_\phi x), \tag{4.18}$$

where $\omega_\phi = m_\phi c^2/\hbar$ is the DM Compton frequency, m_ϕ is the DM mass, $k_\phi = 2\pi/\lambda_{\mathrm{dB}}$ and $\phi_0 = \hbar\sqrt{2\rho_\phi}/(m_\phi c)$ with the assumption that this type of dark matter makes up 100% of the total amount dark matter (Eq. 6 in [AHV15]). From now on I drop the x dependence since our experiment is much smaller than the dark matter coherence length, $k_\phi x \ll 1$. Because of the expected spread in velocities of dark matter about the velocity $v_\phi = 10^{-3}c$ in our galaxy, there is an expected coherence time to these oscillations,

$$\tau_{\mathrm{coh}} = \frac{1}{\omega_\phi}\frac{c^2}{v_\phi^2} \tag{4.19}$$

which corresponds to 10^6 oscillations.

This field is predicted to cause coherent oscillations in fundamental particle masses, electromagnetic interactions and/or gluonic interactions. Here I focus on the gluonic oscillations, which are expected to be the largest contributor to the oscillations in an atom's mass,

$$m(t) = m_0(1 + d_g\kappa_\phi\phi(t)), \tag{4.20}$$

where $\kappa_\phi = \sqrt{4\pi G}$, G is the gravitational constant, m_0 is the Standard Model mass, and d_g is the dimensionless coupling coefficient (Eq. 17 in [DD10]).

4.2.2 Expected Sensitivity

When our atoms undergo Bloch oscillations they oscillate at a frequency proportional to the force of gravity; see Eq. 2.47. Our precision on the frequency of Bloch oscillations is given

generically by

$$\delta\omega_g = \frac{2\pi}{\tau_{\rm int}}\frac{1}{\rm SNR}, \tag{4.21}$$

where $\tau_{\rm int}$ is the integration time of our experiment, and SNR is the signal to noise ratio.

The average photocurrent from a photodiode is given as $\langle i\rangle = eR_{\rm ph}$, where $R_{\rm ph}$ is the rate of photons hitting the detector, and where I have set the photodiode photoelectron conversation rate to one. In reality this conversation rate would be included as a multiplicative factor and depends on the specific photodiode in use. Shot noise on this current over all frequencies goes as $\Delta i = \sqrt{2e\Delta f\langle i\rangle}$, where Δf is the bandwidth of the photodetector. Because of the finite time of our measurement, the frequency spectrum is finite with $\frac{1/\tau_{\rm int}}{\Delta f}$ maximum number of bins. Shot noise is white, and the shot noise per frequency bin is $\Delta i_{\rm bin} = \sqrt{\frac{2e\langle i\rangle}{\tau_{\rm int}}}$. The signal to noise ratio in the signal frequency bin is

$$\text{SNR} = \frac{\epsilon\langle i\rangle}{\Delta i_{\rm bin}} = \epsilon\sqrt{\frac{R_{\rm ph}\tau_{\rm int}}{2}}, \tag{4.22}$$

where ϵ is the contrast of oscillations at the signal frequency.

The expected fractional precision on the frequency (and therefore the acceleration) given our simulated experimental parameters ($\epsilon = .03$, $R_{\rm ph} = 10^{11}$ Hz) is

$$\frac{\delta\omega_g}{\omega_g} = \frac{\delta g}{g} = \frac{2\pi}{\epsilon\omega_g\tau_{\rm int}}\sqrt{\frac{2}{R_{\rm ph}\tau_{\rm int}}} \approx \frac{10^{-7}}{\tau_{\rm int}^{3/2}} \tag{4.23}$$

Because the force of gravity is proportional to the mass, and we expect the mass to oscillate (Eq. 4.20) given the presence of ultralight dark matter, we expect our signal to look like an oscillating Bloch oscillation frequency. Our signal without dark matter is the cavity transmission,

$$\Theta = \epsilon R_{\rm ph} e\cos(\omega_g t). \tag{4.24}$$

If we introduce dark matter, the frequency will be oscillating as $\omega(t) = \omega_g\left(1 + \alpha\sin(\omega_\phi t)\right)$, where $\alpha \ll 1$ is the arbitrary relative strength of dark matter. The instantaneous phase from an oscillating frequency is,

$$\theta(t) = \int_0^t \omega(t)dt = \omega_g t - \alpha\frac{\omega_g}{\omega_\phi}\cos(\omega_\phi t). \tag{4.25}$$

The expected signal now has the form,

$$\epsilon R_{\rm ph} e \cos(\theta(t)) \approx \epsilon R_{\rm ph} e \cos(\omega_g t) \pm \epsilon R_{\rm ph} e \alpha \frac{\omega_g}{2\omega_\phi} \cos((\omega_g \pm \omega_\phi)t), \tag{4.26}$$

where I have applied the Bessel function expansion of an oscillating phase with a small ($\alpha \ll 1$) oscillation amplitude. We therefore expect the dark matter signal to show up as sidebands on the gravitational Bloch oscillation signal. Using the procedure above to find the signal to noise for dark matter where $\langle i \rangle = eR_{\rm ph}$ and now the contrast is $\epsilon\alpha\frac{\omega_g}{2\omega_\phi}$, we get,

$$\mathrm{SNR}_\phi = \frac{\epsilon\alpha\omega_g}{2\omega_\phi}\sqrt{\frac{R_{\rm ph}\tau_{\rm int}}{2}}. \tag{4.27}$$

We will fundamentally be limited by our level of shot noise. In order to compare to limits set by other AMO experiments looking for ultralight dark matter, I define our limit by setting the dark matter signal to noise ratio equal to one. With this definition, we can solve for α to obtain a "minimum detectable" α,

$$\alpha_{\rm min} = \frac{2\omega_\phi}{\epsilon\omega_g}\sqrt{\frac{2}{R_{\rm ph}\tau_{\rm int}}}. \tag{4.28}$$

This corresponds to a 1σ detection level. Comparing this minimum detectable sideband strength with Eq. 4.20, we can see that $\alpha = d_g\kappa_\phi\phi_0$, leading us to a minimum detectable coupling of,

$$d_g = \frac{2\omega_\phi}{\epsilon\omega_g}\frac{1}{\kappa_\phi\phi_0}\sqrt{\frac{2}{R_{\rm ph}\tau_{\rm int}}}. \tag{4.29}$$

In the case that $\tau_{\rm coh} > \tau_{\rm int}$, all of our samples are coherent and we get,

$$d_{g,\tau_{\rm coh}>\tau_{\rm int}} \approx \frac{1}{10^{-38}}\left(\frac{m_\phi^4 c^8/\mathrm{eV}^4}{\tau_{\rm int}/\mathrm{s}}\right)^{1/2}. \tag{4.30}$$

In the case that $\tau_{\rm coh} < \tau_{\rm int}$, we do not learn more information about the dark matter after its coherence time, and we just make improvements on our limit by averaging our noise. According to [BGL14], incoherent averaging after reaching the coherence time continues to decrease the noise by $(\tau_{\rm int}/\tau_{\rm coh})^{1/4}$. This change happens around $m_\phi c^2 \approx 10^{-15}$ eV. Due to the coherence time's dependence on the mass, the scaling after coherence time is reached

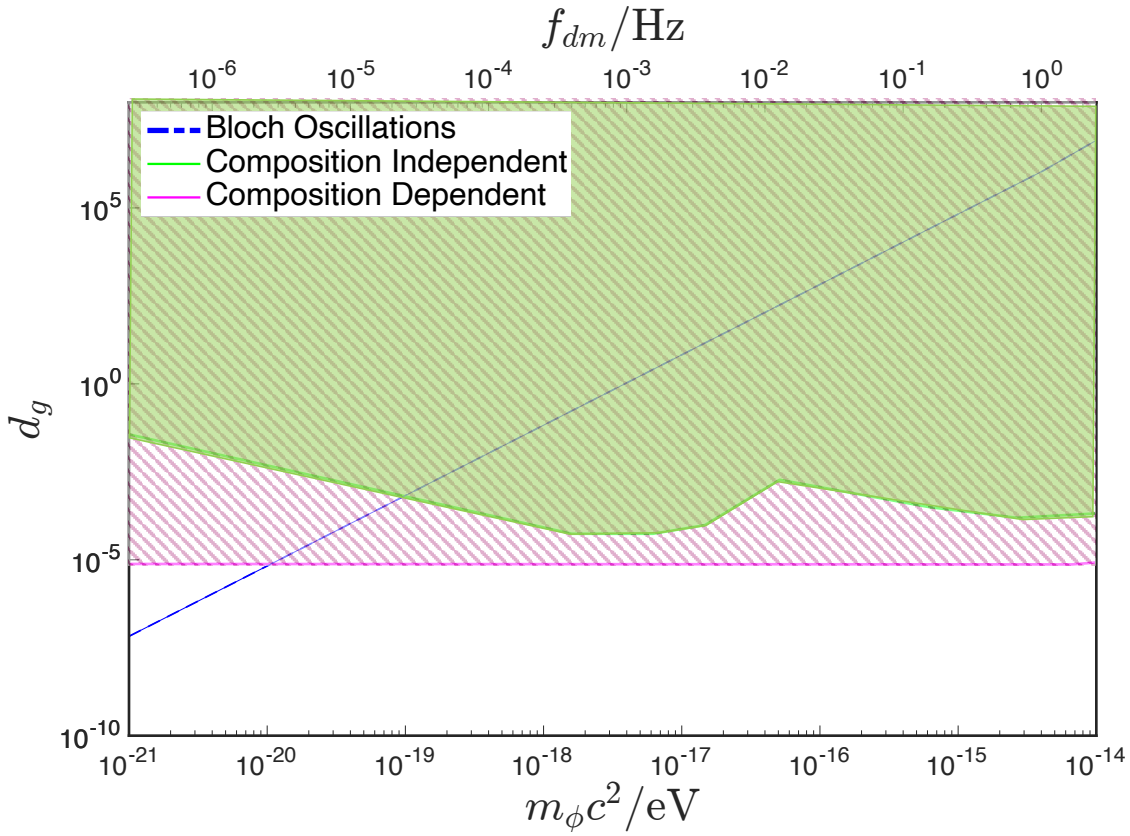

Figure 4.9: A comparison of our expected limit (dashed blue) to the current bounds for both composition independent (green) and composition dependent (pink) couplings both taken from Fig. 3 in [AHV15]. For comparison we used an integration time of $\tau_{\rm int} = 10^6$ s, and have defined the 1σ limit by setting $\mathrm{SNR}_\phi = 1$.

scales as,

$$d_{g,\tau_{\rm coh}<\tau_{\rm int}} \approx \frac{1}{10^{-40}} \left(\frac{m_\phi^9 c^{18}/\mathrm{eV}^9}{\tau_{\rm int}/\mathrm{s}} \right)^{1/4} . \tag{4.31}$$

See Figure 4.9 for a comparison of our limits to others in the field.

We are currently working on further cooling our atoms beyond the 3D MOT in order to efficiently load into the ground state of the very shallow lattice needed for large Bloch oscillations. I will continue the discussion of the future of our experiment as it moves towards the sensitivity goals described here in Chapter 5.

CHAPTER 5

The Future

The next experimental push will be to observe Bloch oscillations from our Yb atoms on the optical cavity transmission. In this section I discuss some of the future barriers and potential solutions, as well as our plan for a lattice cooling stage.

5.1 Towards observing Bloch oscillations

5.1.1 Signal to noise ratio improvements

As discussed in Section 3.3.1, our cavity linewidth appears to be increasing linearly with time. Since installation in April 2018, the linewidth has increased by a factor of two (see Figure 3.20). Our current best guess for this is Yb solidifying onto the bottom mirror surface as we run our experiment. If this is the problem, we shouldn't expect the linewidth to get worse during the months of March to May due to the global pandemic stay-at-home order since our Yb oven is turned off.

The increased linewidth has a serious effect on our expected Bloch oscillation resolution and dark matter limits. Running the same simulation that produced Figure 2.5 while changing the linewidth from the ideal $2\pi \cdot 1.8$ MHz to the current $2\pi \cdot 3.5$ MHz, the signal to noise drops by a factor of 3.5 and the contrast drops by a factor of 5.5. From Eq. 4.21 we can see that our limit scales with the SNR. A more thorough analysis of the relationship between κ and the SNR reveals that the SNR decays exponentially with respect to κ with an exponential decay constant of ~ -1.5; see Figure 5.1.

There are two options moving forward to improve the signal to noise ratio: open our

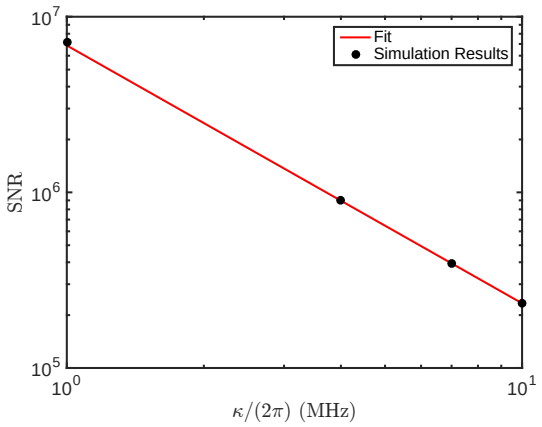

Figure 5.1: Signal to noise ratio obtained via simulation (Section 3.3.1) for different cavity linewidths. The fit result is $\log(\text{SNR}) = -1.468\log(\kappa) + 38.72$ showing the exponential scaling.

vacuum chamber to replace the mirrors or improve other experimental parameters that will boost our SNR. Opening up the vacuum chamber is time consuming, but ideally we could employ some more permanent solution. At the very least, we could install new cavity mirrors.

Installing new mirrors is not an easy process due to the epoxy chosen to attach the current mirrors. Previous efforts to bake the cavity system at 200°C until the epoxy was brittle enough to pull the mirrors off led to breaking the spacer. In addition, we paid to have the mirrors aligned very well by the company that made the spacer, which was expensive. With more time and engineering a metal or 3D printed plastic spacer could be used as a cheaper alignment alternative.

There are a variety of small upgrades I recommend for new mirrors. I would recommend looking into additional coatings to expand the experimental possibilities of our lattice, for example looking at the magic wavelength of Yb near 613 nm for a pi transition or near 858 nm for a sigma transition [TYJ18]. If we also want to upgrade the spacer, extending the side cut outs in the direction of the atom beam would allow for more optical access and possibly ease mirror alignment. Gluing the new mirrors to a new spacer would also reduce complications with the epoxy.

Changing other experimental parameters could also allow us to increase our SNR. For example, we could increase the number of atoms loaded into the lattice. This could be done by increasing the MOT load time (and taking a hit on experimental down time) or by improving cooling efficiency. In the next section I discuss some future ideas for improving cooling. Large improvements are possible due the fact that the SNR scales as the square of the number of atoms. The other experimental parameter that would be easy to change is the acceptable scattering rate, which negatively affects our experimental down time while allowing us to decrease our detuning. The SNR improves exponentially with a decrease in scattering rate with an exponential constant of 1.5.

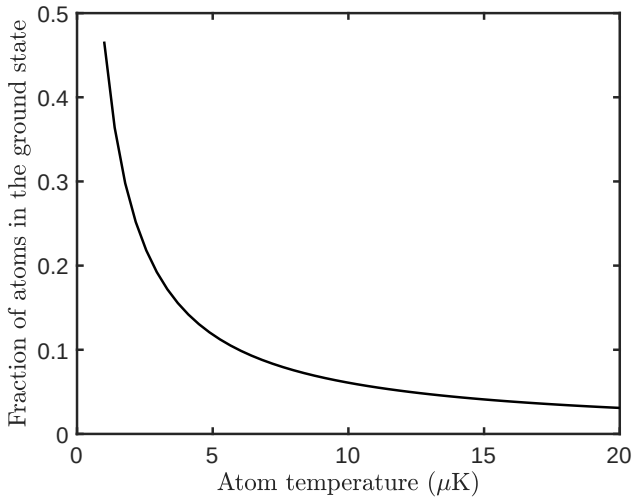

Figure 5.2: Fraction of atoms at temperature T_a loaded into the ground state of a lattice with potential depth $U_t = 3\ E_R$, as calculated from Eq. 5.1.

5.1.2 Cooling

Resolving Bloch oscillations requires that the majority of atoms are in the ground state of the optical lattice. The fraction of the thermal atom sample loaded into the ground state can be calculated directly from the Boltzmann distribution,

$$f = \frac{e^{-\frac{E_0}{k_B T_a}}}{\sum_n e^{-\frac{E_n}{k_B T_a}}} = \frac{e^{-\frac{n\hbar\omega_\ell}{k_B T_a}}}{1 - e^{-\frac{\hbar\omega_\ell}{k_B T_a}}}. \tag{5.1}$$

Here I have used the approximation that the potential is an SHO. Loading directly into a $U_t = 3E_R$ lattice for Bloch oscillations at the coldest MOT temperature achieved, 5 μK, would only lead to a loading fraction of 0.1; see Figure 5.2.

For atoms loaded into a $U_t/k_B = 100\ \mu$K lattice, the fraction of atoms in the ground state can be seen on Figure 5.3. Atoms thermalize in our lattice at $T_z = 0.2U_t/k_B$, which would result in a ≈0.35 loading fraction. We attempted to quickly load colder atoms ($T_a \approx 10\ \mu$K) into the lattice followed by adiabatically ramping down the depth to maintain atom state fractions, but we had problems with atoms leaking out of the lattice radially.

Radial leakage could be solved by radial confinement or radial cooling. We attempted adding a crossed dipole trap to confine atoms in the radial direction, but we were unable to do

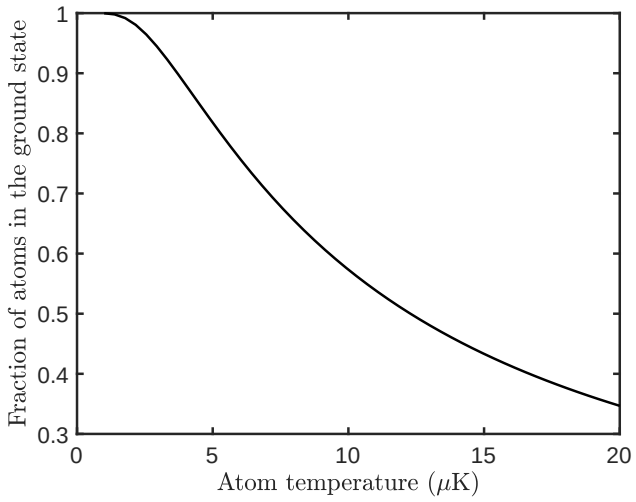

Figure 5.3: Fraction of atoms at temperature T_a loaded into the ground state of a lattice with potential depth $U_t/k_B = 100$ μK, as calculated from Equation 5.1.

so without further heating the atoms in both the axial and radial direction. We suspect that this was due to phase instability of the crossed trapping beams, which leads to amplitude fluctuation in the lattice depth. In the future we could consider using higher order cavity modes with a ring structure to radially confine the atoms.

Electromagnetically Induced Transparency (EIT) Cooling Due to these complications, we have been pushing forward on methods for cooling directly into the ground state of the lattice. Generically, this can be done by performing a two photon transition, where the atoms in an electronic ground state and an SHO state n absorb a photon and emit a photon such that they end back in the ground state, but in an SHO state $n-1$. If this is a cycling transition, the process will occur over and over until the atom occupies the ground state $n = 0$.

The main challenge to overcome when cooling in the lattice is resolving the harmonic oscillator energy bands. To resolve energy bands we need separation of much more than the natural linewidth, which for us would lead to using a very deep lattice that we possibly don't have enough power for. This increased lattice intensity also increases the scattering

rate from lattice photons, which causes residual heating.

The most promising method is electromagnetically induced transparency (EIT) cooling [PWB12]. This method of cooling would work on the two magnetic $^1S_0$ F=1/2 ground states of Yb^{171} and one $^3P_1$ F=1/2 magnetic excited state. The two photon transition between the two ground states interferes in such a way to cause an off resonance excitation that is narrower than the natural linewidth of the transition, allowing us to resolve the trap levels. Experimental efforts for implementing EIT cooling in our lab have begun; immediately before the mandated lab shut down we observed the narrow EIT resonance through absorption imaging of the atoms.

I am excited to watch the future development of this lab and to see all of the cool new experiments in the years to come.

CHAPTER 6

Appendix

6.1 Cavity Spacer Technical Drawing

See Figure 6.1.

6.2 EOM Input Impedance Circuit

For all of our MTS locking systems, we use an electro-optic modulator (EOM) to provide phase modulation to our beam. The EOM drive amplitude needs to be on the order of tens of volts to obtain sufficient phase modulation, and a tank circuit to match the 50Ω input impedance at the desired modulation frequency was necessary to minimize back reflection of the RF signal.

To test the RF signal reflection, a coupler was used to direct the reflected signal to a spectrum analyzer. The initial reflection out of the EOM was 4.6 dBm. A homemade LC resonant circuit was placed before the EOM to impedance match and amplify the input. Different capacitor values were tested, and a 470 pF capacitor was used in the final circuit. To make an inductor, 18 gauge magnetic wire was coiled around a 2 cm diameter pen cap. The inductor started with 34 turns and the LC circuit was tested to see if there was improved reflection at the desired frequency, ω_m. Coil spacing and turn number were adjusted until the reflection was minimized to -8 dBm at the desired ω_m of 17.5 MHz. Note that when the circuit is placed in a metal box, the induction slightly changes along with the resonant frequency of the circuit.

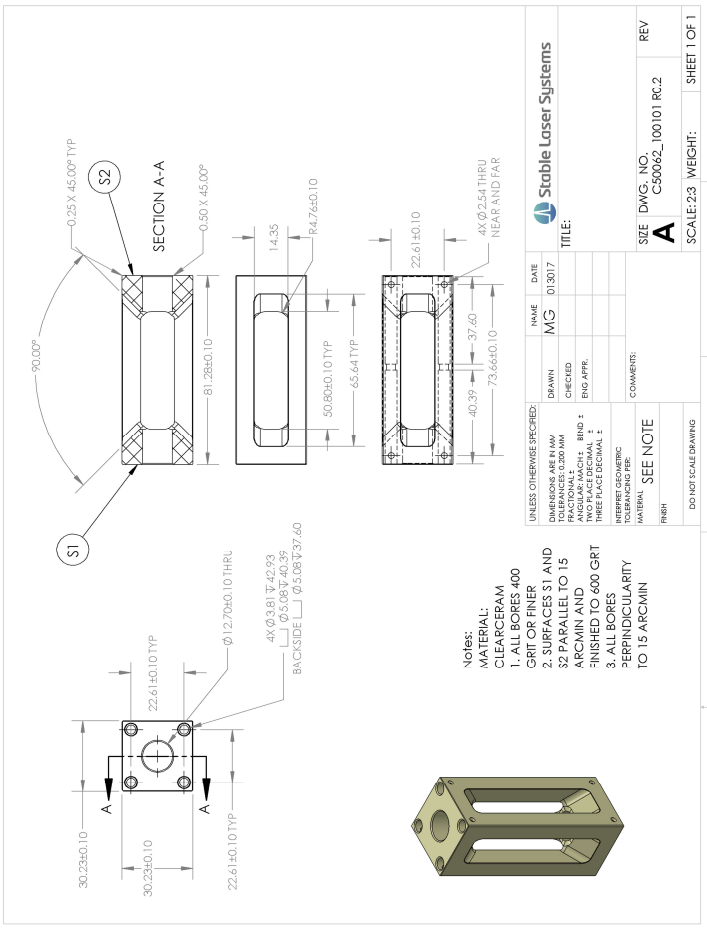

Form 100rev 1

Figure 6.1: Technical drawing for the cavity spacer. This drawing was made by Stable Laser Systems. NOTE: this drawing had an error and the piece needed to be reworked. The sides labeled "S1" and "S2" should refer to the two facing inner surfaces instead of the two facing outer surfaces.

6.3 Compensation Coil Control Circuit

The compensation coil circuits were originally supposed to include an "H bridge" for switching the direction of the current, and a "control circuit" for controlling the amplitude of the current. Both circuits contain multiple MOSFETs, and we found that the H bridge MOSFETs were breaking too often to be of use. Additionally, we have no need to change the sign of the fields regularly at this moment. Since both circuits were built and I already have a description written up for the full circuit, I include both parts here. Upgrading to MOSFETs with higher current rating fixed them breaking in the control circuit, and could fix the problem in the H bridge circuit portion too if replaced.

The H bridge circuit can be seen at the top of Figure 6.2. The purpose of this portion of the circuit is to control the direction of the current flow, and thus the direction of the magnetic field. The circuit takes a control voltage from a power supply, and a TTL input controlling the direction of the field.

MOSFETs are used as logic switches to control the direction of the current. When the input TTL is low, the left 2N7000 MOSFET acts like an open circuit, and the point at 'NOT Logic in' is at the control voltage, while the right 2N7000 MOSFET is active acting as a closed circuit. The MOSFETs switch rolls when the input TTL is high.

The left part of the H bridge circuit has MOSFET switches controlled by the voltage at 'Logic in' and 'NOT Logic in'. Note that the two top MOSFETs are p-channel, while the two at the bottom are n-channel. Determined by the TTL input, the current will either flow from the top left, through the compensation coil, and through the bottom right, or from the top right to the bottom left. The voltage at the source of the n-channel MOSFETS is set by the bottom portion of the circuit at around 1 V.

The current control circuit can be seen at the bottom of Figure 6.2. This circuit is set up to work with either a fixed supply voltage or an analog control voltage. The fixed supply input is followed by a potentiometer voltage divider, an amplifying op amp circuit, and an inverting op amp circuit. The third op amp in the row is the control op amp for both the

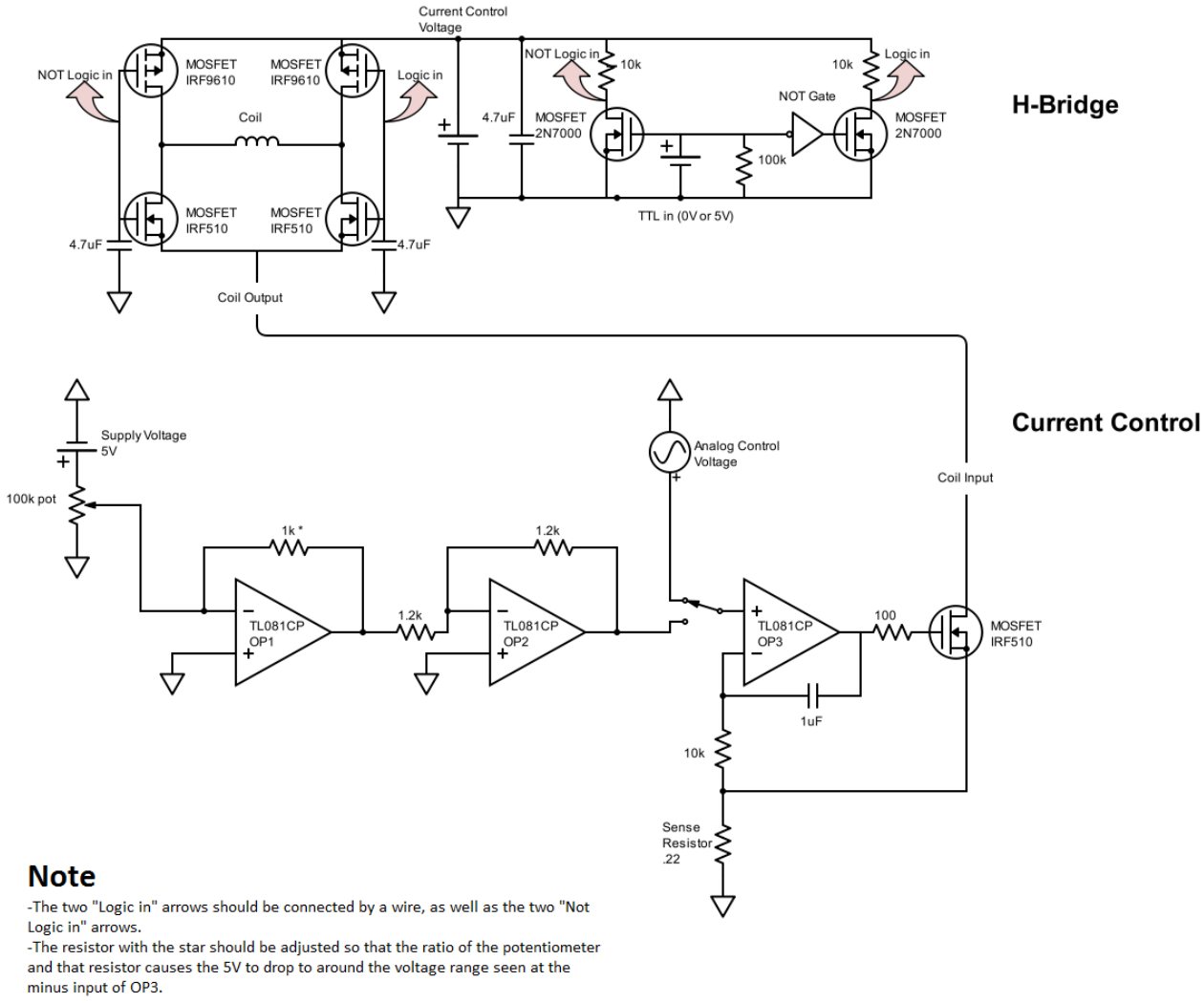

Figure 6.2: Compensation coil current control circuits. The top circuit, the H bridge, controls which direction the current flows. The bottom circuit controls the amplitude of the current. This circuit drawing was made by Paul Hamilton or one of his colleagues.

fixed supply and the analog supply. This op amp works as feedback to regulate the voltage at the gate of the control MOSFET to its right. The voltage and resistor values were chosen such that after the voltage drop from the MOSFETs and coil in the H bridge circuit, the voltage at the source of the control MOSFET is fixed at 1 V. Therefore, if the gate voltage is greater than a couple of volts, the MOSFET is active, and current flows. As the voltage

is changed, the amount of current through the MOSFET changes as well.

6.4 Code Locations

All of the code is located in our Box folder at /Box/Lab files/Matlab, which I will define as '∼' for the following paths.

6.4.1 Modulation Transfer Spectroscopy

This MATLAB script is a simple calculation of the modulation transfer spectroscopy signal given an atomic linewidth, a modulation frequency and a modulation depth. Simulation results are in Figure 2.4.

Paths:

- Main: ∼/MTS.m

6.4.2 Bloch Oscillation Simulation

The main code is broken up into sections: constants, initial conditions, time evolution, plotting and signal to noise ratio calculation. The constants section is where one can adjust the details of the experimental parameters, as well as simulation constants.

The time evolution section uses a MATLAB kit 'expokit' to deal with large sparce matrices with the function 'expv'. It calls three MATLAB functions to calculate the Hamiltonian ('Hamiltonian_M.m'), $g^2(t + \Delta t)$ ('g_squared.m') and $\alpha(t + \Delta t)$ ('alphafunc.m'). Simulation results are in Figure 2.5.

Paths:

- Main: ∼/BlochOscillationSims/Chandlers_Code/lattice_depth_simulation_clean_03_31_20.m
- Expokit (hardcoded add in main script): ∼/BlochOscillationSims/Chandlers_Code/expokit
- Hamiltonian: ∼/BlochOscillationSims/Chandlers_Code/Hamiltonian_M.m

- $g^2(t + \Delta t)$: ∼/BlochOscillationSims/Chandlers_Code/g_squared.m
- $\alpha(t + \Delta t)$: ∼/BlochOscillationSims/Chandlers_Code/alphafunc.m

6.4.3 Zeeman Slower

Most of this code was written by my post-doc Robert Niederriter, so I will simply list the figure locations.

Paths:

- Figure 3.10: ∼/Zeemann slower sims/Zeeman slower coil positions 9-13-2017.fig
- Figure 3.11: ∼/Zeemann slower sims/Magnetic fields of individual slower coils 9-13-2017.fig

6.4.4 New Atomic Temperature Measurement

The new temperature fitting analysis was performed in two main scripts, one for the axial direction and one for the radial. That code allows the fitting of all of the final data at once. Each fit is individually performed in "Temperature_Fitting_sfloat.m" and "Temperature_Fitting_Trans_sfloat.m". The fitting functions themselves for both directions are called from those scripts.

I also list the code used to make the figures used in the paper, as well as additional figures I have included in my thesis. The locations for figures relevant to the verifications of the atomic distribution also contain much of the analysis.

In this section I will use ∼* to represent ∼Temperature_Measurement.

Paths:

- Figures 4.1, 4.5, 4.6, 4.8 made in ∼*/Figures for probe paper/FiguresForProbeTemperaturePaper.m
- Final data: ∼*data_plotting.m
- Verification of atomic distribution

  - Figure 4.2: ∼*/Thermal_SHO.m
  - Classical simulation: ∼* /classical_trajectories.m
  - Figure 4.3: ∼*/TOF Fitting/picture_analysis.m
  - Figure 4.4: ∼*/Gaussian_Width.m

- New temperature fitting
  - Main axial: ∼*/Multi_Fit_Temperature_sfloat_FINAL.m
  - Temperature fitting axial: ∼*/Temperature_Fitting_sfloat.m
  - Transmission function axial: ∼*/Temperature_Function_sfloat.m
  - Main radial: ∼*/Multi_Fit_Temperature_Trans_sfloat_FINAL.m
  - Temperature fitting radial: ∼*/Temperature_Fitting_Trans_sfloat.m
  - Transmission function radial: ∼*/Temperature_Function_Transverse_sfloat.m

6.4.5 Dark Matter

Paths:

- Figure **??**: ∼Simple Analysis Testing/simple_analysis_testing.m
- Figure 4.9: ∼Limit_Plots.m (works in MATLAB 2015 but not MATLAB 2019)

6.4.6 The Future

Paths:

- Figures 5.2 and 5.3: ∼/Temperature_Measurement/Thermal_SHO.m

Bibliography

[AB20] Nobel Media AB. "The Nobel Prize in Physics 1997.", 2020.

[ACH10] S. J. Asztalos, G. Carosi, C. Hagmann, D. Kinion, K. van Bibber, M. Hotz, L. J Rosenberg, G. Rybka, J. Hoskins, J. Hwang, P. Sikivie, D. B. Tanner, R. Bradley, and J. Clarke. "SQUID-Based Microwave Cavity Search for Dark-Matter Axions." *Phys. Rev. Lett.*, **104**:041301, Jan 2010.

[AHV15] Asimina Arvanitaki, Junwu Huang, and Ken Van Tilburg. "Searching for dilaton dark matter with atomic clocks." *Phys. Rev. D*, **91**:015015, Jan 2015.

[AM76a] Neil W. Ashcroft and N. David Mermin. *Solid state physics*. Cengage Learning, 1976.

[AM76b] N.W. Ashcroft and N.D. Mermin. *Solid State Physics*. Saunders College, Philadelphia, 1976.

[Bal08] P.V. Balasubramanian. *"Bloch-Zener Oscillations of a cold atom in an optical cavity."*. Master's thesis, McMaster University, 2008.

[BBS12] Nathan Brahms, Thierry Botter, Sydney Schreppler, Daniel W. C. Brooks, and Dan M. Stamper-Kurn. "Optical Detection of the Quantization of Collective Atomic Motion." *Phys. Rev. Lett.*, **108**:133601, Mar 2012.

[BCW13] Bohnet, Justin G., Chen, Zilong, Weiner, Joshua M., Cox, Kevin C., Meiser, Dominic, Holland, Murray J., and Thompson, James K. "A quasi-continuous superradiant Raman laser with <1 intracavity photon." *EPJ Web of Conferences*, **57**:03003, 2013.

[BGL14] Dmitry Budker, Peter W. Graham, Micah Ledbetter, Surjeet Rajendran, and Alexander O. Sushkov. "Proposal for a Cosmic Axion Spin Precession Experiment (CASPEr)." *Phys. Rev. X*, **4**:021030, May 2014.

[Blo29] Felix Bloch. "Über die Quantenmechanik der Elektronen in Kristallgittern." *Zeitschrift für Physik*, **52**(7):555–600, 1929.

[BMZ02] Tomasz M Brzozowski, Maria Maczynska, Michal Zawada, Jerzy Zachorowski, and Wojciech Gawlik. "Time-of-flight measurement of the temperature of cold atoms for short trap-probe beam distances." *Journal of Optics B: Quantum and Semiclassical Optics*, **4**(1):62–66, jan 2002.

[Boh14] J.G. Bohnet. *A Superradiant Laser and Spin Squeezed States: Collective Phenomena in a Rubidium Cavity QED System for Enhancing Precision Measurements*. PhD thesis, University of Colorado, 2014.

[BPR96] Maxime Ben Dahan, Ekkehard Peik, Jakob Reichel, Yvan Castin, and Christophe Salomon. "Bloch Oscillations of Atoms in an Optical Potential." *Phys. Rev. Lett.*, **76**:4508–4511, Jun 1996.

[CGJ10] Cheng Chin, Rudolf Grimm, Paul Julienne, and Eite Tiesinga. "Feshbach resonances in ultracold gases." *Rev. Mod. Phys.*, **82**:1225–1286, Apr 2010.

[CGW16] Kevin C. Cox, Graham P. Greve, Baochen Wu, and James K. Thompson. "Spatially homogeneous entanglement for matter-wave interferometry created with time-averaged measurements." *Phys. Rev. A*, **94**:061601, Dec 2016.

[CMC06] Pierre Cladé, Estefania de Mirandes, Malo Cadoret, Saïda Guellati-Khélifa, Catherine Schwob, Fran çois Nez, Lucile Julien, and Fran çois Biraben. "Determination of the Fine Structure Constant Based on Bloch Oscillations of Ultracold Atoms in a Vertical Optical Lattice." *Phys. Rev. Lett.*, **96**:033001, Jan 2006.

[Com] "Commercial Solid State Lasers.".

[CVD] Sumanth B. Chikkamaranahalli, R. Ryan Vallance, Bradley N. Damazo, and Richard M. Silver. "Damping mechanisms for precision applications in UHV environment.".

[D13] S. Dörscher. *Creation of ytterbium quantum gases with a compact 2D-/3D-MOT setup*. PhD thesis, Universität Hamburg, 2013.

[DD10] Thibault Damour and John F. Donoghue. "Equivalence principle violations and couplings of a light dilaton." *Phys. Rev. D*, **82**:084033, Oct 2010.

[DHK83] R. W. P. Drever, J. L. Hall, F. V. Kowalski, J. Hough, G. M. Ford, A. J. Munley, and H. Ward. "Laser phase and frequency stabilization using an optical resonator." *Applied Physics B*, **31**(2):97–105, 1983.

[DHL05] E. A. Donley, T. P. Heavner, F. Levi, M. O. Tataw, and S. R. Jefferts. "Double-pass acousto-optic modulator system." *Review of Scientific Instruments*, **76**(6):063112, 2005.

[Fey73] Richard P. Feynman. *Statistical mechanics: a set of lectures*. Benjamin, 1973.

[Foo05] C. J. Foot. *Atomic physics*. Oxford University Press, 2005.

[Fre15] R. Freytag. *Simultaneous Magneto-Optical Trapping of Ytterbium and Caesium*. PhD thesis, Imperial College London, 2015.

[GVK17] Ch. Georges, J. Vargas, H. Keßler, J. Klinder, and A. Hemmerich. "Bloch oscillations of a Bose-Einstein condensate in a cavity-induced optical lattice." *Phys. Rev. A*, **96**:063615, Dec 2017.

[GW60] J. A. Giordmaine and T. C. Wang. "Molecular Beam Formation by Long Parallel Tubes." *Journal of Applied Physics*, **31**(3):463–471, 1960.

[HBV19] Richard Hobson, William Bowden, Alvise Vianello, Ian R. Hill, and Patrick Gill. "Cavity-enhanced non-destructive detection of atoms for an optical lattice clock." *Opt. Express*, **27**(26):37099–37110, Dec 2019.

[JPR01] R. Jáuregui, N. Poli, G. Roati, and G. Modugno. "Anharmonic parametric excitation in optical lattices." *Phys. Rev. A*, **64**:033403, Aug 2001.

[KEK08] Masaaki Kitagawa, Katsunari Enomoto, Kentaro Kasa, Yoshiro Takahashi, Roman Ciuryło, Pascal Naidon, and Paul S. Julienne. "Two-color photoassociation spectroscopy of ytterbium atoms and the precise determinations of s-wave scattering lengths." *Phys. Rev. A*, **77**:012719, Jan 2008.

[KHT99] T. Kuwamoto, K. Honda, Y. Takahashi, and T. Yabuzaki. "Magneto-optical trapping of Yb atoms using an intercombination transition." *Phys. Rev. A*, **60**:R745–R748, Aug 1999.

[KK13] Aviv Keshet and Wolfgang Ketterle. "A distributed, graphical user interface based, computer control system for atomic physics experiments." *Review of Scientific Instruments*, **84**(1):015105, 2013.

[KKV16] H Keßler, J Klinder, B Prasanna Venkatesh, Ch Georges, and A Hemmerich. "In situ observation of optomechanical Bloch oscillations in an optical cavity." *New Journal of Physics*, **18**(10):102001, oct 2016.

[KMW85] Lawrence Krauss, John Moody, Frank Wilczek, and Donald E. Morris. "Calculations for cosmic axion detection." *Phys. Rev. Lett.*, **55**:1797–1800, Oct 1985.

[LFS93] Karl Leo, Joehen Feldmann, Jagdeep Shah, Gero [von Plessen], Peter Thomas, Stefan Schmitt-Rink, and John Cunningham. "Optical investigation of bloch oscillations in semiconductor superlattices." *Superlattices and Microstructures*, **13**(1):55 – 60, 1993.

[LHW97] Chris Leahy, J. Todd Hastings, and P. M. Wilt. "Temperature dependence of Doppler-broadening in rubidium: An undergraduate experiment." *American Journal of Physics*, **65**(5):367–371, 1997.

[Neg09] Vladimir Negnevitsky. "Modulation transfer spectroscopy for fast , accurate laser stabilisation." 2009.

[Pet98] A. Peters. *High precision gravity measurements using atom interferometry*. PhD thesis, Stanford University, May 1998.

[Pet12] Annika Peter. "Dark Matter: A Brief Review." 01 2012.

[PJP13] Szymon Pustelny, Derek F. Jackson Kimball, Chris Pankow, Micah P. Ledbetter, Przemyslaw Wlodarczyk, Piotr Wcislo, Maxim Pospelov, Joshua R. Smith, Jocelyn Read, Wojciech Gawlik, and Dmitry Budker. "The Global Network of Optical Magnetometers for Exotic physics (GNOME): A novel scheme to search

for physics beyond the Standard Model." *Annalen der Physik*, **525**(8-9):659–670, 2013.

[PMC09a] B. M. Peden, D. Meiser, M. L. Chiofalo, and M. J. Holland. "Nondestructive cavity QED probe of Bloch oscillations in a gas of ultracold atoms." *Phys. Rev. A*, **80**:043803, Oct 2009.

[PMC09b] B. M. Peden, D. Meiser, M. L. Chiofalo, and M. J. Holland. "Nondestructive cavity QED probe of Bloch oscillations in a gas of ultracold atoms." *Phys. Rev. A*, **80**:043803, Oct 2009.

[PTH09] B. Prasanna Venkatesh, M. Trupke, E. A. Hinds, and D. H. J. O'Dell. "Atomic Bloch-Zener oscillations for sensitive force measurements in a cavity." *Phys. Rev. A*, **80**:063834, Dec 2009.

[PWB12] Thorsten Peters, Benjamin Wittrock, Frank Blatt, Thomas Halfmann, and Leonid P. Yatsenko. "Thermometry of ultracold atoms by electromagnetically induced transparency." *Phys. Rev. A*, **85**:063416, Jun 2012.

[PWT11] N. Poli, F.-Y. Wang, M. G. Tarallo, A. Alberti, M. Prevedelli, and G. M. Tino. "Precision Measurement of Gravity with Cold Atoms in an Optical Lattice and Comparison with a Classical Gravimeter." *Phys. Rev. Lett.*, **106**:038501, Jan 2011.

[RTB89] M. G. Raizen, R. J. Thompson, R. J. Brecha, H. J. Kimble, and H. J. Carmichael. "Normal-mode splitting and linewidth averaging for two-state atoms in an optical cavity." *Phys. Rev. Lett.*, **63**:240–243, Jul 1989.

[SLc10] Monika H. Schleier-Smith, Ian D. Leroux, and Vladan Vuletić. "States of an Ensemble of Two-Level Atoms with Reduced Quantum Uncertainty." *Phys. Rev. Lett.*, **104**:073604, Feb 2010.

[Smi19] Peter F Smith. "Proposed experiments to detect keV-range sterile neutrinos using energy-momentum reconstruction of beta decay or K-capture events." *New Journal of Physics*, **21**(5):053022, may 2019.

[SR05] H. Salami and A.J. Ross. "A molecular iodine atlas in ascii format." *Journal of Molecular Spectroscopy*, **233**(1):157–159, 09 2005.

[SRG15] Ruwan Senaratne, Shankari V. Rajagopal, Zachary A. Geiger, Kurt M. Fujiwara, Vyacheslav Lebedev, and David M. Weld. "Effusive atomic oven nozzle design using an aligned microcapillary array." *Review of Scientific Instruments*, **86**(2):023105, 2015.

[The] "Thermal Properties of Metals, Conductivity, Thermal Expansion, Specific Heat: Engineers Edge.".

[TYJ18] Zhi-Ming Tang, Yan-Mei Yu, Jun Jiang, and Chen-Zhong Dong. "Magic wavelengths for the $6s^2\,{}^1S_0$–$6s6p\,{}^3P_1^o$ transition in ytterbium atom." *Journal of Physics B: Atomic, Molecular and Optical Physics*, **51**(12):125002, may 2018.

[VBE17] G Vallet, E Bookjans, U Eismann, S Bilicki, R Le Targat, and J Lodewyck. "A noise-immune cavity-assisted non-destructive detection for an optical lattice clock in the quantum regime." *New Journal of Physics*, **19**(8):083002, aug 2017.

[Wik19] Wikipedia contributors. "Vapor pressures of the elements (data page) — Wikipedia, The Free Encyclopedia.", 2019. [Online; accessed 04-January-2020].

[Wik20] Wikipedia contributors. "Dark Matter — Wikipedia, The Free Encyclopedia.", 2020. [Online; accessed 30-March-2020].

[WYJ11] Wen-Li Wang, Jie Ye, Hai-Ling Jiang, Zhi-Yi Bi, Long-Sheng Ma, and Xin-Ye Xu. "Frequency stabilization of a 399-nm laser by modulation transfer spectroscopy in an ytterbium hollow cathode lamp." *Chinese Physics B*, **20**(1):013201, jan 2011.

[XJP19] Victoria Xu, Matt Jaffe, Cristian D. Panda, Sofus L. Kristensen, Logan W. Clark, and Holger Müller. "Probing gravity by holding atoms for 20 seconds." *Science*, **366**:745–749, 2019.

[Zer] "Schott Advanced Optics, https://www.us.schott.com/advanced_optics/english/products/optical-materials/zerodur-extremely-low-expansion-glass-ceramic/zerodur/index.html.".

[ZMC12] Hao Zhang, Robert McConnell, Senka Ćuk, Qian Lin, Monika H. Schleier-Smith, Ian D. Leroux, and Vladan Vuletić. "Collective State Measurement of Mesoscopic Ensembles with Single-Atom Resolution." *Phys. Rev. Lett.*, **109**:133603, Sep 2012.